MANCHESTER 1824
The University of Manchester

Electronic and Magnetic Interpretation of Linear Transition Metal Ions: Insights From X-ray Spectroscopy

A thesis submitted to the University of Manchester for the degree of
Doctor of Philosophy
in the Faculty of Science and Engineering

2022

Myron S. Huzan
Department of Chemistry

Contents

Word Count: 24,175

List of Figures

List of publications

Wu, S. Q., Liu, M., Gao, K., Kanegawa, S., Horie, Y., Aoyama, G., Okajima, H., Sakamoto, A., Baker, M. L., **Huzan, M. S.**, Bencok, P., Abe, T., Shiota, Y., Yoshizawa, K., Xu, W., Kou, H. Z., & Sato, O. (2020). Macroscopic Polarization Change via Electron Transfer in a Valence Tautomeric Cobalt Complex. Nature Communications, 11(1), 1–8.

Huzan, M. S., Fix, M., Aramini, M., Bencok, P., Mosselmans, J. F. W., Hayama, S., Breitner, F. A., Gee, L. B., Titus, C. J., Arrio, M. A., Jesche, A., & Baker, M. L. (2020). Single-ion magnetism in the extended solid-state: Insights from X-ray absorption and emission spectroscopy. Chemical Science, 11(43), 11801–11810.

Abstract

Technological advancements progress materials to the atomic level, and single ion magnets (SIMs) provide several routes of prospective applications within the field of *molecular magnetism*. SIMs achieve a bi-stability of magnetism due to single-ion magnetic anisotropy that is devoid of long-range magnetic ordering. $Li_2(Li_{1-x}Fe_x)N$ achieves remarkable SIM properties that compare favourably with respect to the highest-performing TM- and Ln-SIM systems. The most popular method for preparing SIMs targets coordination chemistry approaches involving bulky organic and inorganic ligand environments encompassing a paramagnetic metal centre to maximise single-ion magnetic anisotropy. However, doping of transition metal ions within a diamagnetic extended solid-state host lattice, such as $Li_2(Li_{1-x}Fe_x)N$, exists as a growing and prospective avenue of scientific pursuit achieving exceptional single ion properties, in spite of the challenges associated with the study of dopant ions.

The application of core-level spectroscopic techniques facilitates an element- specific, high brilliance probe to deduce a plethora of properties beyond laboratory-based methods. This thesis applies an array of inaugural spectroscopic techniques with computational interpretation for a series of monovalent, high symmetry TM systems, $Li_2(Li_{1-x}TM_x)N$ where TM = Mn, Fe, Co, Ni and Cu. Upon commencing this thesis, conclusive experimental quantification of orbital hybridisation of linear TM ions was contingent on theoretical measures. However, upon conclusion, the isolation and quantification of substantial $3d$-$4s$ orbital hybridisation and metal-to-ligand charge-transfer is unravelled through experimental measurements and corroborated through multiplet and *ab initio* calculations. The measurements and analysis methods developed have a direct view of application to analogue complexes to further support our understanding of high-performing SIMs and continued synthetic achievements within this ever-growing field.

Declaration of originality

I hereby confirm that no portion of the work referred to in the thesis has been submitted in support of an application for another degree or qualification of this or any other university or other institute of learning.

Myron S. Huzan

Copyright statement

i The author of this thesis (including any appendices and/or schedules to this thesis) owns certain copyright or related rights in it (the "Copyright") and s/he has given The University of Manchester certain rights to use such Copyright, including for administrative purposes.

ii Copies of this thesis, either in full or in extracts and whether in hard or electronic copy, may be made *only* in accordance with the Copyright, Designs and Patents Act 1988 (as amended) and regulations issued under it or, where appropriate, in accordance with licensing agreements which the University has from time to time. This page must form part of any such copies made.

iii The ownership of certain Copyright, patents, designs, trademarks and other intellectual property (the "Intellectual Property") and any reproductions of copyright works in the thesis, for example graphs and tables ("Reproductions"), which may be described in this thesis, may not be owned by the author and may be owned by third parties. Such Intellectual Property and Reproductions cannot and must not be made available for use without the prior written permission of the owner(s) of the relevant Intellectual Property and/or Reproductions.

iv Further information on the conditions under which disclosure, publication and commercialisation of this thesis, the Copyright and any Intellectual Property and/or Reproductions described in it may take place is available in the University IP Policy (see `http://documents.manchester.ac.uk/DocuInfo.aspx?DocID=24420`), in any relevant Thesis restriction declarations deposited in the University Library, The University Library's regulations (see `http://www.library.manchester.ac.uk/about/regulations/`) and in The University's policy on Presentation of Theses.

All models are wrong,

but some are useful.

GEORGE E. P. BOX

Dedicated to:

Michael A. Huzan

Acknowledgements

My first and most important thank you is to my supervisor Dr Michael L. Baker. From the first coffee in the R1 coffee lounge in 2018 to the present, you have been an amazing inspiration and motivation throughout this PhD. Being thrown into the deep end with an I21 RIXS experimental session before even the beginning of my studies, I hope I showed you that I could swim, which is completely a result of your supervision. I am indebted to your guidance through all of the experimental beamtimes and opportunities you have provided me throughout my studies, along with the ever-growing checklist of beamlines that I have attended and also performed night shifts on. You have been there for the most challenging part of my life and been flexible when I have struggled but pushed me continually as I have needed it, and I can't thank you enough for all you have done.

My second thank you is to everyone who has been a part of the $M_{4,5}$ $L_{2,3}$ Baker Lab group. As the first student, I have seen everyone who has joined for a short or extended stay. From the laughs at the experimental facilities to lost luggage on the international return, you've all helped make this PhD a joy to undertake. To Tim, Rasmus, Nathan, Yuan, Joy, Sut Kei, JiaFu, Alban, ZhiBo, Ryan and Jin and to all others who have interacted with our group, thank you.

A special thank you is extended to Professor David Collison, a second supervisor who has always been available to discuss any scientific questions or directions to take and continue to push the research output of my studies; thank you. To the Manchester Chemistry Department and The University of Manchester at Harwell, while I started PhD life in Oxfordshire and moved just before a global pandemic, both groups always made me feel welcome wherever I resided. From running around chasing samples of upcoming beamtimes to administrative help, everyone has been of great help when I need it.

To Anton Jesche, Manuel Fix, and Franziska A. Breitner, without you, there would literally be no $Li_2(Li_{1-x}TM_x)N$ single crystal samples to even undertake any experiments on. While my knowledge of synthesis is extremely limited, one thing I do know is that you achieve remarkable single crystals that never fail to push the limits of experimental measurements and bring awe to the beamline scientists who see these

fascinating samples. Thank you for synthesising these remarkable samples; my thesis, by definition, wouldn't be what it is without them.

Throughout my PhD, I have had the privilege to travel and undertake incredible experimental work at world-leading research facilities. I would like to extend my gratitude to all beamline scientists and staff who have helped at any and all of the facilities I have had the joy of undertaking measurements at. To Peter, Matteo, Shu, Fred, Ke-Jin, Abhishek, Mirian, Myrtille, Edwige, Kristina, Monica and everyone else I might have missed at the Diamond Light Source, ESRF, SOLEIL, ILL and ISIS with whom I have had the pleasure to work with. An extra special thank you extends to Professor Hiroyuki Nojiri, who gratefully hosted me in the beautiful city of Tohoku, Japan, to perform remarkable experiments within his facility, a city and country I will not forget any time soon.

To my friends, a group of people who have seen me at my worst and been the reason I have been at my best. You all haven't stopped being there when I have needed some levity, and I couldn't ask for a better collection of humans than all of you.

Finally, my family, a small family, but more than anyone can ask for. You have all been there and provided insurmountable support and always were just a phone call away, Мама, Маріянна, Цьоця Ірка and Цьоця Стефка; thank you! Finally, finally, Тато, you're not here now, and that pains me every day, but I know you were proud of me because I heard you say it. You always had an interest in what I was doing throughout my studies and always flicked through any piece of work 'reading' it and nodding. This is the most significant and proudest piece of work I have ever done, so I will come and read it to you soon xx.

Myron S. Huzan

Organisation of Thesis and Contributing Authors

The submission of this thesis is presented in the style of a Journal Format Thesis. This approach combines journal-style publications, either as accepted or with an immediate view for submission, enclosed within a thesis introduction (Chapter 1) and conclusion (Chapter 5). Chapter 2 presents an accepted manuscript, DOI: 10.1039/d0sc03787g, in *Chemical Science*, **2020**. Chapters 3 and 4 are formatted in a journal style with an imminent view of submitting to publication.

The justification of this format of submission extends many branches of rationale. The work provided within this PhD constitutes primarily of experimental work performed at national- and international-synchrotrons; the nature of these facility experiments are highly competitive and expensive, requiring scientific publications to be at the heart of any experimental conclusion. Experimental reports naturally conclude a session at any facility, which leads to the formation and writing of a scientific journal. The collaborative nature, in conjunction with the cooperative interpretation of theory and experiment, leads to a scientific publication which can be actively and inherently beneficial to many colleagues and scientists. Scientific journal paper writing is a prerequisite in academia, and developing this skill throughout my studies will provide insurmountable benefits throughout my career. Therefore, upon the merit of all the above, it has been deemed most appropriate to submit a journal format thesis. The formation of Chapter 2 was co-written by the author of this thesis and Michael L. Baker, Chapters 3 and 4 was primarily written by the author of this thesis with input and comments provided by Michael L. Baker. There were also subsequent comments and input provided by all documented co-authors of Chapter 2.

Chapter 2, "Single-ion magnetism in the extended solid-state: insights from X-ray absorption and emission spectroscopy", integrates a broad range of spectroscopic techniques to unravel the electronic and geometric properties of $Li_2(Li_{1-x}Fe_x)N$. The majority of the experimental measurements were performed with myself as co-supervisor of the experimental session; these include powder XANES, EXAFS and Kβ XES, and single crystal $L_{2,3}$-edge XAS measurements at the I10-BLADE and I20-scanning

beamlines, Diamond Light Source, UK. Local contacts of the experimental session were Shusaku Hayama, J. Frederick W. Mosselmans and Peter Bencok; Michael L. Baker formed the rest of the experimental group as the primary supervisor. K-edge angular-dependent single crystal measurements were performed by Michael L. Baker at the SSRL, USA, with assistance provided by Leland B. Gee and Charles J. Titus. Quantum Espresso DFT calculations were performed by Matteo Aramini.

Chapter 3, "$L_{2,3}$-edge XAS and XMCD of linearly coordinated transition metal ions: a study of $3d$-$4s$ mixing and spin-orbit coupling", applies angular dependent single crystal $L_{2,3}$-edge XAS and XMCD measurements to comprehensively unravel orbital and magnetic contributions of $Li_2(Li_{1-x}TM_x)N$ where TM = Mn, Fe, Co, Ni and Cu. Experimental measurements were performed at the I10-BLADE beamline with myself as a co-supervisor with primary supervision provided by Michael L. Baker. Timothy G. Burrow and Sut Kei Chong completed the rest of the experimental team with Peter Bencok as the local contact during the experimental session. TD-DFT and CASSCF calculations were performed by myself, while Quantum Espresso DFT calculations were performed by Matteo Aramini.

Chapter 4, "Direct access to $3d$-$4s$ orbital hybridisation and single-ion magnetism with high-energy resolution RIXS", pushed the limit of high-resolution $2p3d$ Fe L_3-edge RIXS in an attempt to measure the anisotropic barrier of $Li_2(Li_{1-x}Fe_x)N$ and unravel hidden excitations from previously quantified core-level spectroscopic techniques. The experimental team consisted of myself, Michael L. Baker as the primary supervisor and Manuel Fix rounding out the experimental group. Measurements were performed at the I21 beamline at Diamond Light Source, UK, with local contacts Abhishek Nag, Mirian Garcia-Fernandez, Andrew C. Walters and Ke-Jin Zhou. Preliminary CASSCF measurements were performed by Nikolay Bogdanov.

All data processing supplied within this thesis was performed by myself; Demeter: XAS Data Processing and Analysis for EXAFS results and DAWN: next-generation data processing for RIXS measurements. All further plotting and spectroscopic processing were performed within MATLAB®.

I developed and applied charge-transfer ligand-field multiplet, TD-DFT and CASSCF calculations throughout the thesis with guidance from supervisors, literature material and workshops as a result of unconventional requirements of non-standard models.

Manuel Fix, Franziska A. Breitner and Anton Jesche from the University of Augsburg generously synthesised all transition metal doped lithium nitride samples.

The idea to apply core-level spectroscopy techniques to unravel $Li_2(Li_{1-x}Fe_x)N$ and $Li_2(Li_{1-x}TM_x)N$ electronic structure and magnetism questions has been provided by my primary supervisor, Michael L. Baker; with stimulating scientific discussions further provided by Marie-Anne Arrio and David Collison.

Chapter 1

Introduction

1.1 Single Ion Magnetism

Magnetic materials have been at the forefront of scientific importance since the dawn of the Information Age, with wide-ranging applications. The doubling of transistor density on integrated circuits every two years, in accordance with Moore's Law [1] has fundamentally advanced to the atomic level. Approaching this limit requires discrete magnetic units devoid of long-range magnetic ordering. The discovery of $[Mn_8^{III}Mn_4^{IV}O_{12}(CH_3COO)_{16}(H_2O)_4]$ [2], (Mn_{12}) introduced the field of "*Single Molecule Magnetism*" and with it a potential solution in the miniaturisation of binary magnetic storage.

Mn_{12} was first crystallographically characterised in 1991 [3] comprising of a ring of eight Mn^{3+} (S = 2) enclosing four Mn^{4+} (S = 3/2) ions, Figure 1.1. Magnetisation measurements revealed pronounced magnetic anisotropy resulting from a total spin ground state of $S = 10$ [3, 4]. Electron paramagnetic resonance (EPR) measurements confirmed the presence of a large zero-field splitting (ZFS), D=$-$0.5 cm^{-1} [3] lifting the $2S+1$ degeneracy of the ground-state M_S manifolds as described by the equation

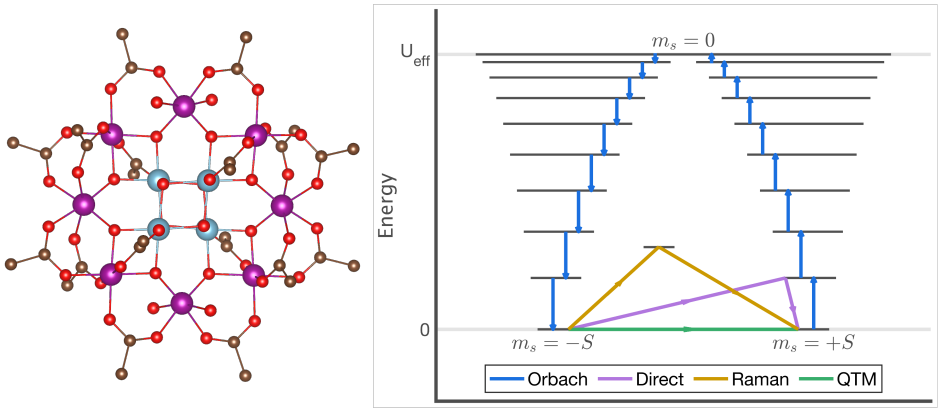

Figure 1.1. (*left*) Molecular structure of $[Mn_8^{III}Mn_4^{IV}O_{12}(CH_3COO)_{16}(H_2O)_4]$[2]; Mn^{III}, ●; Mn^{IV}, ●; C, ●; O, ● and Hydrogen omitted for clarity. (*right*) Schematic of a double well potential barrier of SMMs with representative through-, and over-barrier relaxation processes.

[5]:

$$\hat{\mathcal{H}} = D\left(\hat{S}_z^2 - \frac{1}{3}S\left(S+1\right)\right) + E\left(\hat{S}_x^2 - \hat{S}_y^2\right) \tag{1.1}$$

where $D = \frac{3}{2}D_{zz}$, and $E = \frac{1}{2}\left(D_{xx} - D_{yy}\right)$ represent the axial and transverse zero-field splitting parameters respectively corresponding to the traceless and symmetric D-tensor defined in a ZFS Hamiltonian description as, $\hat{\mathcal{H}}_{ZFS} = \hat{S}^{\top} \cdot D \cdot \hat{S}$.

The sign of the axial ZFS parameter dictates whether the magnetic anisotropy is easy-planar ($D > 0$) with $M_S = 0$ at lowest energy, or easy-axis ($D \leq 0$) corresponding to $M_S = \pm S$ as the lowest energy levels, Figure 1.1 [6]. The latter is a requirement of SMMs to achieve a preferential thermal population of the lowest-lying $M_S = \pm S$ states.

The size of the energy barrier as defined for integer spin ($U_{eff} = |D|S_z^2$), and non-integer spins ($U_{eff} = |D|(S_z^2 - 1/4)$) drove initial synthetic efforts towards maximising S for strongly spin-correlated clusters in increasing magnetic anisotropy [6]. This included a multitude of Mn and Fe derivatives [7]. Integral to the synthesis was the role of bridging ligands which promote strong exchange coupling between spins. This research led to large spin ground-states, including an $S = 83/9$ derivative of the cage Manganese compound, $[Mn^{III}_{12}Mn^{II}_{7}(\mu_4\text{-}O)_8(\mu_3,\eta^1\text{-}N_3)_8(HL)_{12}(MeCN)_6]Cl_2\cdot 10MeOH\cdot MeCN$ [8]. The U_{eff} of these complexes was substantially less than anticipated due to theoretical demonstration and subsequent experimental evidence in the proportionality of D to $1/S^2$ [9, 10]. Consequently, this approach of maximising S with increasingly elaborate polynuclear complexes with strong spin exchange-coupled ground-states was deemed unsuitable and led to greater efforts maximising anisotropic D values at the atomic level of mononuclear complexes [11]. This also brought a nomenclature change from single molecule magnets, SMM, to the more commonly utilised single-ion magnets, SIM, primarily referred to complexes that exhibit magnetic properties originating from single-ion anisotropy.

The magnetic relaxation rate of a SIM is defined as:

$$\frac{1}{\tau} = \frac{1}{\tau_0}e^{\frac{-U_{eff}}{T}} + AH^mT + CT^n + \frac{1}{\tau_{QTM}} \tag{1.2}$$

where the four terms are associated with Orbach, Direct, Raman and quantum tunnelling of magnetisation (QTM) relaxation processes [12, 13], Figure 1.1. The suppression of these relaxation mechanisms is crucial in reaching operational temper-

atures of magnetic retention feasible for prospective applications within high-density data storage [14, 15]. Orbach relaxation represents vibrational excitations of discrete steps over the potential barrier, U_{eff}, Figure 1.1. This thermally mediated process is dictated by an Arrhenius law and is typically characterised through AC-susceptibility measurements [5]. Slow magnetic relaxation requires an energy reversal barrier of the magnetic moment to be greater than thermal fluctuations. However, through-barrier relaxations are often observed at lower temperatures (Direct, Raman and QTM), which lead to increased relaxation rates and suppressed magnetic anisotropy barriers [16, 17]. These processes are significant at low temperatures, limiting the highest temperature where magnetic hysteresis can be observed. Through barrier relaxations occur due to the SIMs magnetic moment coupling with the lattice-environment *via* a one-step phonon emission (Direct) or two-step virtual phonon process (Raman) [18]. QTM is a resonant process through which the quantum mechanical overlap of ground- and/or excited-state wavefunctions results in through-barrier tunnelling and suppression of magnetisation. QTM can be enhanced with zero-field distortions, E (lowering of the ligand field symmetry), stray dipolar fields, and hyperfine couplings [14, 19–21]. These contributions are minimised through magnetic dilution [22, 23] and isotope enrichment [24, 25], while the utilisation of high symmetry environments significantly suppresses QTM. Ligand field optimisation is paramount in reducing magnetic relaxation rates, and there exists no shortage of reviews for $3d$ [26–29], and $4f$ [30–34] complexes in the optimisation of these parameters.

The chemical design of SIMs drove to increase U_{eff}. However, increasing operational temperatures was constrained by the prevalence of through barrier relaxation processes, thus limiting comparative insights between complexes. Conversely, the characterisation of a magnetic blocking temperature, T_B, below which the magnetisation of a SIM persists upon removal of applied fields, has been deemed more appropriate. Several competing definitions of T_B exist within the literature [31]; i) temperature bifurcation of zero-field and field cooled measurements (temperature sweep-rate dependent) ii) highest temperature of a hysteresis loop within magnetisation measurements (field sweep-rate dependent), and iii) temperature of measurable magnetic relaxation greater than 100 seconds. As the inaugural molecular magnet, Mn_{12} exhibited magnetic hysteresis below 2.1 K with relaxation times on the order of months [2, 3], which grows to the order of 50 years as the temperature is reduced to 1.5 K[35]. This result provided the template and inspiration for future systems to exceed.

Typically, first-row transition metal ions experience quenching of the orbital magnetic moment due to energetically favourable Jahn-Teller distortions [36, 37]. The

presence of ZFS within these systems is thus a manifestation of ground and excited electronic state mixing, resulting in a weak second-order perturbation upon the ground state of parabolic energy dependence [6]. Comparatively, targeting lanthanides that exhibit spin-orbit coupling effects of valence $4f$ orbitals has resulted in remarkable single-molecule properties. Mononuclear lanthanide SMMs were first demonstrated to exhibit a slow relaxation of magnetism through the $[LnPc_2]^-\cdot TBA^+$ (Ln = Tb, Dy; Pc = dianion of phthalocyanine; TBA^+= $N(C_4H_9)_4^+$) [38] double-decker complexes. Screening of $4f$ electrons by $5d$ and $6s$ orbitals largely conserve orbital angular momentum leading to spin-orbit coupling described by the Russell-Saunders scheme defining the total angular momentum, J of integer steps from $|L - S|$ to $|L + S|$. Projection of the J multiplets are perturbed $(2J + 1)$ by the crystal field, and with an appropriate selection of coordination environments, anisotropic barriers can exceed 1000 cm^{-1}. For instance, in 2017, a Dy(III)-SMM achieved a breakthrough energy barrier of U_{eff} = 1,223 cm^{-1} (151.63 meV) [39], which was very shortly surpassed by a derivative complex achieving a U_{eff} = 1,277 cm^{-1} (158.33 meV) [40] . Strategies in increasing magnetic anisotropy rely on the coordination environment and comprehension of the crystal field symmetries. While these Dy SIM results far exceed any previously observed energy reversal barriers of transition metal ion SIMs, this thesis will focus on how by exploiting the symmetry of transition metal ions can exhibit first-order spin-orbit coupling comparable to lanthanide counterparts.

1.1.1 Linear Transition Metal Complexes

The electronic structure of open-shell transition metal ions can be described using semi-empirical models of ligand field theory (LFT) [41, 42] as an interpretational technique to comprehend experimental results [43]. Application of LFT has been extensively tested with the insurmountable success of spectroscopic results ranging from the laboratory with UV-VIS to large-scale facilities and X-ray spectroscopic techniques [44]. With the development and advancements of quantum chemistry methods, the application of LFT models has extended to density functional theory and post-self-consistent field *ab initio* methods, where discrepancies between crystal field theory are apparent; including linear metal dihalides, MX_2 (M = Ca through to Zn; X = F, Cl) [45].

Crystal field theory predicts the raising and labelling of d-orbital degeneracies through the electrostatic potential of the surrounding atoms, Figure 1.2. Ligand field theory builds upon this purely electrostatic model to introduce molecular orbital principles to describe metal-ligand bonding contributions appropriately. Orbital degen-

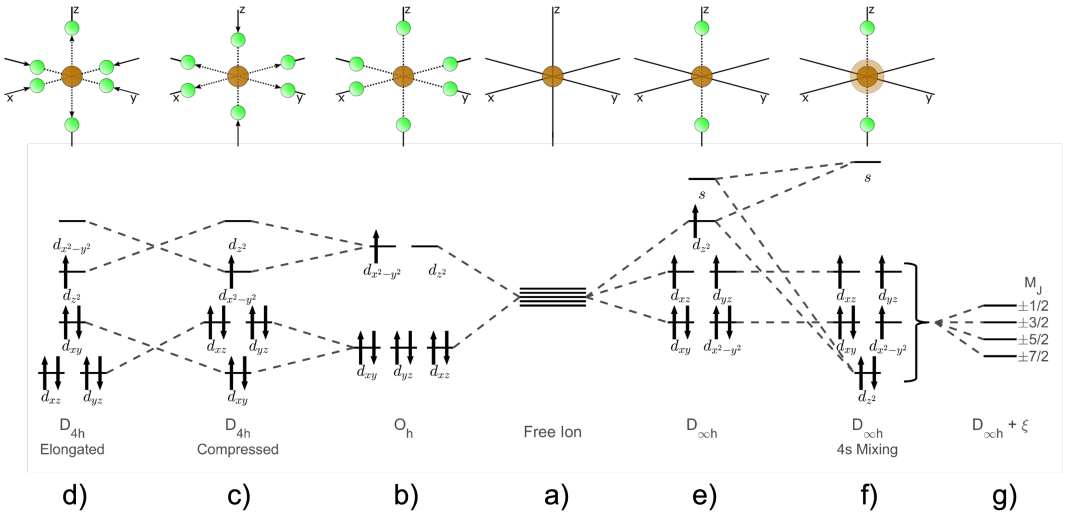

Figure 1.2. Energy level diagram utilising a point charge approximation representing transition metal d orbital degeneracy of several ligand field environments. (a) Free ion (b) Octahedral, O_h (c, d) Octahedral Jahn-Teller distorted compression and elongation, D_{4h}. (e) Linear, $D_{\infty h}$ (f) Linear with $3d_{z^2}$-$4s$ hybridisation, stabilising $3d_{z^2}$ orbital facilitating first order spin-orbit coupled d^7 ground state, (g).

eracy of a linear coordination, $D_{\infty h}$ corresponds to a lowest energy E_{2g} doublet, $(3d_{xy}, 3_{dx^2-y^2})$ followed by an intermediate energy E_{1g} doublet $(3d_{xz}, 3d_{yz})$ and an A_{1g} singlet $(3d_{z^2})$ of highest energy [46]; representing a bonding order of $\delta < \pi < \sigma$. Deviation of this ordering was first addressed through *ab initio* calculations of MX_2 complexes with orderings of $\delta < \sigma < \pi$ or even $\sigma < \delta < \pi$ [45]. These energetic orderings of the $3d$ orbitals are predicted as a result of strong metal-ion $3d_{z^2}$-$4s$ orbital hybridisation through quantum chemistry calculations, reducing the destabilisation of $3d\sigma$ anti-bonding orbital and lowering the energy of the $3d_{z^2}$ orbital [45, 47, 48]. This counter-intuitive ordering represents some limitations within ligand field theory where modern theories such as cellular ligand field theory [49, 50] or atomic overlap models [51] more appropriately, and correctly account for strong orbital interactions [52, 53].

The unusual ordering of electronic ground-states has wide-ranging implications within molecular magnetism; a prominent example of this are the linear Fe(II) analogues synthesised by Zadrozny et al. [54]. These complexes exhibited spin-reversal barriers in excess of 100 cm^{-1} each with a $S = 2$ quintet ground-state but exhibit large quantum tunnelling of magnetisation. Kramers theorem [55] predicts half-integer spin systems to remain doubly degenerate in the absence of magnetic fields, thus targeting the synthesis of the first monovalent linear transition metal complex to exhibit slow magnetic relaxation, $[Fe(C(SiMe_3)_3)_2]^-$, Figure 1.3 [56]. Deviation of linearity introduces symmetry permitting QTM; however, the success of this complex drove the targeted synthesis of analogue complexes.

$[Fe(C(SiMe_3)_3)_2]^-$ exhibits a degenerate ^4E ground-state with first-order spin-orbit

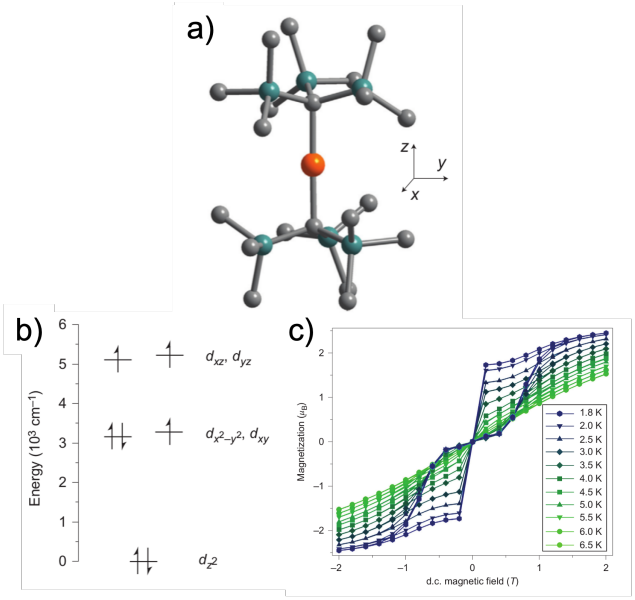

Figure 1.3. (*a*) Molecular structure of $[Fe(C(SiMe_3)_3)_2]^-$ (*b*) $3d$ orbital energies determined from *ab initio* calculations. (*c*) Magnetisation measurements displaying waist-restricted hysteresis loops for temperatures below 6.5 K [56].

coupling leading to the splitting of four Kramers doublets, in order of increasing energy, represented by the quantum number $M_J = \pm 7/2, \pm 5/2, \pm 3/2$ and $\pm 1/2$ (where J is the total angular momentum). Experimental evidence of the T_B was demonstrated with a discontinuous decrease of $\chi_m T$ below 4.5 K with and without applied d.c. fields; and the presence of magnetic hysteresis below 6.5 K, performed with an average sweep rate of 50 Oes^{-1}, Figure 1.3c [56]. Despite targeting the synthesis of Kramers ions, the presence of quantum tunnelling is still pronounced as a waist-restriction of the hysteresis loops within variable-field magnetisation measurements of $[Fe(C(SiMe_3)_3)_2]^-$, Figure 1.3c. Explanation of this is highlighted through the deviation in the linearity of the C-Fe-C bond angle of 179.2(2)° leading to the possibility of Renner-Teller vibronic coupling [37, 57] facilitating mixing of the ground $M_J = \pm 7/2$ states. Despite this, the determination of an U_{eff} = 226 cm^{-1} as calculated through Orbach relaxation via the first excited doublet, $M_J = \pm 5/2$ greatly exceeded any previous mono (181 cm^{-1}) [54] or poly (67 cm^{-1}) [58] -transition metal systems. This discovery led to further efforts in enhancing magnetic anisotropy for linear transition metal complexes, including $[Co(C(SiMe_3)_3)_2]$ [10] as a prospective Co(II) analogue with an inherently larger spin-orbit coupling constants, 553 vs 361 cm^{-1} [10, 59] and thus expected superior SIM properties.

The approach in reaching the single ion magnetic anisotropy limit for $3d$ ions requires targeted and meticulous control of ligand field environments to achieve a maximal orbital angular momentum of $L = 3$. To achieve this ground-state orbital degeneracy requires an odd electron count in both the $d_{x^2-y^2}, d_{xy}$ ($m_l = \pm 2$)

and d_{xz}, d_{yz} ($m_l = \pm 1$) orbitals. Naturally, this would require violating the Aufbau principle, which predicts electron filling in order of energy levels. The competing effects of ligand field stabilisation and interelectronic repulsions are often neglected with transition metal electronic structure considerations. Within a regime where these effects are comparable preferential ordering of $(d_{x^2-y^2}, d_{xy})^3(d_{xz}, d_{yz})^3$ over $(d_{x^2-y^2}, d_{xy})^4(d_{xz}, d_{yz})^2$ minimises electron-pairing considerations, while maximising orbital angular momentum as dictated by Hund's rule [10, 60]. *ab initio* calculations of [Co(C(SiMe$_3$)$_3$)$_2$] predicts a sufficiently weak ligand field reordering the orbital occupancy to $(d_{x^2-y^2}, d_{xy})^3(d_{xz}, d_{yz})^3(d_{z^2})^1$ corresponding to the desired orbital angular momentum of $L = 3$. Synthetic challenges delayed the inevitable breakthrough of a Co(II) molecule with non-Aufbau ordering with record anisotropic barriers. Bunting et al. [60] synthesised Co(CoSiMe$_2$OR)$_3$ (Figure 1.4) and experimentally verified a well-isolated $M_J = 9/2$ ground-state separated by an excited $7/2$ state at 450 cm^{-1} exhibiting the largest barrier to spin-relaxation to date of a TM-SIM.

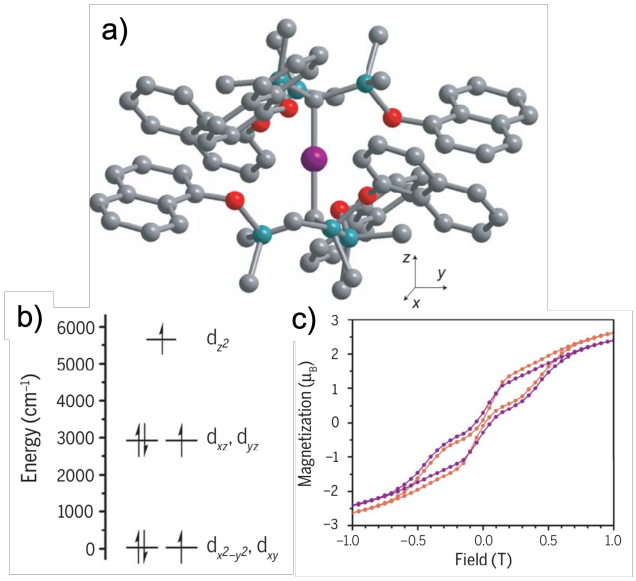

Figure 1.4. (*a*) Molecular structure of Co(CoSiMe$_2$OR)$_3$ (*b*) 3*d* orbital energies determined from *ab initio* calculations. (*c*) Variable-field magnetisation measurements display waist-restricted hysteresis loops. Sweep rate of 32 Oe/s and temperature of 1.8K for Co(CoSiMe$_2$OR)$_3$, ● ; and a magnetically dilute analogue, Co$_{0.02}$Zn$_{0.98}$(CoSiMe$_2$OR)$_3$, ● [60].

1.1.2 Li$_2$(Li$_{1-x}$Fe$_x$)N

Lithium nitride, Li$_3$N, first synthesised in 1935 [61] exhibits a unique hexagonal symmetry and has proved an exemplary compound to study fascinating magnetic properties as a dopant host matrix lattice. Formally characterised with a space group symmetry of P6/mmm through X-ray diffraction techniques [62], Li$_3$N crystallises as a hexagonal lattice of Li$_2$N alternating with lithium planes bonding solely to the central nitrogen atom within the unit cell parallel to the crystallographic c axis, Figure 1.5.

Initial interest in the compound was sparked as a promising solid electrolyte within battery research owing to its considerably high ionic conductivity [63–66]. Further scientific contributions extend but are not limited to atmospheric CO_2 conversion [67], preparative organic and organometallic chemistry [68], and hydrogen storage [69]. This introduction will focus on the exceptional magnetic properties Li_3N facilitates as a host lattice and the impact within single-ion magnetism that can be contributed.

The first reported synthesis of ternary compounds doped in the crystalline form of Li_3N began in 1949 with Co, Ni and Cu from X-ray powder investigations [70]. Subsequent re-investigations [71] of polycrystalline samples would propose a transition metal series, TM = Mn, Fe, Co and Ni [72, 73], exhibiting a 1+ valence through K-edge fingerprinting of XANES edge shifts (Detailed introduction of X-ray spectroscopy provided in Section 1.2 below). The intense pre-edge present in the Fe K-edge XANES measurements are reassigned within the first publication of this thesis.

The observation of a μ_{eff}/Fe exceeding the expected spin-only value for an Fe(I) ion from powder SQUID magnetometry measurements of concentrated $Li_2(Li_{1-x}Fe_x)N$ (x = 0.21) indicated the presence of unquenched orbital momentum [74]. This result was theorised within a theoretical framework utilising the local density approximation (LDA + U) to an electronic ordering indicative of that to linear dihalides (as described above, Section 1.1.1), $d_{z^2} < d_{x^2-y^2}, d_{xy} < d_{xz}, d_{yz}$. Within this relativistic scheme, the sensitivity of electronic ordering is not correlated to Hubbard U or magnetic exchange, J (provided they are within reasonable limits); rather, the results predict huge hyperfine magnetic fields and large magnetic moments resulting from strong orbital contributions [75, 76].

Experimental evidence of pronounced magnetocrystalline anisotropy was previously unsuccessful due to synthetic limitations [77] of single crystals until Jesche and Canfield [78]. developed single crystal growth techniques utilising Li-rich flux methods achieving large (mm^2) single crystal synthesis of $Li_2(Li_{1-x}TM_x)N$, Figure 1.5 [78]. Metallic doping of Li_3N substitutes a Li-ion site at the Wyckoff 1*b* position corresponding to a local two-coordination, $D_{\infty h}$ symmetry. Doping of transition metal ions (TM = Mn, Fe, Co [79], Ni [80] and Cu [80], (Figure 1.6) is achievable for a broad range of concentrations and is verified by inductively coupled plasma mass spectrometry [78].

Figure 1.7 shows variable-field magnetisation measurements of $Li_2(Li_{1-x}Fe_x)N$ [82] which have become synonymous in the experimental identification of SIM properties. Magnetic hysteresis persists up to 16 K and coercive fields of 3.4 T below 10 K constitute the largest temperature hysteresis reported for a TM-SIM. Furthermore,

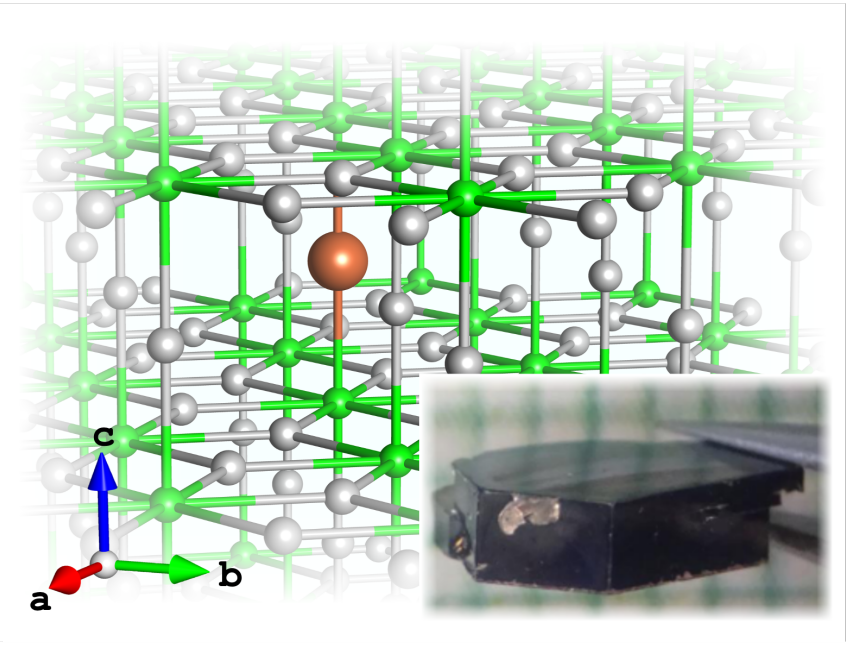

Figure 1.5. Structure of $Li_2(Li_{1-x}Fe_x)N$; Illustration representative of a metallic dopant site within an extended solid-state matrix. Fe, ● ; N, ● ; Li, ● . *(Inlay)* Li_3N single crystal upon a millimetre background [81].

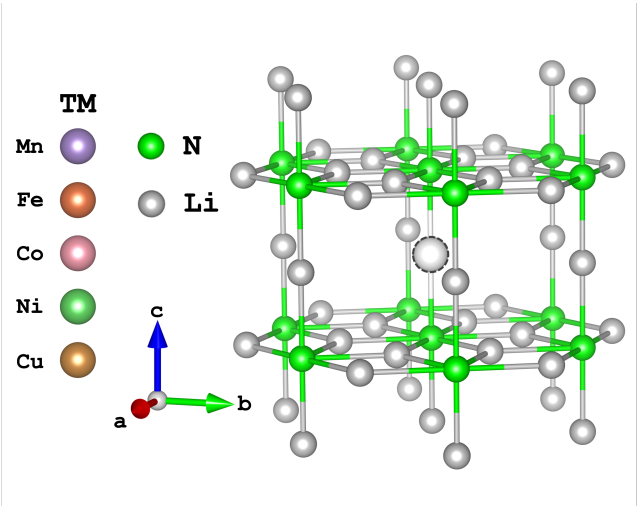

Figure 1.6. Structure of $Li_2(Li_{1-x}TM_x)N$; TM substitution within α-Li_3N matrix at the $1b$ Wyckoff position.

discrete steps as H approaches zero-field and near-temperature independence below $\sim$10 K indicates a magnetic relaxation regime dominated through QTM, indicative of SIMs. Pronounced magnetic anisotropy is observed with the preferential direction of magnetisation $H \parallel c$ supporting easy-axis anisotropy. Experimental quantification of $\mu_{\text{sat}}^{\parallel c} = 4.8(4)\mu_B$ and $\mu_{\text{eff}}^{\parallel c} = 6.5(4)\mu_B$ was determined through variable-field magnetisation (2 K) and temperature-dependent inverse magnetisation (200 - 300 K) measurements respectively [82]. These values are in good but contrasting agreements with magnetic moment calculations of a transition metal ion:

$$\mu_{\text{eff}} = \sqrt{4S\,(S+1) + L\,(L+1)}\mu_B \tag{1.3}$$

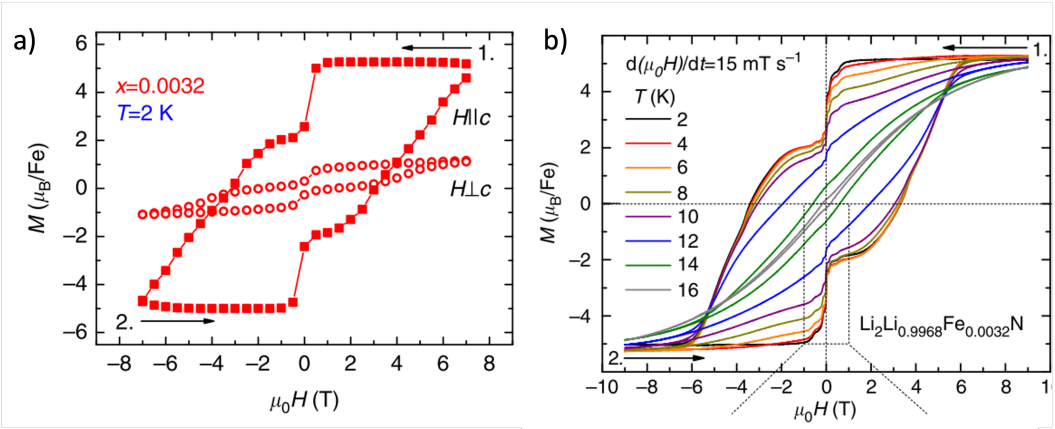

Figure 1.7. (*a*) Variable-field magnetisation measurements with pronounced single crystal magnetic anisotropy of $Li_2(Li_{1-x}Fe_x)N$ representing easy-plane magnetisation with greater M saturation $\parallel c$. (*b*) Temperature dependent variable-field magnetisation measurements of $Li_2(Li_{1-x}Fe_x)N$, $H \parallel c$. Distinct steps within magnetisation loops indicative of QTM upon approaching $H = 0$ [83].

$$\mu_{\text{eff}} = g_J \sqrt{J\,(J+1)}\mu_B \tag{1.4}$$

where μ_B is defined as the Bohr magneton and g_J the Lande-g factor through the equation:

$$g_J = \frac{3}{2} + \frac{S\,(S+1) - L\,(L+1)}{2J\,(J+1)} \tag{1.5}$$

Equation 1.3 represents the magnitude of a magnetic moment of a free ion with quantum numbers L and S while Equation 1.4 is derived with the inclusion of spin-orbit coupling representative with a total angular momentum, J. Equation 1.3 is in good agreement of a free ion with ground-state quantum numbers $L = 2$ and $S = 3/2$ resulting in $\mu_{\text{eff}} = 4.58\mu_B$ and is comparable to previous LDA + U calculations [75]. Whereas Equation 1.4 requires a Hund's rule couple scheme maximising angular momentum, $L = 3$ and $S = 3/2$, $\mu_{\text{eff}} = 6.6\mu_B$ for a fully spin-orbit coupled d^7 system. These contrasting results highlight the limitations in utilising rudimentary magnetic moment calculations.

AC-susceptibility measurements identify Orbach relaxation with an energy barrier to spin-reversal to be $\Delta E/k_B = 476(21)$ ($T > 10\,\text{K}$) [83] and 1123 K ($T > 25\,\text{K}$) [81] for single crystal dopants of $x \sim 0.001$ and ~ 0.3 respectively. These results are comparable to other mononuclear Fe(I) SMMs, but lower than many Dy(III) complexes [84]. Contrastingly, a comparison of relaxation times within a QTM regime reveals $Li_2(Li_{1-x}Fe_x)N$ is comparable to the highest performing Dy(III) complexes with τ being of the order of $\sim 10^4$ s. Quantification of magnetic relaxation processes for $Li_2(Li_{1-x}Fe_x)N$ extends ten orders of magnitude with the sum of Orbach, Raman

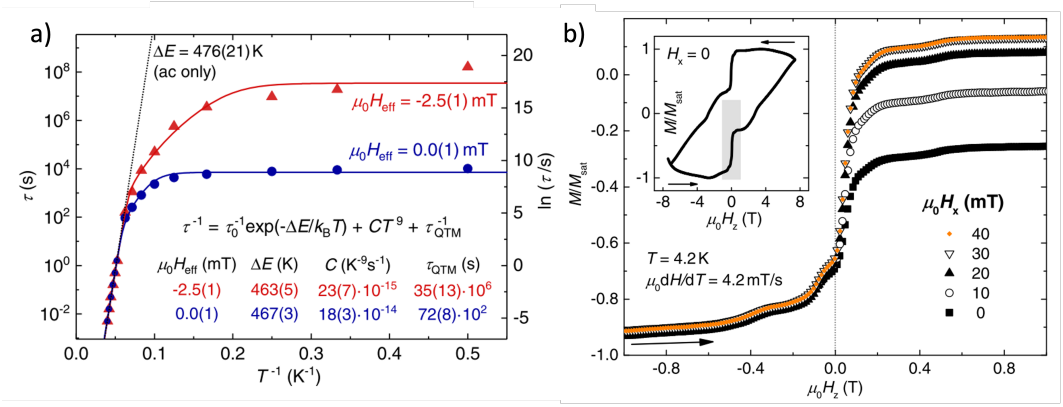

Figure 1.8. (*a*) Nominal zero (*blue*) and applied (*red*) longitudinal field comparison of magnetic relaxation, τ of $Li_2(Li_{1-x}Fe_x)N$ (x = 0.001). Fits representative of relaxation dependencies, including Orbach, Raman and QTM. (*b*) Isothermal magnetisation measurements within applied transverse fields, $\mu_0 H_x$, (*Inlay*) highlighting QTM region of interest as H approaches 0 [83].

and QTM, Figure 1.8a [83]. Further spin-reversal dependencies were observed with applications of transverse and longitudinal fields. QTM resonances were identified to collapse upon application of a 3 mT longitudinal field extending magnetic relaxation by an order of 10^4 s, Figure 1.8a. This extreme magnetic field sensitivity illustrates a narrow energy splitting, 1.7 μeV, of the ground-state $M_J = \pm 7/2$ doublets and lifting of ground-state degeneracy through a Zeeman splitting. The application of transverse fields collapses the magnetic coercivity by increasing tunnelling rates, Figure 1.8b. This is emblematic of transverse anisotropy effects resulting from non-linear environments or indicative of stray dipolar or hyperfine coupling fields, highlighting the imperativeness in minimising these processes to circumvent QTM.

Scientific Motivation

Through meticulous control of ligand field environments, TM ions can be prepared with unique low valences and non-Aufbau orderings, resulting in large magnetic anisotropies [56, 60, 85]. Doping of transition metal ions within an extended solid-state crystal provides an alternative approach to explore single-ion magnetism relative to conventional coordination chemistry techniques. $Li_2(Li_{1-x}Fe_x)N$ exhibits exceptional magnetic properties with prospective applications within magnetic data storage [86], quantum computation [87] and magnetic field sensing [88]. Several theoretical approaches predict magnetic anisotropy resulting from unquenched orbital momentum and $3d$-$4s$ orbital hybridisation. However, concrete experimental evidence has been limited [89, 90]. Quantification of orbital hybridisation of $Li_2(Li_{1-x}Fe_x)N$ and comparable TM-SIM complexes is also currently limited to theoretical approaches. To advance the understanding of linearly coordinated TM ions, experimental quantification of electronic structure is thus proposed for $Li_2(Li_{1-x}TM_x)N$ where TM = Mn,

Fe, Co, Ni and Cu.

The extended solid-state system $Li_2(Li_{1-x}Fe_x)N$ represents the convergence of several captivating branches of research pursuits within *molecular magnetism* into a single system. Theoretical determination of an unquenched orbital momentum drives the description of spin-orbit coupling into the Russel Saunders LS coupling scheme, a highly favourable direction as demonstrated by high-performance Ln-SIMs. Therefore, targeting these materials provides the prospect of rare-earth-based alternatives to permanent magnets and SIMs. The insulating Li_3N crystal is proposed to establish a truly isolated atomic system for TM dopants, with average TM-TM distances of $\sim$36 Å when $x = 0.001$ [83]. This low doping concentration is thus proposed as single-ion in nature, facilitating the unravelling of magnetic properties without ambiguities from stray dipolar coupling. This study of $Li_2(Li_{1-x}Fe_x)N$, extending to $Li_2(Li_{1-x}TM_x)N$ derivatives, aims to provide a comprehensive understanding of linear transition metal complexes in the continued pursuit of targeting larger spin-reversal energy barriers and minimising relaxation processes for SIMs.

Upon approaching elevated blocking temperatures of SIMs, the general scientific motivation within the international research community is directed towards the deposition of such coordinated complexes upon surfaces [86, 91, 92]. Alternatively, high symmetry host lattices [93], such as Li_3N, are readily being explored as alternative approaches to coordination chemistry techniques manifesting from the direct control of local symmetries and lattice phonon dispersions available. However, the nature of dopant systems limits the application of frequently utilised laboratory techniques in their characterisations. Comprehensive experimental quantification of transition metal valence is still debated within the literature, TM(I) vs TM(II) [79, 94–97] with further uncertainty on the effect of Li-ion vacancy formation within Li_3N [98–100]. Therefore, the application of element selective spectroscopic techniques through synchrotron sources are proposed to characterise $Li_2(Li_{1-x}TM_x)N$ comprehensively. X-ray spectroscopy is introduced below to pursue experimental quantification of the previously undetermined geometric and electronic structure of $Li_2(Li_{1-x}Fe_x)N$ and TM-dopant equivalents to interpret the observed exceptional magnetic properties comprehensively.

1.2 X-ray Spectroscopy: An Overview

The arrival of 4th generation synchrotron facilities promises to have significant implications in many scientific disciplines [101]. Light-matter interactions can be broadly characterised into absorption, elastic scattering and inelastic scattering events, each of which are harnessed at synchrotron facilities around the globe to answer a plethora of scientific questions. X-ray energies are loosely characterised into soft (0.1 - 2 keV), hard (>4 keV) and tender, the murky middle that branches the two. Depending on the question at hand, the use and application of X-rays are harnessed in different ways. Within this thesis, a broad range of techniques are utilised to determine the electronic and magnetic properties of $Li_2(Li_{1-x}TM_x)N$, along with further recommended literature [102–104], these concepts will be introduced below.

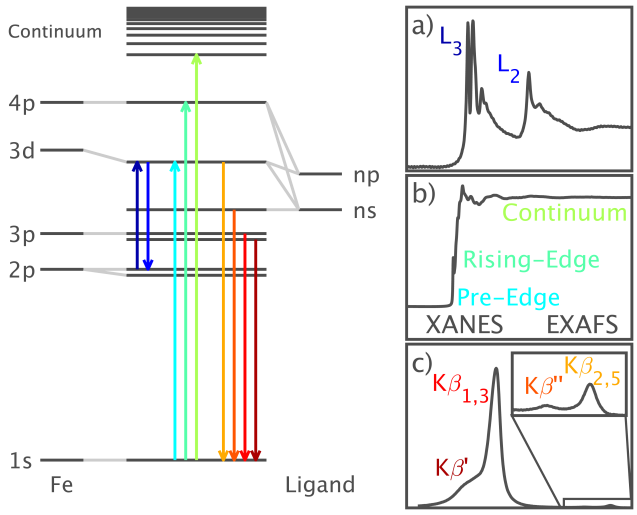

Figure 1.9. Illustration of several X-ray spectroscopic techniques with their associated transitions. (*a*) $L_{2,3}$-edge absorption probes unoccupied $3d$ orbitals. Spin-orbit coupling within the $2p^5$ core-hole splits the absorption into the $2p_{1/2}$ and $2p_{3/2}$ edges. (*b*) K-edge pre-edge, edge and EXAFS correspond to $1s$ absorptions into unoccupied $3d$, $4p$ and continuum, respectively. (*c*) Following the ejection of a $1s$ electron, Kβ XES involves the decay of Fe $3p$ and occupied valence electrons into the $1s$ core-hole [90].

1.2.1 X-ray Absorption Spectroscopy

X-ray absorption is a core-level technique that describes the excitation of an electron from an incoming photon to unoccupied states above the Fermi energy level. The strength of absorption interaction is dictated by the absorption cross-section of the incident element, which exhibits discontinuous logarithmic reduction as a function of energy, as described by the Beer-Lambert Law, corresponding to absorption edges.

Transition Metal K-edge XAS

K-edge, X-ray absorption spectroscopy, involves the excitation of a $1s$ electron into unoccupied states, Figure 1.9b [105–107]. The spectrum is categorised into pre-edge, main-edge and post-edge regions, each sensitive to various chemical and physical properties. The pre-edge region is a quadrupole allowed, $1s \rightarrow 3d$ transition frequently used to identify valence, and spin ground-states of TM ions due to significant variation of crystal field multiplet effects resulting in a characteristic fingerprint [108]. X-ray Absorption Near-Edge Structure, XANES refers to the main-absorption edge region of the spectrum, which describes the dipole allowed, $1s \rightarrow 4p$ transitions. The XANES is a projection of the partial unoccupied density of states, with sensitivity to ligand field splitting of the p-orbitals. Finally, Extended X-ray Absorption Fine Structure, EXAFS corresponds to the post-edge, which describes the ejection of a $1s$ electron into the continuum states. Modulation of photoelectronic scattering off neighbouring atoms experiences interference effects upon trajectory back to the absorbing atom. Radial distances extending to the first coordination sphere can be readily inferred through Fourier transformation into k-space [109–111].

The energy resolution of K-edge absorption is limited by the excited state lifetime broadening as described by the energy uncertainty of the $1s$ core-hole, described through the Heisenberg uncertainty principle. This results in significant Lorentzian broadening of the spectra and smearing of spectral features. Spectral resolution enhancement can be achieved by measuring both the incident and scattered radiation with high-resolution emission spectrometers; this technique is known as high energy resolution fluorescence detection, HERFDs [112]. Additionally, one can minimise these effects by selecting alternative absorption edges. Such as the $L_{2,3}$-edge, with a core-hole lifetime limited by the $2p$ orbital, which is considerably longer and conversely results in sharper resolved features.

$L_{2,3}$-edge XAS

$L_{2,3}$-edge X-ray absorption involves the excitation of a $2p$ electron into unoccupied d states, Figure 1.9a [107]. The $3d$ valence electrons of transition metal complexes determine the chemical and physical properties. Through direct access to these states with $L_{2,3}$-edge, XAS bonding contributions and electronic structure can be readily studied. An identifying feature of $L_{2,3}$-edge spectra are the L_2 and L_3-edges which are a result of spin-orbit coupling of the $2p^5$ final state ($J = L \pm S$) into $2p_{1/2}$ and $2p_{3/2}$ respectively. The fine structure observed within these edges are the product of

multiplet structure of partially filled d^n and $2p^5$-orbitals, which can be derived for the system through *ab initio* calculations [113, 114].

1.2.2 X-ray Magnetic Circular Dichrosim

Dichroism derives from the Greek word "*dikhroos*" which describes a material exhibiting colour orientation dependence upon the stimulation of light. This can be visualised spectroscopically through the incidence and difference of right and left-circularly polarised light, X-ray magnetic circular dichroism (XMCD) or X-ray magnetic linear dichroism (XMLD), which describes orthogonal orientation incidence of linearly-polarised light relative to a quantised axis [115]. The former is utilised within the analysis of this thesis and will be introduced below.

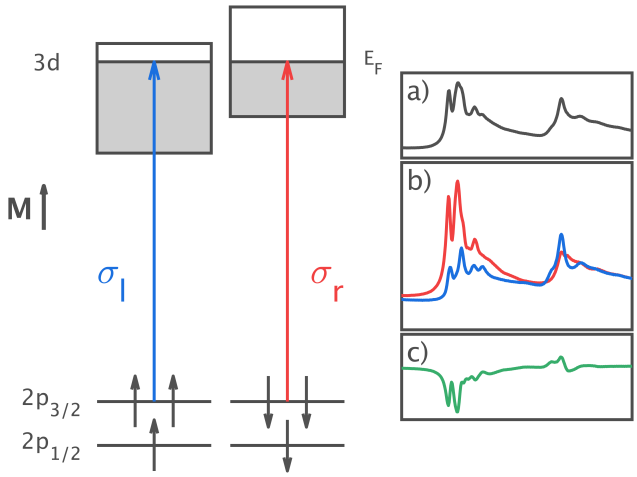

Figure 1.10. Illustration of the orbital transitions associated to $L_{2,3}$-edge X-ray Magnetic Circular Dichroism (XMCD). Spin-polarised photo-excitation of $2p$ orbitals into unoccupied $3d$ density of states. Absorption of left (right) circularly polarised light corresponds to excitation of spin up (down) photoelectron. (*a*) Isotropic absorption spectrum, $(\sigma_l + \sigma_r)$ equivalent to $L_{2,3}$-edge XAS, Figure 1.9a. (*b*). X-ray absorption spectra of left and right circular polarisation aligned perpendicular to magnetisation vector. (*c*) XMCD spectra $(\sigma_r - \sigma_l)$ representative of the asymmetry between spin density of states.

XMCD relies on the presence of spin polarisation-dependent selection rules to exploit differences in spin density of state populations of the frontier orbitals. The detection of X-ray absorption spectra is typically undertaken within the application of an external magnetic field. Field directionality is reversed or circular polarisation helicity is flipped (Figure 1.10b) to achieve an XMCD signal, Fig. 1.10c. This is based upon the principle of the selection rule, $\Delta m = \pm 1$ where m is the magnetic orbital quantum number and left (σ_l) and right (σ_r)-circular polarisation promotes $\Delta m = +1$ and -1 respectively. Interpretation of XMCD results draws from the ratio of the L_3/L_2-edge XMCD intensities, which is attributed to the presence of spin-orbit coupling; and sum rule analysis (with some limitations [116–118]), to interpret the expectation values of

$\langle S_z \rangle$ and $\langle L_z \rangle$ of the ground state manifolds [119, 120]. Comprehensive interpretation applies charge-transfer ligand field multiplet theory and semi-empirical parameters to deduce exchange fields and ligand field contributions of magnetic materials to add an extra depth of knowledge to experimental results.

1.2.3 Resonant Inelastic X-ray Scattering

The advent of high-brilliance sources and continual engineering advancements in monochromator and spectrometer resolutions facilitates high-resolution unravelling of numerous electronic and magnetic phenomena; where previously, this was limited to solely inelastic neutron scattering (INS) experiments [121]. Resonant inelastic X-ray scattering (RIXS) is a photon-in, photon-out technique built upon the foundations of resonant Raman spectroscopy [122]. By measuring both incident and emission photon energies, the spectral resolution of discrete excitations can exceed 35 meV [123]. This resolution far exceeds conventional core-hole spectroscopy techniques as a result of being intrinsically limited by the final-state lifetime as opposed to the core-hole lifetime.

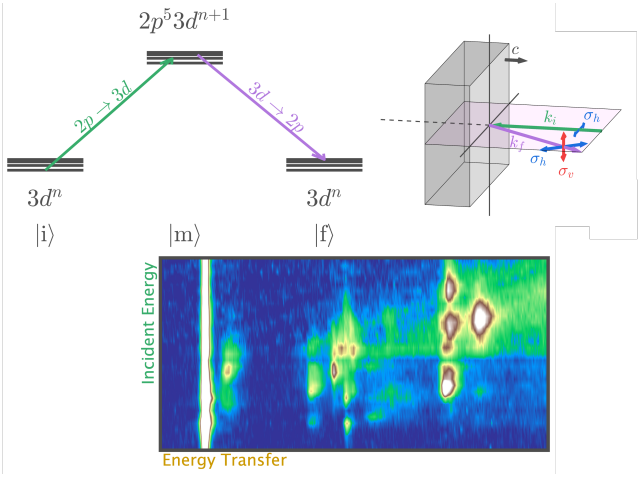

Figure 1.11. Illustration of the 2-step photon processes associated with Resonant Inelastic X-ray Scattering (RIXS) alongside schematic of geometry for the measurement for single crystal RIXS. Incident energy (E_I) corresponds to excitations of 2p electrons into unoccupied 3d valence orbitals. Emission energy (E_F) represents relaxation of excited states into the empty core-hole. Energy transfer ($E_T = E_I - E_F$) constitutes the energy difference between incident and emission intrinsic to the excitations under investigation.

Beyond the engineering accomplishments that high-resolution RIXS beamlines achieve, there are several additional dimensions of freedom in which to explore [124–127]. Vibronic (phonons), electronic (d-d and charge-transfer) and magnetic (magnons) fluctuations each can exhibit significant polarisation and momentum transfer dependencies of the incident and scattering photons which directly reflect the nature of the propagation [128, 129]. Identifying these characteristics requires an addi-

tional dimension of complexity to the analysis; however, the feasibility of unravelling electronic and magnetic features which are inaccessible with XAS enhances the fundamental understanding of the system. Equally sophisticated and flexible theoretical approaches are required to characterise the rich excitations observed by RIXS experimental measurements; this is introduced in the following section by employing the semi-empirical charge-transfer ligand field multiplet theory.

1.2.4 Experimental Considerations

The majority of the experimental data collected within this thesis was undertaken at the I21 [123], I20-scanning [130] and I10 beamlines at Diamond Light Source, with contributing measurements from the BL9-3 beamline at SSRL.

Detection

Direct quantification of X-ray absorption is achieved with transmission detection harnessing the Beer-Lambert Law, $I = I_0 e^{-\mu(E)d}$ where intensity before, I_0 and after I light-matter interaction corresponds to the absorption coefficient, $\mu(E)$ of the material. However, this technique is challenging to achieve since it requires strict sample homogeneity for the hard X-ray regime; or $\sim$ sub μm-level sample thickness at the soft X-ray regime, which naturally presents experimental and synthetic challenges [44]. Therefore, detection of soft X-ray absorption is routinely achieved through secondary processes. Relaxation of excited state atomic absorptions can occur *via* X-ray fluorescence or Auger electron emission [44]. Both can infer absorption cross-sections within certain experimental conditions and approximations. Electron yield (EY) is influenced by external magnetic and electric fields with a penetrating depth of approximately $\sim$ 2 nm. Conversely, the measurement of fluorescence yield (FY) provides greater escape depths of the radiative photons; however, the resultant spectra can suffer from considerable state-dependent decay channels [131, 132], self-absorption [133] and saturation effects, significantly distorting the spectra of concentrated materials.

1.2.5 Multiplet Theory

The application of atomic multiplet theory and the continued implementation into the domain of charge-transfer ligand field theory has provided overwhelming success in the interpretation of core-level spectroscopy. This introduction will focus on interpreting $L_{2,3}$-edge XAS, XMCD [134, 135] and RIXS [136–138] calculations with

multiplet effects describing the atomic and perturbative contributions upon the ground and excited states of a given configuration.

Direct solution of a given Hamiltonian through the Dirac equation [139] provides a complete treatment of relativistic and many-body contributions of electronic states. However, computationally this approach is time-intensive at best, and impossible in many other cases, so instead, the solution applied through multiplet models is routinely deemed more appropriate.

Software

Quanty is a many-body scripting language developed by Haverkort and co-workers [140] to construct and solve multiplet calculations through a second-quantisation approach. The program is built within C/C++ with a Lua wrap, enabling the user control in the construction of Hamiltonians and transition operators to solve core-level spectroscopic problems. Quanty expands and modernises upon the previous multiplet code developed by Theo Thole, TTMULT, first developed in 1985 [141]. TTMULT was built upon the atomic theory developed by Cowan [59], and group theory approaches by Butler [142], which still have foundations within Quanty.

Quanty is built upon expanding spherical and radial harmonics with the construction of a Hamiltonian and evaluation of absorption cross-sections. A general discussion of the Hamiltonian's dependencies on the spectroscopic calculations will be provided below. Further detailed reading is available [104, 143–145].

1.2.6 Charge Transfer Ligand Field Multiplet Calculations

The construction of a Hamiltonian within a quantum mechanical formalism describing the multielectronic components of a charge-transfer ligand field multiplet approach is defined as:

$$\hat{\mathcal{H}} = \hat{\mathcal{H}}_T + \hat{\mathcal{H}}_V + \hat{\mathcal{H}}_{e^-e^-} + \hat{\mathcal{H}}_{SO} + \hat{\mathcal{H}}_{CF} + \hat{\mathcal{H}}_{Hyb.} \tag{1.6}$$

where the first term represents the kinetic energy of the electrons and the second electrostatic interaction with the nucleus; the third and fourth terms symbolise the electron-electron and spin-orbit coupling interactions; the local environment of the crystal field is taken into account through the fifth term Hamiltonian, and the last term

considers the orbital hybridisation. Application of the Born-Oppenheimer approximation to a reduced Hamiltonian description of the atom [146], assumes the wavefunctions of electrons can be treated separately from that of the nucleus, simplifying an atomic Hamiltonian equation to:

$$\hat{\mathcal{H}}_{atom} = \hat{\mathcal{H}}_{av} + \hat{\mathcal{H}}_{e^-e^-} + \hat{\mathcal{H}}_{SO} = \hat{\mathcal{H}}_{av} + \sum_{i>j}^{N} \frac{e^2}{r_{ij}} + \sum_{i=1}^{N} \xi(r_i)\, l_i \cdot s_i \tag{1.7}$$

where $\hat{\mathcal{H}}_{av} = \hat{\mathcal{H}}_T + \hat{\mathcal{H}}_V = -\sum_{i=1}^{N} \frac{p_i^2}{2m} + \sum_{i=1}^{N} \frac{-Ze^2}{r_i}$; which for a given electronic configuration is constant and does not require solving in the calculations of X-ray absorption spectroscopy. Thus simplifying equation 1.6 to $\hat{\mathcal{H}} = \hat{\mathcal{H}}_{e^-e^-} + \hat{\mathcal{H}}_{SO} + \hat{\mathcal{H}}_{CF} + \hat{\mathcal{H}}_{Hyb.}$ for application in the construction of a charge transfer ligand field multiplet calculation.

Electron-Electron Interactions

Multipole expansion of $\hat{\mathcal{H}}_{e^-e^-}$ and separation into spherical harmonics and radial components yields:

$$\hat{\mathcal{H}}_{e^-e^-} = \sum_{i>j}^{N} \frac{e^2}{r_{ij}} = \left\langle {}^{2S+1}L_J \middle| \frac{e^2}{r_{ij}} \middle| {}^{2S+1}L_J \right\rangle = \sum_k f_k F^k + \sum_k g_k G^k \tag{1.8}$$

Angular coefficients, f_k and g_k are calculated using Wigner $3j$- and $6j$-symbols. Solving for k of absorption ground-states, $3d^n$ results in f_k = 0,2,4 and excited-states, $2p^5d^{n+1}$ of f_k = 0,2,4 and g_k=1,3 [147]. F^k and G^k represent Slater-Condon-Shortley parameters which correspond to radial integrals of direct and exchange interactions respectively [148–151]. Most commonly theses values are utilised as reduced radial integrals (F_k, G_k) and Racah parameters (A,B and C) [152] through the respective set of equations [153, 154]:

$$F_0 = F^0 \qquad A = F_0 - 49F_4$$
$$F_2 = \frac{F^2}{49} \qquad B = F_2 - 5F_4$$
$$F_4 = \frac{F^4}{441} \qquad C = 35F_4$$

Racah parameters are frequently used as a measure of central field covalency (C/B) [155] in the assignment of optical transitions. Self-consistent Hartree-Fock calculations determine the atomic weighting and multiplet coupling of Slater-Condon-Shortley integrals. Hartree-Fock methods determine wavefunction approximations of single ions through *ab initio* calculations. It is established that the values obtained are consistently over-estimated integrals by $\sim$20%. Furthermore, under-estimations of bonding contributions require an additional parameterised reduction of the overestimation of Racah A and B as a first principles quantification of covalency [156].

Crystal Field

Upon the formation of the atomic Hamiltonian, the crystal field of the metal ion is added as a perturbation.

$$\hat{\mathcal{H}}_{CF} = V_{CF}(r_i, \theta_i, \varphi_i) = \sum_{k=0}^{\infty} \sum_{m=-k}^{m=k} A_{k,m} r^k C_m^k(\theta, \varphi) \tag{1.9}$$

The above equation represents the decomposition of the crystal field potential in normalised spherical harmonics $C_m^k(\theta, \varphi)$ and is restricted by the symmetry defining numerical constant A_m^k [59]. Solution of Equation 1.9 in a $D_{\infty h}$ symmetry results in d-orbtial splitting defined through the crystal field parameters, $D\mu$ and $D\nu$ [157]:

$$A_{2,0} = E_{a_{1g}} - 2E_{e_{2g}} + E_{e_{1g}} \qquad E_{a_{1g}} = -D\mu + 4D\nu$$
$$A_{4,0} = \frac{3}{10}\left(6E_{a_{1g}} + 2E_{e_{2g}} - 8E_{e_{1g}}\right) \qquad E_{e_{2g}} = 2D\mu - D\nu$$
$$E_{e_{1g}} = -2D\mu - 6D\nu$$

Orbital Hybridisation

Application of a nephelauxetic reduction infers an electronic density transfer to bonding molecular orbitals, and thus, a decrease of interelectronic repulsions [158]. This interpretation assumes an isotropic delocalisation of electronic orbitals, which frequently oversimplifies an accurate representation of metal-ligand bonding contributions, where covalency is strongly symmetry dependent. Valence bond configuration interactions, (VBCI) [159] introduces symmetry restricted electron transfer through both inter-shell and metal-ligand orbital hybridisation models. Application of these principles has facilitated the quantification of numerous complexes exhibiting $3d$-$4p$ hybridisation [160, 161], and metal-to-ligand [162], and [163]/or ligand-to-metal charge trans-

fer (MLCT and LMCT respectively) processes through core-level spectroscopic techniques, to uncover previously inaccessible bonding properties [107, 164–166]. Below documents the construction of a $3d$-$4s$ orbital hybridisation Hamiltonian, $\hat{\mathcal{H}}_{3d-4s}$.

$3d$-$4s$ orbital hybridisation is symmetry restricted through the $3d_{z^2}$ orbital; $A_{2,0}/\sqrt{5}$ as described in the basis of spherical harmonics. The ground-state wavefunction, ψ_{gs} is calculated through diagonalisation of the Hamiltonian matrix:

$$\begin{aligned}\hat{\mathcal{H}}_{3d-4s} &= \begin{bmatrix} 0 & V_{4s} \\ V_{4s} & \Delta_{4s} \end{bmatrix} \\ \psi_{gs} &= \alpha \left|3d^n\right\rangle + \beta \left|3d^{n-1}4s\right\rangle \\ \frac{\beta}{\alpha} &= \frac{\sqrt{\Delta_{4s}^2 + 4V_{4s}^2} - \Delta_{4s}}{2V_{4s}}\end{aligned}$$

where V_{4s} and Δ_{4s} represent orbital overlap and energy separation of the $3d^n$ and $3d^{n-1}4s$ configurations. Additional Slater-Condon-Shortley integrals are also introduced with $4s$ hybridisation; these include exchange G^2_{ds} and G^1_{ps}, G^2_{ds} of the initial and final states, respectively. 80% reduction applied to the calculated free-ion values deduced from RCN [141]. The introduction of $3d$-$4s$ orbital hybridisation had not been previously investigated through multiplet calculations of single crystal spectroscopic measurements within the literature. The implications upon the magnetism and electronic configurations of $Li_2(Li_{1-x}TM_x)N$ will be explored in the subsequent chapters.

Spectroscopic Cross-section Calculations

The calculation of X-ray absorption can be expressed through the dipole approximation of Fermi's golden rule, Eq. 1.10. While the two-step RIXS process can be calculated through the partial Kramers-Heisenberg equation [167, 168], Eq. 1.11.

$$\sigma_{abs}(\Omega) = 4\pi^2\hbar\alpha\Omega \sum_{i,f} \left|\langle\psi_f \left|O\right| \psi_i\rangle\right|^2 \delta\left(E_f - E_i - \hbar\Omega\right) \tag{1.10}$$

$$\sigma_{sct}\left(\Omega,\omega\right) = \frac{r_e^2}{m^2}\frac{\Omega}{\omega}\sum_f \left|\sum_n \frac{\left\langle\psi_f\left|O^\dagger\right|\psi_n\right\rangle\left\langle\psi_n\left|O\right|\psi_i\right\rangle}{E_i - E_n + \hbar\omega + i\Gamma_i/2}\right|^2 \delta\left(E_f + \hbar\Omega - E_i - \hbar\omega\right) \tag{1.11}$$

where $\hbar\Omega$ and $\hbar\omega$ represent the incident and emission energies of the incoming

and outgoing photons. $\alpha = e^2/\hbar c$ is the fine-structure constant, $r_e^2 = e^2/4\pi\epsilon_0 mc^2$ is the classical radius of the electron, and m the mass of an electron. ψ_i, ψ_n, ψ_f are the system's initial, intermediate and final state many-body wavefunctions with corresponding energies E and associated lifetime broadening, Γ. The limitation of these equations within modern theoretical calculations is the solution of the Dirac function δ, which ensures energy conservation and requires summation over all initial and final states. This computationally intensive task is replaced with a Green's function, which defines a transition propagator operator, O and makes full use of the spherical harmonic basis within Quanty [169].

$$F_i^{XAS}(\omega) = -\,\mathrm{Im}\left[\left\langle \psi_i \middle| O_a^\dagger \frac{1}{\hbar\omega - \hat{\mathcal{H}}_f + E_i + i\Gamma_i/2} O_a \middle| \psi_i \right\rangle\right] \tag{1.12}$$

$$F_i^{RIXS}(\Omega,\omega) = -\frac{1}{\pi}\mathrm{Im}\left[\left\langle \psi_i \middle| O_a^\dagger \frac{1}{\omega - i\Gamma_i/2 + E_i - \hat{\mathcal{H}}_m^\dagger} O_e^\dagger \right.\right.$$
$$\left.\left. \frac{1}{\Omega + i\Gamma_f/2 + E_f - \hat{\mathcal{H}}_f} O_e \frac{1}{\omega + i\Gamma_i/2 + E_i - \hat{\mathcal{H}}_m} O_a \middle| \psi_i \right\rangle\right]$$

where F_i is the intensity of the respective state $|\psi_i\rangle$, which is scaled through a Boltzmann temperature distribution of all states to determine total intensity:

$$I^{XAS}(\omega, T) = \frac{1}{Z} e^{-\frac{E_i}{k_B T}} F_i^{XAS}(\omega)$$
$$I^{RIXS}(\Omega, \omega, T) = \frac{1}{Z} e^{-\frac{E_i}{k_B T}} F_i^{RIXS}(\Omega, \omega)$$

where Z is the partition function and $\Gamma_i$and Γ_f represent the core-hole and final-state lifetime broadenings, respectively. The operators O_a and O_e define the interaction of an electromagnetic plane wave and electron within the system describing an absorption and emission process. Within the dipole approximation limit the transition operator is reduced to $O = \varepsilon \cdot \hat{r}$ where $\varepsilon = \{\varepsilon_x, \varepsilon_y, \varepsilon_z\}$ is the polarisation vector of light with respect to the absorbing electron $\hat{r}$. This can be expanded upon within re-normalised spherical harmonics, C_m^k:

$$\begin{aligned}\varepsilon \cdot \hat{r} = &(\varepsilon_x + i\varepsilon_y)\, C^1_{-1} \\ &+ \varepsilon_z\, C^1_0 \\ &+ (-\varepsilon_x + i\varepsilon_y)\, C^1_1\end{aligned}$$

Through expression of quantum mechanical questions within a second quantisation approach and solution of absorption and emission cross-sections within Greens theorem, the semi-empirical nature of the Quanty program has provided endless possibilities in unravelling the nature of a myriad of complexes. The direct control and construction of a representative Hamiltonian facilitates environmental dependencies such as polarisation, single-crystal angular dependencies and more to compare directly to experimental measurements. In the following chapters, Quanty is applied in conjunction with *ab initio* calculations to discern the unique electronic and magnetic properties of $Li_2(Li_{1-x}TM_x)N$ with a primary focus on the $Li_2(Li_{1-x}Fe_x)N$ analogue.

Chapter 2

Single-ion magnetism in the extended solid-state: insights from X-ray absorption and emission spectroscopy

Upon commencing this thesis, many unresolved questions existed regarding $Li_2(Li_{1-x}Fe_x)N$, primarily revolving around the quantification of valence and electronic structure. Resulting from the nature of the material as a dopant host lattice, this substantially limited quantification through laboratory techniques, thus turning to synchrotron-based experimental measurements as an element-specific, high brilliance probe. Diamond Light Source hosted the vast majority of the experimental measurements performed within this chapter, enabling experimental evidence of N-Fe-N bond length, ligand-field and geometric quantification, and electronic structure as a function of concentration, x. These inaugural measurements provide the foundation of understanding for $Li_2(Li_{1-x}Fe_x)N$ and analogue $Li_2(Li_{1-x}TM_x)N$ systems throughout this thesis.

Chemical Science

ROYAL SOCIETY OF CHEMISTRY

EDGE ARTICLE

View Article Online
View Journal | View Issue

Cite this: *Chem. Sci.*, 2020, **11**, 11801

All publication charges for this article have been paid for by the Royal Society of Chemistry

Single-ion magnetism in the extended solid-state: insights from X-ray absorption and emission spectroscopy†

Myron S. Huzan, [ab] Manuel Fix,[c] Matteo Aramini,[d] Peter Bencok,[d] J. Frederick W. Mosselmans, [d] Shusaku Hayama,[d] Franziska A. Breitner,[c] Leland B. Gee, [e] Charles J. Titus, [f] Marie-Anne Arrio,[g] Anton Jesche[c] and Michael L. Baker *[ab]

Large single-ion magnetic anisotropy is observed in lithium nitride doped with iron. The iron sites are two-coordinate, putting iron doped lithium nitride amongst a growing number of two coordinate transition metal single-ion magnets (SIMs). Uniquely, the relaxation times to magnetisation reversal are over two orders of magnitude longer in iron doped lithium nitride than other 3d-metal SIMs, and comparable with high-performance lanthanide-based SIMs. To understand the origin of these enhanced magnetic properties a detailed characterisation of electronic structure is presented. Access to dopant electronic structure calls for atomic specific techniques, hence a combination of detailed single-crystal X-ray absorption and emission spectroscopies are applied. Together K-edge, $L_{2,3}$-edge and Kβ X-ray spectroscopies probe local geometry and electronic structure, identifying iron doped lithium nitride to be a prototype, solid-state SIM, clean of stoichiometric vacancies where Fe lattice sites are geometrically equivalent. Extended X-ray absorption fine structure and angular dependent single-crystal X-ray absorption near edge spectroscopy measurements determine Fe^{I} dopant ions to be linearly coordinated, occupying a D_{6h} symmetry pocket. The dopant engages in strong 3dπ-bonding, resulting in an exceptionally short Fe–N bond length (1.873(7) Å) and rigorous linearity. It is proposed that this structure protects dopant sites from Renner–Teller vibronic coupling and pseudo Jahn–Teller distortions, enhancing magnetic properties with respect to molecular-based linear complexes. The Fe ligand field is quantified by $L_{2,3}$-edge XAS from which the energy reduction of $3d_{z^2}$ due to strong 4s mixing is deduced. Quantification of magnetic anisotropy barriers in low concentration dopant sites is inhibited by many established methods, including far-infrared and neutron scattering. We deduce variable temperature L_3-edge XAS can be applied to quantify the $J = 7/2$ magnetic anisotropy barrier, 34.80 meV (~280 cm^{-1}), that corresponds with Orbach relaxation *via* the first excited, $M_J = \pm 5/2$ doublet. The results demonstrate that dopant sites within solid-state host lattices could offer a viable alternative to rare-earth bulk magnets and high-performance SIMs, where the host matrix can be tailored to impose high symmetry and control lattice induced relaxation effects.

Received 10th July 2020
Accepted 2nd October 2020

DOI: 10.1039/d0sc03787g

rsc.li/chemical-science

1 Introduction

Linearly coordinated transition metal ions can exhibit first-order spin–orbit coupling which gives rise to large magnetic anisotropy barriers and bi-stability of magnetisation. An example of this is Fe doped in lithium nitride ($Li_2(Li_{1-x}Fe_x)N$). The magnetic anisotropy energy of $Li_2(Li_{1-x}Fe_x)N$ exhibits an observed coercivity field of more than 11 T, exceeding even the largest values observed in rare-earth-based permanent magnets.[1] Consequently, the underlying electronic structure of $Li_2(Li_{1-x}Fe_x)N$ is of relevance to the search for alternatives to rare-earth materials. Furthermore, since large single-crystals can be prepared,[2] and the concentration of Fe sites (x) can be controlled, $Li_2(Li_{1-x}Fe_x)N$ prepared at low doping

[a]*The University of Manchester at Harwell, Diamond Light Source, Harwell Campus, OX11 0DE, UK. E-mail: michael.baker@manchester.ac.uk*
[b]*Department of Chemistry, The University of Manchester, Manchester, M13 9PL, UK*
[c]*EP VI, Center for Electronic Correlations and Magnetism, Institute of Physics, University of Augsburg, D-86159 Augsburg, Germany*
[d]*Diamond Light Source, Harwell Science and Innovation Campus, Chilton, Didcot, OX11 0DE, UK*
[e]*Department of Chemistry, Stanford University, Stanford, CA 94305, USA*
[f]*Department of Physics, Stanford University, Stanford, CA 94305, USA*
[g]*Institut de Minéralogie, de Physique des Matériaux et de Cosmochimie, CNRS, Sorbonne Université, IRD, MNHN, UMR7590, 75252 Paris Cedex 05, France*
† Electronic supplementary information (ESI) available. See DOI: 10.1039/d0sc03787g

concentrations is proposed as single-ion like and therefore a solid-state equivalent[3] to molecular based single ion magnets (SIMs). SIMs are complexes which display slow magnetic relaxation, and magnetic remanence relevant to nano-scale information storage technologies. Notable recent examples of linearly coordinated transition metal SIMs include a $Co^{II}(C(SiMe_2ONaph)_3)_2$ (where naph is a naphthyl group) complex with a non-aufbau $(d_{x^2-y^2},d_{xy})^3(d_{xz},d_{yz})^3(d_{z^2})^1$ configuration and resultant $L = 3$ ground-state orbital angular momentum.[4] Another intriguing result are unusual 3d ligand fields. A $D_{\infty h}$ crystal field transforms the 3d-orbitals to a $A_1(3d_{z^2})$ singlet at highest energy, followed by a $E_{1g}(3d_{xz},3d_{yz})$ doublet at an intermediate energy and a $E_{2g}(3d_{xy},3d_{x^2-y^2})$ doublet at lowest energy. However, multi-reference calculations based on the crystal structures of linear complexes, $[M^I(N(SiMe_3)_2)_2]^-$ (where M = Cr, Mn, Fe, Co) all predict a d-orbital splitting with $3d_{z^2}$ at lowest energy.[5] Reasoning for this is due to strong $4s–3d_{z^2}$ mixing that weakens the anti-bonding character of the metal ion $3d_{z^2}$ orbital. Experimental evidence and the associated implications of $4s–3d_{z^2}$ mixing on magnetic properties have been investigated on $[Fe^I(C(SiMe_3)_3)_2]^-$.[6] Calculations, based on the crystal structure, propose a $a_{1g}^2e_{2g}^3e_{1g}^2$ ground state configuration with an almost unquenched $L = 2$ orbital angular momentum. These calculations are supported and found consistent with Mössbauer spectroscopy data[7] and high-resolution single-crystal crystallography provides the first experimental evidence of $3d_{z^2}^2$ electron occupation from electron density analysis.[8] However, despite the increasing number of reports of new linear transition metal SIMs[9] there have been very few experimental studies beyond the characterisation of orientation averaged magnetism. In this paper we demonstrate X-ray absorption spectroscopies as an accurate means to characterise the geometric and electronic structure of two coordinate transition metal SIMs.

We report results of extended X-ray absorption fine structure (EXAFS), X-ray absorption near edge spectroscopy (XANES), Kβ X-ray emission spectroscopy (XES) and $L_{2,3}$-edge X-ray absorption spectroscopy (XAS) single-crystal measurements on $Li_2(Li_{1-x}Fe_x)N$. Each of these techniques have specific sensitivities associated with transition selection rules and generated core-holes. A schematic overview of the spectroscopic techniques and associated transitions are shown in Fig. 1. K-edge XANES probes unoccupied 4p orbitals with 1s → 4p dipole transitions and unoccupied 3d orbitals *via* the much weaker intensity pre-edge, 1s → 3d, transitions. The technique has particular sensitivity to local coordination symmetry, making it ideally suited for probing distortions from a linear, $D_{\infty h}$, to a bent, C_{2v}, coordination. Bending leads to a pseudo Jahn–Teller effect that mixes $4p_{x,y}$ character into $3d_{xz,yz}$. This mixing can be clearly identified since it drives strong dipole intensity enhancement in the pre-edge. EXAFS quantifies interference effects due to electron scattering from the surrounding atoms. Kβ XES involves the ionisation of a 1s electron and the detection of photons emitted from occupied 3p and occupied valence-electrons filling the 1s core-hole. Inter-shell 3d–3p Coulomb exchange makes Kβ XES a sensitive probe of 3d spin-state in $Li_2(Li_{1-x}Fe_x)N$ as a function of concentration, x.[10] $L_{2,3}$-edge XAS probes 2p → 3d dipole transitions providing direct

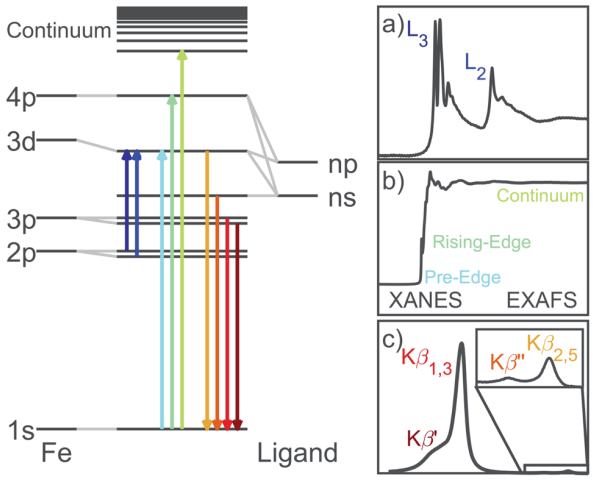

Fig. 1 Illustration of the Fe X-ray spectroscopic techniques with the associated transitions. (a) $L_{2,3}$-edge absorption probes unoccupied 3d orbitals. Spin–orbit coupling within the $2p^5$ core-hole splits the absorption into the $2p_{1/2}$ and $2p_{3/2}$ edges. (b) K-edge pre-edge, edge and EXAFS correspond to 1s absorptions into unoccupied 3d, 4p and continuum respectively. (c) Following the ejection of a 1s electron, Kβ XES involves the decay of Fe 3p and occupied valence electrons into the 1s core-hole.

experimental access to the ligand field, related $4s–3d_{z^2}$ mixing, spin–orbit coupling and the resultant anisotropy barrier.[11]

Magnetisation studies for low Fe doping concentrations show hysteresis is maintained up to 16 K with sweep rates of 15 mT s^{-1},[12] which is the largest temperature reported for a transition metal SIM. The effective energy barrier to magnetisation reversal is estimated between 37.1 and 40.2 meV (298.9 and 324.6 cm^{-1}).[12] Below a blocking temperature of ~10 K relaxation to magnetisation becomes temperature independent, with an exceptionally long magnetic relaxation time of $\tau > 10^4$ s.[13] However, despite several theoretical[1,14,15] and experimental[13,16–19,55] studies, the electronic structure of $Li_2(Li_{1-x}Fe_x)N$ remains a matter of considerable contention. Even the oxidation state of Fe sites has been brought into question by recent *ab initio* calculations proposing the presence of Li-ion vacancies coupled to Fe^{II} sites.[20] Fig. 2 shows the proposed structure of a single Fe dopant site present within $Li_2(Li_{1-x}Fe_x)N$ and possible ground state electronic configurations for both the

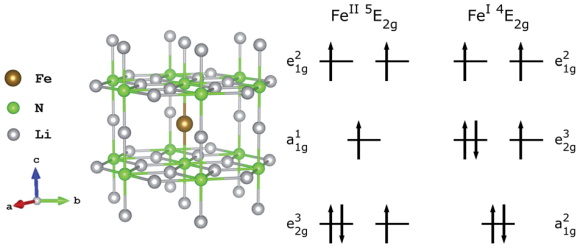

Fig. 2 (left) Structure of $Li_2(Li_{1-x}Fe_x)N$; Fe substitution within α-Li_3N matrix at the 1*b* Wyckoff position. (right) Proposed Fe^{II} and Fe^{I} electron occupations.[20]

divalent and mono-valent situations. Additional open questions arise due to the inaccessibility of low concentration Fe sites embedded within the host structure, and presence or absences of Fe dopant clustering effects and concentration dependencies. In this paper we apply the range of X-ray spectroscopies that selectively characterise different aspects of electronic structure, from which we identify $Li_2(Li_{1-x}Fe_x)N$ is a high symmetry solid state SIM clear of stoichiometric vacancies where Fe lattice sites are geometrically equivalent. The geometric and electronic structure of $Li_2(Li_{1-x}Fe_x)N$ is compared against molecular based SIMs and important insights into the origin of high temperature magnetic blocking and exceptionally long magnetic relaxation times observed in $Li_2(Li_{1-x}Fe_x)N$ are obtained.

2 Experimental section

2.1 Preparation of $Li_2(Li_{1-x}Fe_x)N$

Single crystal growth of $Li_2(Li_{1-x}Fe_x)N$ was achieved through a Li-rich solution to a desired concentration, x, and verified by inductively coupled plasma mass spectrometry (detailed information on crystal synthesis reported by Jesche and Canfield in ref. 2). $Li_2(Li_{1-x}Fe_x)N$ crystallises as a hexagonal lattice of Li_2N layers alternating with $Li_{1-x}Fe_x$ planes perpendicular to the crystallographic c axis. Dopant Fe site substitution replaces a Li-1*b* Wyckoff position ion, Fig. 2. Crystal growth stipulates the crystallographic c axis (magnetic easy-axis) to be oriented surface normal enabling accurate mounting of single crystals to easily perform angular dependence measurements.

2.2 K-edge XANES, EXAFS and Kβ XES measurements

XANES, EXAFS and Kβ XES measurements were performed using the high-resolution fluorescence-detection available at the I20-scanning beam-line at Diamond Light Source, UK, and exploiting a four-bounce Si(111) monochromator for spectral purity.[21] The XES measurements were collected by a medipix detector from three Si(531) analyser crystals. XANES and EXAFS measurements were detected with a 64 element Ge detector windowed to the Kα fluorescence line. XANES monochromatic energy ranges; 7000–7075 eV, 5 eV step size, 1 s integration (pre-edge), 7075–7100 eV, decreasing step size 5–0.5 eV, 1 s integration (rising-edge), 7100–7135.5 eV, 0.5 eV step size, 1 s integration (XANES), 7135.5–8100 eV, 0.04 Å, increasing integration time from 1–5 s (EXAFS). Kβ emission energy ranges; 7025–7080 eV, 0.3 eV step size, 1s int. time (Kβ mainline), 7080–7120 eV, 0.2 step size, 5 s integration time (valence-to-core). Several spectra were acquired for each doping concentration. Kβ measurements were performed with the incident energy set above the Fe K-edge at 8500 eV. The XANES, EXAFS and Kβ measurements were performed at room temperature. Additional Kβ measurements at 80 K exhibited negligible difference with respect to measurements at room temperatures. To minimise diffraction induced distortions within EXAFS spectra, crystals of $Li_2(Li_{1-x}Fe_x)N$ were ground into powdered pellets where possible. However, it is reported that the host crystal Li_3N exhibits an additional high pressure phase, of which grinding can induce a partial phase transformation of the Li_3N lattice from the α to β phase.[22] The XANES spectra of α and β $Li_2(Li_{1-x}Fe_x)N$ differ significantly. Therefore XANES measurements were performed on both single-crystal and powder samples, from which it was deduced that only the lowest concentration $Li_2(Li_{1-x}Fe_x)N$ sample was affected by grinding. For this reason the measurements performed on $Li_2(Li_{1-x}Fe_x)N$ for $x = 0.0020(5)$ were on a single crystal while for $x = 0.0063(4)$ and $0.0093(6)$ were undertaken on powder samples. Powder samples were formed into pellets and mixed with boron nitride to an appropriate dilution to minimise self-absorption effects. Samples of $Li_2(Li_{1-x}Fe_x)N$ were prepared within an argon atmosphere glove-box (<0.5 ppm O_2 and H_2O) where single crystals and powders were encapsulated with Kapton tape. Measurements were performed within a nitrogen gas atmosphere. XANES and EXAFS analysis was undertaken within the Athena and Artemis packages.[23] Background subtraction was undertaken with a linear fitting of the pre-edge and normalisation through a third order polynomial of the post-edge. Bond length (R) and Debye–Waller factor (σ) were used as variables of fitting for neighbouring lithium and nitrogen atoms. A Levenberg–Marquardt non-linear least-squares minimisation was applied for EXAFS fitting. Kβ XES spectra are normalised through a trapezoidal integration and the subtraction of a constant. Angular dependent XANES measurements were performed at the BL9-3 beamline at SSRL. The measurements were performed at 10 K in transmission mode on a 1 mm thick single crystal. These measurements were performed with monochromatic energy ranges; 6785–7085 6 eV step size, 1 s integration (pre-edge), 7085–7150 eV, 0.15 eV step size, 1 s integration (rising-edge), 7150–8359.5 eV, 0.5 eV step size, 1 s (post-edge region). Background subtraction of main K-edge XANES isolates the rising-edge peak from which Pearson VII peak fitting was undertaken through a least-squares minimisation, Fig. S3.†

2.3 $L_{2,3}$-edge XAS measurements

$L_{2,3}$-edge XAS measurements were performed at the I10 high field magnet end station at Diamond Light Source. Fast energy XAS scans were performed between 690–755 eV with 0.1 eV step sizes. The measurements were performed between 4.5–400 K within an ultra-high vacuum (10^{-10} bar). Detection was performed *via* total fluorescence yield in a back-scattering geometry using a 10×10 mm^2 silicon diode with a 150 nm Al cover to filter out electrons. Single crystals of $Li_2(Li_{1-x}Fe_x)N$ are too insulating to obtain drain current detected XAS. Single crystals were mounted within an argon glovebox with Torr Seal epoxy resin and transferred to experimental chamber through a nitrogen purged glovebag. Background subtraction of the spectra was performed with a linear fitting of the pre-edge (690–700 eV) and normalisation through a linear fitting of the post edge (735–750 eV). The $2p_{3/2}$ and $2p_{1/2}$ continuum transitions were subtracted through a double arctangent function[24] (further details see ESI Fig. S4†).

Ligand field multiplet simulations of the $L_{2,3}$-edge XAS results were performed using the quantum many-body scripting

language, Quanty.[25] The Quanty input files for the simulation of $L_{2,3}$-edge fluorescence XAS were adapted from templates generated in Crispy.[26] Multiplet effects are described by the Slater–Condon–Shortley parameters, F^{k}_{pp}, F^{k}_{pd} (Coulomb) and G^{k}_{pd} (exchange), reduced to 80% of the Hartree–Fock calculated values to account for the over-estimation of electron–electron repulsion found for the free ion. The $2p^5$ spin–orbit coupling parameter ξ_{2p} is found consistent with the atomic value (8.202 eV). The 3d spin–orbit coupling parameters were obtained by fitting to the temperature dependence of the $L_{2,3}$-edge XAS, giving $\xi_{3d} = 0.052$ and 0.068 eV for the initial and final states respectively. The presence of 4s mixing in linear transition metal complexes is known to weaken the 3dσ anti-bonding character and reducing the energy of the $3d_{z^2}$ orbital. This effect is accounted for in a simple 3d ligand field model, where the relative energy of the orbitals are adjusted with parameters D_q, D_t and D_s, in the D_{6h} point group. The ligand field parameters describe the d-orbital degeneracy and energy splittings of the $A_{1g}(3d_{z^2})$ singlet, and two E doublets, $E_{1g}(d_{xy},d_{yz})$ and $E_{2g}(d_{x^2-y^2},d_{xy})$. A local linear coordination geometry is characterised by a $D_{\infty h}$ ligand-field, and has equivalence with D_{6h} when $D_q = 0$. Broadening of the transitions as described by the core-hole lifetime was applied through a Lorentzian function over the L_3 and L_2 edge of 0.35 eV and 0.7 eV full width half maximum (FWHM) respectively. Gaussian broadening due to the instrumental resolution was set to 0.25 eV FWHM and simulated at 4.5 K.

2.4 Calculation details

The density functional theory (DFT) calculations presented in this work were performed using the plane-wave pseudopotential DFT method available within the codes Quantum-Espresso[27] and CASTEP.[28] Generalised-gradient approximation for the exchange-correlation energy was selected in the form of PBE functional.[29] Ultrasoft pseudopotentials were used for PBE and PBE+U calculations, whereas relativistic ultrasoft pseudopotentials were used for the non-collinear calculations including spin–orbit coupling. The pseudopotentials for use with Quantum-Espresso were taken from the PSlibrary[30] while the pseudopotentials for use with CASTEP were generated self consistently. A kinetic energy cutoff of 90 Ry for the wave function and of 900 Ry for the charge density together with a (6 × 6 × 6) Monkhorst–Pack *k*-point grid were determined as parameters for convergence calculations. A (10 × 10 × 10) *k*-point grid was instead used for the calculation of the density of states (DOS). Self-consistent calculations were performed to a convergence value of 1×10^{-7} eV. Due to the isolated nature of Fe atoms in $Li_2(Li_{1-x}Fe_x)N$, we operated with a 3 × 3 × 3 supercell constructed from the hexagonal cell of Li_3N having space group *P*6/*mmm*. The structure was relaxed so that the Fe–N and Fe–Li distances in the first coordination shells of iron matched the distances evaluated from the analysis of EXAFS results. The reliability of the experimentally evaluated structure for simulations was tested by completing a relaxation up to an energy change of 3×10^{-6} eV per atom, which produced a structure yielding a shorter Fe–N distance but a comparable density of states. A smearing of 0.01 Ry was applied to the computed eigenvalues in order to improve the *k*-point convergence. The angular dependence of Fe K-edge was calculated including the effects of core-hole[31] and using the same *k*-point grid as previously used for the DOS. Ground state DFT was then expanded by expressing the exchange-correlation potential in terms of local-density band theory *via* the PBE+U method.[32] The electronic properties were calculated with the simplified, rotational-invariant formulation developed within the linear response approach.[33] An effective *U* value of 4 eV was included in such calculations, as previously estimated for similar compounds.[34] Angular-momentum dependent orbital occupation was determined with Löwdin charge analysis on top of ground-state, converged DFT wavefunctions. X-ray absorption spectra were computed by extracting the matrix elements for electronic interband transitions from the ground state DFT including the local effects of 1s core-hole as implemented in the code CASTEP. Such calculations were accomplished in the aforementioned supercell, in order to avoid interactions between periodic images of the core excitation. An energy shift of 7110.5 eV was applied to match the experimental data and normalised through trapezoidal integration of simulated spectrum. Transition broadening as a consequence of instrumental resolution (Gaussian) and core-lifetime effects (Lorentzian) was set as 0.2 and 1.25 eV FWHM respectively.

3 Results and discussion

3.1 Extended X-ray absorption fine structure (EXAFS)

To precisely quantify the local coordination environment at Fe sites EXAFS measurements were performed on samples with low dopant concentrations, where $x = 0.0020(5)$, 0.0053(4) and 0.0093(6). The k^3 weighted spectra are presented in Fig. 3a which highlight the EXAFS Fourier transform region as $3 \leq k \leq 10$ Å^{-1} for $x = 0.0020(5)$ and $3 \leq k \leq 12$ Å^{-1} for $x = 0.0053(4)$ and 0.0093(6) (E_0 = 7113 eV). Single crystal measurements were performed with *E* 45° relative to the crystallographic *c* axis on the lowest concentration ($x = 0.0020(5)$) sample resulting in significant Bragg peaks for *k* values greater than 10 Å^{-1}, requiring a reduced Fourier transform range.

EXAFS fitting was undertaken using a model including a single Fe atom dopant within α-Li_3N as an initial structure ($a = 3.652(8)$ Å and $c = 3.870(10)$ Å, Fig. 2). The selected scattering paths were limited up to a radial distance of 3.5 Å; these included two single scattering pathways (Fe–N–Fe, Fe–Li–Fe) and one double scattering path (Fe–N–Li–Fe). Fitting of the experimental data was undertaken for each concentration individually. The EXAFS fit parameter results are presented in Table 1. The coordinated nitrogen atoms characterise the first spectral peak centred at 1.5 Å, Fig. 3b, while scattering from the hexagonally bonded lithium atoms in combination with the double scattering path characterise the remaining spectral features. The Fe–N bond lengths were determined to be 1.873(7) Å, 0.062(7) Å shorter than the equivalent Li–N bond length. This finding is consistent with X-ray diffraction results that show *c*-axis contraction and *a* and *b*-axis expansion on increasing Fe concentration.[12,16,35] The length of the Fe–N bond is very short in

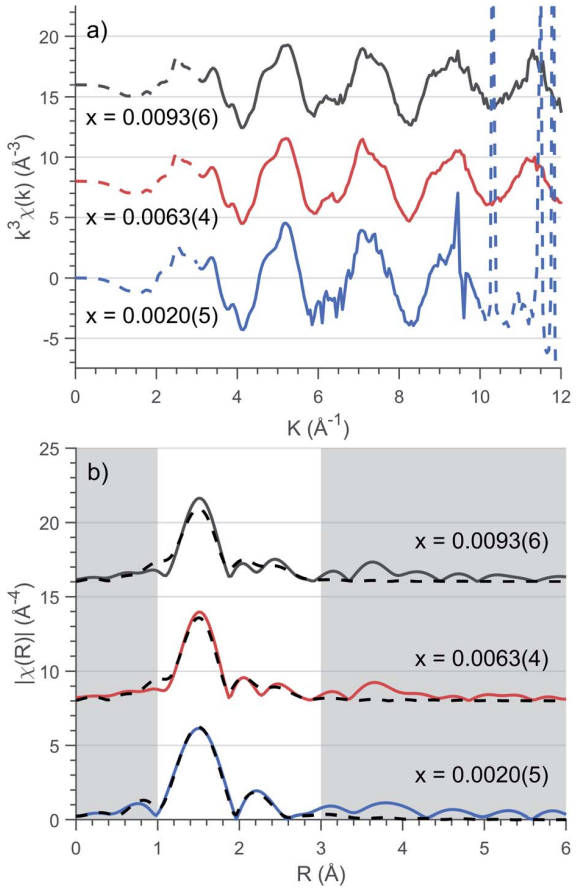

Fig. 3 (a) Background subtracted k^3 weighted XAFS spectra of various concentrations, x. Solid lines represent the Fourier transform region for EXAFS fitting. (b) Fitting of Fourier transformed k^3-weighted EXAFS spectra for $Li_2(Li_{1-x}Fe_x)N$ as a function of concentration, x. EXAFS fitting is represented as dashed lines with corresponding parameters presented in Table 1.

comparison with values reported for two coordinate Fe^{I}–N, including the linear complex [K(18-crown-6][Fe(N(SiMe$_3$)$_2$)$_2$] (1.9213(6) Å)[36] and the slightly bent [Fe(N(SiMe$_3$)Dipp)$_2$]$^-$ (1.91 Å).[37] The Fe–N length found for $Li_2(Li_{1-x}Fe_x)N$ compares more favourably with the linear divalent complex [Fe(N(SiMe$_3$)Dipp)$_2$] with a reported Fe^{II}–N length of 1.853(1) Å.[38] Many-body quantum chemistry calculations performed on Fe doped lithium nitride units $[Fe^{I}N_2Li_{14}]^{9+}$ and $[Fe^{II}N_2Li_{13}]^{9+}$ report bond lengths of 1.92 Å and 1.88 Å respectively.[20] In summary, comparison with reported Fe–N bond lengths for two coordinate complexes might suggest a divalent oxidation state for $Li_2(Li_{1-x}Fe_x)N$. Indeed this was the conclusion reported by Muller-Bouvet *et al.* (ref. 39) for Co doped lithium nitride, where EXAFS analysis included the pairing of dopants with Li vacancies at 2*c* sites, from which a formula of $Li_{3-2x}Co_xN$ with a divalent Co oxidation state is proposed.[39]

The EXAFS measurements are consistent with isolated Fe dopants with no indication of clustering evidenced through the lack of strong features beyond the first structural peak at 1.5 Å. While not conclusive there is an observed increase in *R*-factor with concentration which could be attributed to the requirement of incorporating small contributions from Fe–Fe and Fe–N–Fe scattering paths within the *ab* plane and along the *c* axis respectively.

According to combinatorial analysis, the probability of locating n Li ions at the 8 possible neighbouring sites (6 perpendicular and 2 parallel to the crystallographic *c* axis) for a dopant Fe ion is expressed as: $W_n = 8![n!(8-n)!]^{-1}(1-x)^n x^{8-n}$.[40] At the highest doped concentration, $x = 0.0093(6)$, the probability of all 8 neighbouring atoms being lithium is 92.8%, at which point there begins to be a non-negligible requirement of additional scattering pathways to account for Fe dimerisation. However, the number of available independent parameters, dictated by the Nyquist theorem $\left(N_{idp} = \frac{2\Delta k \Delta R}{\pi} + 1\right)$[41] prohibits the inclusion of multiple Fe ions within the model.

Table 1 EXAFS fitting parameters of various Fe doping concentrations, x of $Li_2(Li_{1-x}Fe_x)N$; *R*-factor (*R*), Energy alignment (ΔE), Fe–N and Fe–Li Bond Lengths (R_N and R_{Li} respectively) and Debye–Waller factor (σ^2) for lithium (Li) and nitrogen (N) scattering atoms. Amplitude reduction factor, S_0^2 fixed to 0.92

x	0.0020(5)	0.0063(4)	0.0093(6)
R	0.004	0.028	0.061
ΔE (eV)	10.85 ± 0.93	9.35 ± 1.84	9.73 ± 2.85
R_N (Å)	1.873 ± 0.007	1.869 ± 0.015	1.868 ± 0.023
σ_N^2 (Å^2) × 10^{-3}	0.7 ± 0.5	3.4 ± 1.0	4.9 ± 1.6
R_{Li} (Å)	2.867 ± 0.015	2.840 ± 0.025	2.845 ± 0.039
σ_{Li}^2 (Å^2) × 10^{-3}	20.4 ± 3.0	19.6 ± 4.5	17.9 ± 5.8

3.2 X-ray absorption near-edge structure (XANES)

Transition metal oxidation state is frequently characterised by the K-edge threshold energy and the characteristic multiplet effects present within the K pre-edge.[42] Fe K-edge XANES measurements on a polycrystalline sample of $Li_2(Li_{1-x}Fe_x)N$ was previously investigated by Niewa *et al.*[17,43] The threshold energy region of the XANES was found to be dominated by an intense transition centred at 7113 eV. The origin of the 7113 eV peak was assigned by Niewa *et al.*[17,43] as a K pre-edge (1s → 3d) transition, with enhanced intensity due to 4p-mixing, from which a local C_{2v} coordination symmetry was proposed. Since bending away from 180° introduces mixing of $4p_x$ character into $3d_{xz}$ and $4p_y$ into $3d_{yz}$ due to transformations under the same irreducible representations in C_{2v}. To further investigate Fe site coordination symmetry, we preformed angular dependent single-crystal Fe K-edge XANES measurements of $Li_2(Li_{0.985}Fe_{0.015})N$, Fig. 4 and S2.† The area of the 7113 eV peak for each sample orientation gives the angular dependence of the transition oscillator strength, Fig. 4. Measurements were experimentally limited from 0–45°, where 0° corresponds with $E \perp c$ and 90° with $E \| c$. Maximum intensity of the transition is observed at 0°. The variation in intensity as a function of crystal orientation follows a sinusoidal profile with a minimum at 90°; this is indicative of the two fold symmetry of dipole transitions with $4p_{x,y}$ orbital character. The XANES of linear Cu^{I} complexes

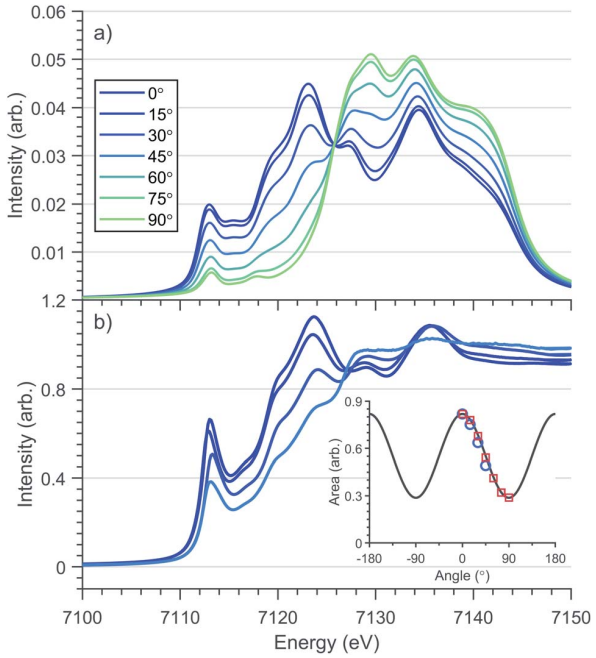

Fig. 4 Single crystal angular dependent Fe K-edge XANES of $Li_2(Li_{1-x}Fe_x)N$ (a) DFT calculations (b) experimental spectra with a nominal concentration of $x = 0.015$. 0° corresponds with $E \perp c$ and 90° with $E \| c$. (Inlay) Angular dependence of $1s-4p_{x,y}$ transition intensity of experimental (◯) and theoretical (□) rising-edge peak centred at 7113 eV.

are known to exhibit very low energy rising edge features due to transitions directly into degenerate $4p_{x,y}$ states,[44] however the XANES of open-shell linear transition metal complexes are less developed. The 7113 eV feature in $Li_2(Li_{0.985}Fe_{0.015})N$ is consistent with the crystal field model originally proposed for Cu^I, whereby the linear coordination lifts the $4p_{x,y,z}$ degeneracy, decreasing the energy of the degenerate $4p_{x,y}$ orbitals that are non-bonding and increasing the $4p_z$ orbital to a higher energy. To obtain conclusion of the origin of the 7113 eV peak, and the associated local symmetry of the Fe site, DFT calculations based on a linear geometry were found to accurately reproduce the angular dependent XANES of $Li_2(Li_{0.985}Fe_{0.015})N$, Fig. 4. Projection of the density of states from this resultant DFT simulation verifies the interpreted splitting and degeneracy of the Fe-4p orbitals. Unoccupied character above the Fermi energy (Fig. S5†) coincides with the expected degeneracy of the $4p_{x,y}$ orbitals at the energy of the rising edge feature with $4p_z$ orbital character shifted to higher energy. In summary, our angular dependent K-edge XANES analysis on $Li_2(Li_{0.985}Fe_{0.015})N$ identifies the local coordination symmetry involves a linear N–Fe–N motif; a conclusion that is further supported by our $L_{2,3}$-edge analysis in the following section. The weak quadrupole allowed $1s \rightarrow 3d$ K pre-edge transitions are however unresolved due to overlap with the considerably more intense 7113 eV feature. The absence of a resolvable pre-edge inhibits a ligand field multiplet analysis to quantitatively assign Fe spin ground-state by K-edge XANES.

3.3 Kβ X-ray emission spectroscopy

Magnetisation measurements for $Li_2(Li_{1-x}Fe_x)N$ shows considerable dependence on x.[1] In a recent theoretical study, many-body quantum chemistry calculations on $[Fe^IN_2Li_{14}]^{9+}$ and $[Fe^{II}N_2Li_{13}]^{9+}$ fragments show a strong reduction in magnetic anisotropy in going from a Fe^I to Fe^{II} dopant site.[20] Previous studies have proposed that dopant sites couple to a finite number of Li ion vacancies giving rise to minority divalent species and a monovalent majority species with a ratio that changes as a function of dopant concentration.[20,39] To address this question and investigate the spin-ground state of $Li_2(Li_{1-x}Fe_x)N$, Kβ XES measurements were performed as a function of doping concentration, x, Fig. 5. Since Kβ utilises a non-resonant incident photon energy it is less affected by self-absorption than resonant techniques, making it ideally suited to studying the Fe concentration dependence of electronic structure. The Kβ mainline, $Kβ_{1,3}$ and Kβ′, involves a dipole-allowed 3p–1s emission transition. These two mainline features have the advantage of being highly sensitive to spin ground-state, identified *via* differences in the $Kβ_{1,3}$ and Kβ′ splitting and intensity.[10] Fig. 5 shows Kβ measurements for $Li_2(Li_{1-x}Fe_x)N$ where $x = 0.1800(1)$, $0.0063(4)$ and $0.0020(5)$. There exists no electronic structural change as a function of doping concentration for $Li_2(Li_{1-x}Fe_x)N$; confirming no valence change with respect to concentration. Frequently Kβ is applied to fingerprint the spin ground-state and to deduce the valence of transition metal ions. However, due to a lack of two coordinate Fe^I reference spectra, such qualitative analysis is inhibited. Despite this, Fig. S1† compares the $Li_2(Li_{1-x}Fe_x)N$ Kβ-mainline spectrum with a series of six coordinate O_h and D_{4h} Fe^{II} and Fe^{III} model complexes.[45] The energy and intensity of the Kβ″ first moment is consistent with either a d^6 or d^7 occupation of the Fe from which either $S = 2$ or 3/2 could be inferred. However, there is a significant deviation in the splitting and intensity between the $Kβ_{1,3}$ and Kβ′ of $Li_2(Li_{1-x}Fe_x)N$ with respect to the model complexes.

The valence to core $Kβ_{2,5}$ and Kβ″ peaks have significant sensitivity to the local bonding environment around Fe site. The

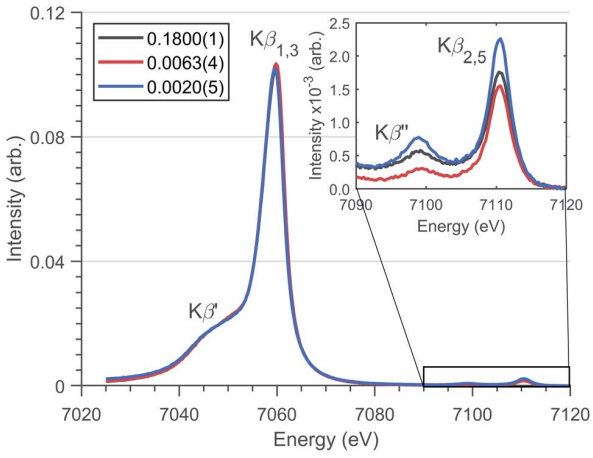

Fig. 5 Fe Kβ XES spectrum of $Li_2(Li_{1-x}Fe_x)N$ for several concentrations (x values defined in legend) with spectral features highlighted. (Inlay) Magnified valence-to-core region.

valence-to-core peaks at 7098.9 eV and 7110.6 eV (Fig. 5) correspond with metal character present within nitrogen 2s and 2p orbitals respectively. The lack of variation in the relative intensities and energies of these features is consistent with no variation in geometry around the N–Fe–N motif as a function of dopant concentration.

3.4 $L_{2,3}$-edge X-ray absorption spectroscopy

$L_{2,3}$-edge XAS accesses the electronic structure at the 3d orbitals through dipole allowed 2p–3d transitions. Single crystal measurements were performed with $E \perp$ to the crystallographic c axis and nominal doping concentration, $x = 0.015$. Fig. 6a shows the Fe $L_{2,3}$-edge total-fluorescence spectrum measured at 4.5 K, with L_3 and L_2 edge peaks at 705.7 eV and 720.3 eV respectively. The L_3-edge exhibits two intense features separated by 1.3 eV whereas the L_2-edge is dominated by a single intense peak. Both $L_{2,3}$-edges exhibit a series of high energy satellite features indicating the presence of significant metal–ligand charge transfer.

$L_{2,3}$-edge XAS ligand field multiplet fitting was performed to quantify the 3d electronic structure of dopant sites. Two sets of simulations were performed based on both Fe^{I} and Fe^{II} scenarios. Initial fit parameters were extracted from the results of *ab initio* results reported by Xu *et al.*,[20] see Table S1 and Fig. S6.† Optimisation of the simulated spectral features relative to experiment were obtained through adjustment of the ligand field parameters (D_t and D_s) and include the effect of 4s mixing through the reduction in energy of the $3d_{z^2}$ orbital. Agreement with the measured spectrum could only be obtained for the Fe^{I} valence model, with best fit parameters of $D_q = 0$, $D_t = 0.1806$ and $D_s = -0.0257$ eV corresponding to an electronic configuration such that d_{z^2} has the lowest orbital energy, Fig. 6. The simulation quantifies the $Li_2(Li_{0.985}Fe_{0.015})N$ dopant site as a Fe^{I} $3d^7$, $^4D_{7/2}$ ion, with a ^5E symmetry ground state resulting from a $e_{1g}{}^2e_{2g}{}^3a_{1g}{}^2$ configuration. The experimentally determined ligand field splitting is larger than the reported CASSCF result for a $[Fe^{I}N_2Li_{14}]^{9+}$ fragment that gave energies of 0, 0.91, 1.5 eV for $a_{1g}{}^2$, $e_{2g}{}^3$ and $e_{1g}{}^2$ respectively.[20] The energy reduction in d_{z^2} is approximately twice the value calculated for the linear monovalent SIM, $[Fe(C(SiMe_3)_3)_2]^-$.[6] Spin–orbit coupling splits the total angular momentum of Fe sites into four Kramers doublets. In order of increasing energy these doublets, $M_J = \pm 7/2$, $\pm 5/2$, $\pm 3/2$ and $\pm 1/2$, are evenly separated by approximately $2/3\xi$. This splitting characterises the magnetic anisotropy barrier to the slow magnetic relaxation observed in $Li_2(Li_{0.985}Fe_{0.015})N$, Fig. 6b. At sufficiently low temperature only the $M_J = \pm 7/2$ Kramers doublet is populated. The 4.5 K $L_{2,3}$-edge transitions hence emanate exclusively from the $M_J = \pm 7/2$ doublet. To evaluate the magnetic anisotropy barrier precisely, temperature dependent $L_{2,3}$-XAS measurements were performed. We find the strong selection rules of $L_{2,3}$-edge XAS makes the technique particularly sensitive to the population of M_J states. Therefore, *via* a series of measurements from 4.5 to 400 K the thermal population of M_J excited states can be experimentally deduced from changes in the line shape of the L_3-edge spectrum. The temperature dependence is most clearly identified through the relative peak intensity for Peak 1 (P_1), $E = 706.1$ eV *versus* Peak 2 (P_2), $E = 707.3$ eV at the L_3-edge, Fig. 7. Modelling the temperature dependent ratio of P_1 and P_2 through Maxwell–Boltzmann statistics the thermal population of the excited states can be achieved through the equation:

$$\frac{P_1}{P_2} = A\frac{\exp\left(-\frac{E_{7/2}}{k_B T}\right)}{\sum_{i=M_J}\exp\left(-\frac{E_i}{k_B T}\right)} + c \quad (1)$$

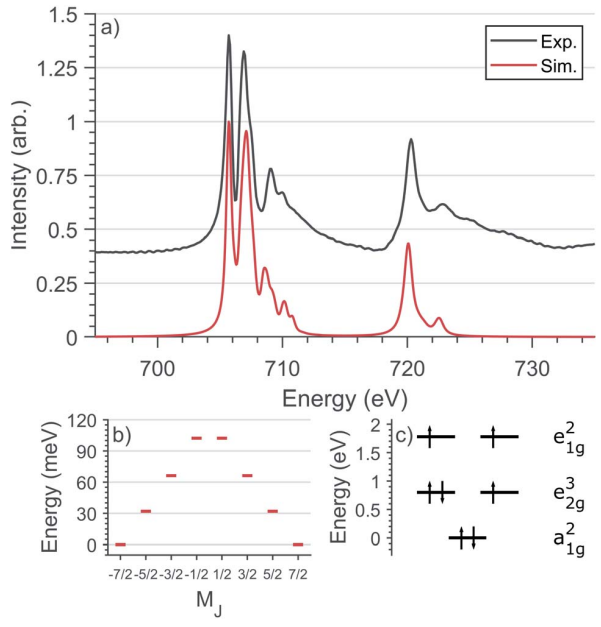

Fig. 6 (a) Comparison of experimental and simulated Fe $L_{2,3}$-edge spectra at 4.5 K with L_3 peak normalisation. (b) The calculated M_J splitting of the ground-state $J = 7/2$ manifold. (c) The calculated energies of 3d orbitals obtained from the $L_{2,3}$-edge ligand field multiplet fit.

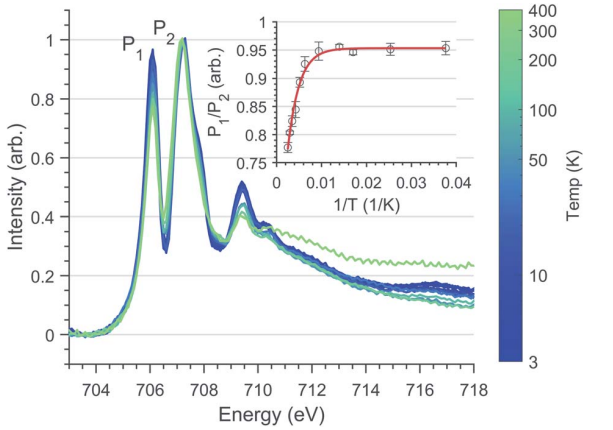

Fig. 7 Fe L_3 temperature dependence spectra of $Li_2(Li_{0.98}Fe_{0.02})N$ normalised through P_2 intensity. (Inlay) Least-squares fit of Eqn.(1) to L_3 peak ratio with respect to the inverse absolute temperature. Error bars represent standard deviation of repeat measurements.

where E_i represents the energy of the four M_J ±7/2, ±5/2, ±3/2 and ±1/2 states (each evenly separated by $2/3\xi$), k_B is the Boltzmann constant and A and c are multiplicative and scaling factors. The inlay of Fig. 7 shows L_3-edge peak ratio (P_1/P_2) *versus* inverse absolute temperature ($1/T$) for $Li_2(Li_{1-x}Fe_x)N$. Fitting to eqn (1) gives $\xi = 52.2 \pm 4.97$ meV (421 ± 40.08 cm^{-1}), significantly greater than the atomic value for Fe^I of 44.8 meV.[6] Typically, the free ion spin–orbit coupling parameter represents the upper limit for spin–orbit coupling, where bonding leads to only decrease ξ. However, atomic spin–orbit coupling is strongly dependent on electron configuration, particularly on the number of 3d electrons.[46] For instance, the 3d atomic spin–orbit coupling for a $3d^64s^1$ configuration is $\xi_{3d} = 51$ meV, approximately 6 meV greater than the value for a $3d^7$ configuration.[47] Therefore, we propose that the measured value of ξ is greater than the $3d^7$ atomic value due to strong $4s$–$3d_{z^2}$ mixing. Previously reported measurements of magnetic relaxation for $Li_2(Li_{1-x}Fe_x)N$ at low doping concentrations gave the effective energy barrier to magnetisation reversal (U_{eff}) between 37.1 and 40.2 meV (298.9 and 324.6 cm^{-1}).[12,19] This is close to 34.80 ± 3.31 meV (280.7 cm^{-1}) the energy splitting between the ground $M_J = \pm 7/2$ and first excited ±5/2 doublet determined from our variable temperature $L_{2,3}$-edge XAS analysis. To our knowledge the application of variable temperature L_3-edge XAS has not been previously reported. Therefore, we performed supporting calculations into the origin of this effect. This enabled us to confirm the same temperature dependence in the simulated spectra and test the validity of our fitting method (Fig. S7†). Furthermore, to identify the origin of the temperature dependence Fig. S8† shows the calculated $L_{2,3}$-edge XAS spectra associated with each thermally populated Kramer's doublet of the ground-state $J = 7/2$ manifold. The calculations identify the individual intensity contributions to P_1 and P_2 for each M_J doublet.

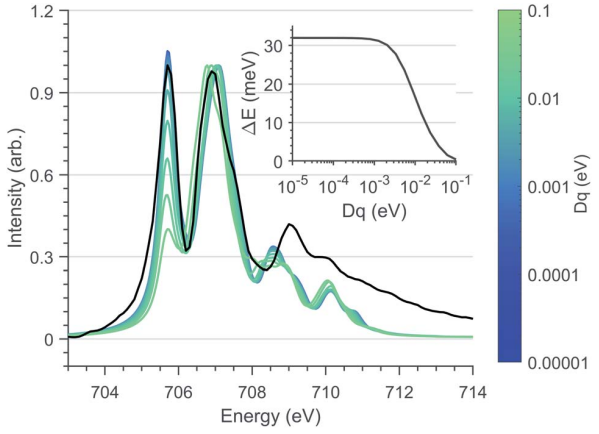

Fig. 8 Ligand field multiplet calculations of the Fe L_3-edge as a function of D_q splitting, normalised through second peak intensity. The D_t and D_s crystal field and spin–orbit coupling parameters are fixed to the optimised vales used in Fig. 6a. (Black) Experimental spectrum of $Li_2(Li_{0.985}Fe_{0.015})N$. (Inlay) Energy separation, ΔE of M_J ±7/2 and ±5/2 states with respect to D_q.

Since first-order spin–orbit coupling in $Li_2(Li_{1-x}Fe_x)N$ is a manifestation of an odd electron count within the E_{2g} orbitals, the relationship between non-linearity due to N–Fe–N bending and the magnetic anisotropy barrier can be explored through the introduction of a D_q crystal field parameter. Fig. 8 shows the effect of including a non-zero D_q energy on the simulated Fe L_3-edge. To maintain the measured anisotropy energy of $Li_2(Li_{0.985}Fe_{0.015})N$, the magnitude of D_q must be less than 1 meV. This result supports our angular dependent K-edge XANES analysis, demonstrating the strict N–Fe–N linearity imposed within the α-Li_3N matrix.

4 Conclusion and outlook

We have characterised the local geometric and electronic structure of Fe dopant sites in $Li_2(Li_{1-x}Fe_x)N$ *via* K-edge XANES and EXAFS, $L_{2,3}$-edge XAS and Kβ XES as a function of x, with particular attention to low values of x, where Fe sites are sufficiently isolated and hence perform as single ion magnets. The complementary use of element specific X-ray spectroscopy techniques unambiguously answers a multitude of questions that had limited quantitative understanding of this system. Kβ XES analysis rules out previous arguments[20] for a divalent subspecies in $Li_2(Li_{1-x}Fe_x)N$ at low x concentration. EXAFS analysis shows no evidence of preferential Fe clustering at low dopant concentrations. $L_{2,3}$-edge XAS measurements in conjunction with ligand field multiplet simulations conclude Fe sites are monovalent with a $^4D_{7/2}$ ground state of ^4E symmetry resultant from a $a_{1g}^2e_{2g}^3e_{1g}^2$ configuration. The energetic order of the 3d orbitals is affected by strong $4s$–$3d_{z^2}$ mixing that results in a fully occupied $3d_{z^2}$ at lowest energy. The strong influence of $4s$–$3d_{z^2}$ mixing in reducing the destabilisation of 3dσ antibonding has long been reasoned by DFT and more recently by quantum chemistry calculations.[6,48] It is shown that $L_{2,3}$-edge XAS enables experimental quantification of $3d_{z^2}$ energy reduction. The large $3d_{z^2}$ energy reduction contributes to raising the anisotropy barrier in $Li_2(Li_{1-x}Fe_x)N$, and is much greater than values calculated for other linear monovalent SIMs, including the first two coordinate complex, $[Fe(C(SiMe_3)_3)_2]^-$.[6] Focusing then on low concentration $Li_2(Li_{1-x}Fe_x)N$, variable temperature L_3-edge XAS measurements from 4.5 to 400 K enabled quantification of the magnetic anisotropy barrier to slow magnetic relaxation. Analysis of variable temperature L_3-edge XAS enables determination of the ground state $J = 7/2$ energy splittings. The splitting between the ground $M_J = \pm 7/2$ doublet and first excited $M_J = \pm 5/2$ doublet is 34.80 ± 3.31 meV (280.7 cm^{-1}), this value is consistent with reported U_{eff} values obtained from magnetic relaxation measurements (37.1 and 40.2 meV (298.9 and 324.6 cm^{-1})[12,19]) identifying that magnetisation reversal manifests *via* this through barrier process. The U_{eff} is larger than reported values for other linear Fe SIMs, including $[Fe(C(SiMe_3)_3)_2]^-$ ($U_{eff} = 22.4$ meV, 181 cm^{-1}),[6] but is less than the value recently reported for a linear Co complex $Co^{II}(C(SiMe_2ONaph)_3)_2$ (55.8 meV, 450 cm^{-1})[4] and lanthanide SIMs which can exceed 150 meV.[49] Despite the unexceptional U_{eff} energy for $Li_2(Li_{1-x}Fe_x)N$, the relaxation time at low temperatures certainly is exceptional $\tau = \sim 10^7$ s (ref. 19) in

comparison with other linear SIMs where τ is within a range of seconds and less.

To further understand the origin of the unusually long $Li_2(Li_{1-x}Fe_x)N$ relaxation time, we have analysed the geometric structure and coordination symmetry around Fe dopant sites. EXAFS analysis find both Fe–N bond lengths as 1.873(7) Å, which is exceptionally short for two-coordinate Fe^{I}. The shortness of the Fe–N bonds suggests strong Fe–N π bonding, facilitated by the D_{6h} point symmetry providing equal N 2p π-mixing into both $3d_{xz}$ and $3d_{yz}$ orbitals.[50] Further evidence of this is observed *via* strong satellite intensities present in the $L_{2,3}$-edge XAS spectra. The N–Fe–N angle is analysed by K-edge XANES through single-crystal angular dependence of an intense, low energy, 7113 eV peak. A ligand field interpretation is backed up by DFT calculations, assigning the transition as being associated with unoccupied $4p_{x,y}$ orbitals, from which it is deduced that the N–Fe–N bonding does not deviate from linear. This conclusion is supported by ligand field multiplet simulations that indicate that D_q induced degeneracy breaking of $3d_{xy}$ and $3d_{x^2-y^2}$ cannot exceed 1 meV for the measured energy reversal barrier to be maintained.

Together the X-ray spectroscopy results identify $Li_2(Li_{1-x}Fe_x)N$ as an ideal model system clean of stoichiometric vacancies where Fe sites are geometrically equivalent. The doping of Fe ions into the lithium nitride host matrix enables control of inter-SIM distances, from which dipolar fields can be minimised. The introduction of Fe sites displace Li ions at 2*c* positions causing a local bond contraction of 0.062(7) Å with respect to the equivalent Li–N bond. The linear N–Fe–N core is supported through $3d_{xz,yz}$-Nπ mixing and indirectly by the hexagonal lithium nitride lattice, that acts to drive bond shortening and rigorous linearity, in a similar but more direct way than dispersion force stabilisation observed in other linear molecular complexes, including $Fe[N(SiMe_3)Dipp]_2$.[38]

Previous theoretical studies have identified the crucial influence of reduced symmetry and Renner–Teller vibronic coupling on the magnetic relaxation time in two coordinate Fe SIMs.[51] It is proposed that the combination of a short Fe–N bond, related strong 3dπ bonding, and high point symmetry imposed by the hexagonal lithium nitride lattice contribute to suppress vibronic effects, resulting in increased magnetic relaxation times with respect to other linear SIMs. The high point symmetry of the solid-state host lattice exhibit less disorder with respect to large inorganic coordination complexes. The high symmetry of the crystal host lattice and geometric equivalence of Fe dopant sites, result in a very low propensity for dislocation-induced strain type variations in local symmetry and easy axis directions, consistent with the extreme field dependence reported in $Li_2(Li_{1-x}Fe_x)N$.[13,19]

The quantification of electronic structure reported here provides insights relevant for the advance of high performance magnets free from rare-earth metals. The extraordinary electronic and magnetic properties of $Li_2(Li_{1-x}Fe_x)N$, highlights the potential of doping paramagnetic ions within high symmetry solid-state lattices. Another area of potential relevance is nanoscale information storage for which there is currently considerable effort devoted to depositing coordination complexes with SIM properties on surfaces.[52,53] An even distribution of SIM dopant sites within a high symmetry host lattice crystal or thin film[54] offers an interesting alternative method, with additional degrees of freedom for controlling local symmetry and lattice phonon dispersion.

Conflicts of interest

There are no conflicts to declare.

Acknowledgements

We acknowledge Diamond Light Source for experimental time for the following proposals; SI21117 and MM23982 at I10-BLADE and SP20632 at I20-scanning. Use of the Stanford Synchrotron Radiation Lightsource, SLAC National Accelerator Laboratory, is supported by the U.S. Department of Energy, Office of Science, Office of Basic Energy Sciences under Contract No. DE-AC02-76SF00515. This work was supported by the Deutsche Forschungsgemeinschaft (DFG, German Research Foundation) - Grant No. JE748/1. MLB acknowledges the support of the Royal Society of Chemistry (RM1802-4019). David Collison is gratefully acknowledged for stimulating discussions and comments.

Notes and references

1 A. Jesche, L. Ke, J. L. Jacobs, B. Harmon, R. S. Houk and P. C. Canfield, *Phys. Rev. B: Condens. Matter Mater. Phys.*, 2015, **91**, 180403.
2 A. Jesche and P. Canfield, *Philos. Mag.*, 2014, **94**, 2372–2402.
3 M. A. Zykin, P. E. Kazin and M. Jansen, *Chem.–Eur. J.*, 2020, **26**, 8834–8844.
4 P. C. Bunting, M. Atanasov, E. Damgaard-Møller, M. Perfetti, I. Crassee, M. Orlita, J. Overgaard, J. Van Slageren, F. Neese and J. R. Long, *Science*, 2018, **362**, 7319.
5 C. G. Werncke, E. Suturina, P. C. Bunting, L. Vendier, J. R. Long, M. Atanasov, F. Neese, S. Sabo-Etienne and S. Bontemps, *Chem.–Eur. J.*, 2016, **22**, 1668–1674.
6 J. M. Zadrozny, D. J. Xiao, M. Atanasov, G. J. Long, F. Grandjean, F. Neese and J. R. Long, *Nat. Chem.*, 2013, **5**, 577–581.
7 J. M. Zadrozny, D. J. Xiao, J. R. Long, M. Atanasov, F. Neese, F. Grandjean and G. J. Long, *Inorg. Chem.*, 2013, **52**, 13123–13131.
8 M. K. Thomsen, A. Nyvang, J. P. Walsh, P. C. Bunting, J. R. Long, F. Neese, M. Atanasov, A. Genoni and J. Overgaard, *Inorg. Chem.*, 2019, **58**, 3211–3218.
9 P. P. Power, *Comments Inorg. Chem.*, 2012, **8**, 177–202.
10 C. J. Pollock, M. U. Delgado-Jaime, M. Atanasov, F. Neese and S. Debeer, *J. Am. Chem. Soc.*, 2014, **136**, 9453–9463.
11 F. de Groot and A. Kotani, *Core level spectroscopy of solids*, CRC Press, 2008, pp. 1–491.
12 A. Jesche, R. W. McCallum, S. Thimmaiah, J. L. Jacobs, V. Taufour, A. Kreyssig, R. S. Houk, S. L. Bud'Ko and P. C. Canfield, *Nat. Commun.*, 2014, **5**, 3333.

13 M. Fix, A. Jesche, S. G. Jantz, S. A. Bräuninger, H. H. Klauss, R. S. Manna, I. M. Pietsch, H. A. Höppe and P. C. Canfield, *Phys. Rev. B*, 2018, **97**, 064419.
14 P. Novák and F. R. Wagner, *Phys. Rev. B: Condens. Matter Mater. Phys.*, 2002, **66**, 1–6.
15 L. Ke and M. Van Schilfgaarde, *Phys. Rev. B: Condens. Matter Mater. Phys.*, 2015, **92**, 014423.
16 A. Yamada, S. Matsumoto and Y. Nakamura, *J. Mater. Chem.*, 2011, **21**, 10021–10025.
17 R. Niewa, Z. Hu and R. Kniep, *Eur. J. Inorg. Chem.*, 2003, **2003**(8), 1632–1634.
18 V. Ksenofontov, S. Reiman, M. Waldeck, R. Niewa, R. Kniep and P. Gütlich, *Z. Anorg. Allg. Chem.*, 2003, **629**, 1787–1794.
19 M. Fix, J. H. Atkinson, P. C. Canfield, E. Del Barco and A. Jesche, *Phys. Rev. Lett.*, 2018, **120**, 147202.
20 L. Xu, Z. Zangeneh, R. Yadav, S. Avdoshenko, J. Van Den Brink, A. Jesche and L. Hozoi, *Nanoscale*, 2017, **9**, 10596–10600.
21 S. Hayama, G. Duller, J. P. Sutter, M. Amboage, R. Boada, A. Freeman, L. Keenan, B. Nutter, L. Cahill, P. Leicester, B. Kemp, N. Rubies and S. Diaz-Moreno, *J. Synchrotron Radiat.*, 2018, **25**, 1556–1564.
22 H. J. Beister, S. Haag, R. Kniep, K. Strössner and K. Syassen, *Angew. Chem., Int. Ed. Engl.*, 1988, **27**, 1101–1103.
23 B. Ravel and M. Newville, *J. Synchrotron Radiat.*, 2005, **12**, 537–541.
24 E. C. Wasinger, F. M. De Groot, B. Hedman, K. O. Hodgson and E. I. Solomon, *J. Am. Chem. Soc.*, 2003, **125**, 12894–12906.
25 M. W. Haverkort, M. Zwierzycki and O. K. Andersen, *Phys. Rev. B: Condens. Matter Mater. Phys.*, 2012, **85**, 165113.
26 M. Retegan, *Crispy: v0.7.3*, 2019, DOI: 10.5281/zenodo.1008184.
27 P. Giannozzi, S. Baroni, N. Bonini, M. Calandra, R. Car, C. Cavazzoni, D. Ceresoli, G. L. Chiarotti, M. Cococcioni, I. Dabo, A. Dal Corso, S. De Gironcoli, S. Fabris, G. Fratesi, R. Gebauer, U. Gerstmann, C. Gougoussis, A. Kokalj, M. Lazzeri, L. Martin-Samos, N. Marzari, F. Mauri, R. Mazzarello, S. Paolini, A. Pasquarello, L. Paulatto, C. Sbraccia, S. Scandolo, G. Sclauzero, A. P. Seitsonen, A. Smogunov, P. Umari and R. M. Wentzcovitch, *J. Phys.: Condens. Matter*, 2009, **21**, 395502.
28 S. J. Clark, M. D. Segall, C. J. Pickard, P. J. Hasnip, M. I. Probert, K. Refson and M. C. Payne, *Z. Kristallogr. Cryst. Mater.*, 2005, **220**, 567–570.
29 J. P. Perdew, K. Burke and M. Ernzerhof, *Phys. Rev. Lett.*, 1996, **77**, 3865–3868.
30 A. Dal Corso, *Comput. Mater. Sci.*, 2014, **95**, 337–350.
31 S. P. Gao, C. J. Pickard, M. C. Payne, J. Zhu and J. Yuan, *Phys. Rev. B: Condens. Matter Mater. Phys.*, 2008, **77**, 115122.
32 V. I. Anisimov, J. Zaanen and O. K. Andersen, *Phys. Rev. B: Condens. Matter Mater. Phys.*, 1991, **44**, 943–954.
33 M. Cococcioni and S. De Gironcoli, *Phys. Rev. B: Condens. Matter Mater. Phys.*, 2005, **71**, 035105.
34 V. P. Antropov and V. N. Antonov, *Phys. Rev. B: Condens. Matter Mater. Phys.*, 2014, **90**, 94406.
35 J. Klatyk and R. Kniep, *Z. Kristallogr. NCS*, 1999, **214**, 447–448.
36 C. Gunnar Werncke, P. C. Bunting, C. Duhayon, J. R. Long, S. Bontemps and S. Sabo-Etienne, *Angew. Chem., Int. Ed.*, 2015, **54**, 245–248.
37 C. Y. Lin, J. C. Fettinger, F. Grandjean, G. J. Long and P. P. Power, *Inorg. Chem.*, 2014, **53**, 9400–9406.
38 C. Y. Lin, J. D. Guo, J. C. Fettinger, S. Nagase, F. Grandjean, G. J. Long, N. F. Chilton and P. P. Power, *Inorg. Chem.*, 2013, **52**, 13584–13593.
39 D. Muller-Bouvet, J. P. Pereira-Ramos, S. Bach, P. Willmann and A. Michalowicz, *Inorg. Chem.*, 2014, **53**, 6127–6131.
40 J. Klatyk, W. Schnelle, F. R. Wagner, R. Niewa, P. Novák, R. Kniep, M. Waldeck, V. Ksenofontov and P. Gütlich, *Phys. Rev. Lett.*, 2002, **88**, 2072021–2072024.
41 S. D. Kelly, D. Hesterberg and B. Ravel, *Methods of Soil Analysis Part 5 - Mineralogical Methods*, Soil Science Society of America, 2008, ch. 14, pp. 387–463.
42 T. E. Westre, P. Kennepohl, J. G. DeWitt, B. Hedman, K. O. Hodgson and E. I. Solomon, *J. Am. Chem. Soc.*, 1997, **119**, 6297–6314.
43 R. Niewa, Z. Hu and R. Kniep, *Eur. J. Inorg. Chem.*, 2003, **2003**, 1632–1634.
44 L. S. Kau, D. J. Spira-Solomon, J. E. Penner-Hahn, K. O. Hodgson and E. I. Solomon, *J. Am. Chem. Soc.*, 1987, **109**, 6433–6442.
45 W. Zhang, R. Alonso-Mori, U. Bergmann, C. Bressler, M. Chollet, A. Galler, W. Gawelda, R. G. Hadt, R. W. Hartsock, T. Kroll, K. S. Kjær, K. Kubiek, H. T. Lemke, H. W. Liang, D. A. Meyer, M. M. Nielsen, C. Purser, J. S. Robinson, E. I. Solomon, Z. Sun, D. Sokaras, T. B. Van Driel, G. Vankó, T. C. Weng, D. Zhu and K. J. Gaffney, *Nature*, 2014, **509**, 345–348.
46 P. H. Rieger, *J. Magn. Reson.*, 1997, **124**, 140–146.
47 R. D. Cowan, *The Theory of Atomic Structure and Spectra*, University of California Press, 1981, p. 731.
48 S. G. Wang and W. H. Schwarz, *J. Chem. Phys.*, 1998, **109**, 7252–7262.
49 C. A. Goodwin, F. Ortu, D. Reta, N. F. Chilton and D. P. Mills, *Nature*, 2017, **548**, 439–442.
50 W. M. Reiff, C. E. Schulz, M. H. Whangbo, J. I. Seo, Y. S. Lee, G. R. Potratz, C. W. Spicer and G. S. Girolami, *J. Am. Chem. Soc.*, 2009, **131**, 404–405.
51 M. Atanasov, J. M. Zadrozny, J. R. Long and F. Neese, *Chem. Sci.*, 2013, **4**, 139–156.
52 V. E. Campbell, M. Tonelli, I. Cimatti, J. B. Moussy, L. Tortech, Y. J. Dappe, E. Rivière, R. Guillot, S. Delprat, R. Mattana, P. Seneor, P. Ohresser, F. Choueikani, E. Otero, F. Koprowiak, V. G. Chilkuri, N. Suaud, N. Guihéry, A. Galtayries, F. Miserque, M. A. Arrio, P. Sainctavit and T. Mallah, *Nat. Commun.*, 2016, **7**, 13646.
53 M. Mannini, F. Pineider, C. Danieli, F. Totti, L. Sorace, P. Sainctavit, M. A. Arrio, E. Otero, L. Joly, J. C. Cezar, A. Cornia and R. Sessoli, *Nature*, 2010, **468**, 417–421.
54 Y. Li, Y. Sun, A. Pei, K. Chen, A. Vailionis, Y. Li, G. Zheng, J. Sun and Y. Cui, *ACS Cent. Sci.*, 2018, **4**, 97–104.
55 S. A. Bräuninger, A. Jesche, S. Kamusella, F. Seewald, M. Fix, R. Sarkar, A. A. Zvyagin and H.-H. Klauss, *Phys. Rev. B*, 2020, **102**, 054426.

Electronic Supplementary Information:

Single-Ion Magnetism in the Extended Solid-State: Insights from X-ray Absorption and Emission Spectroscopy

Myron S. Huzan,[a b] Manuel Fix,[c] Matteo Aramini,[d] Peter Bencok,[d] J. Fred Mosselmans,[d] Shusaku Hayama,[d] Franziska A. Breitner,[c] Leland B. Gee,[e] Charles J. Titus,[e] Marie-Ann Arrio,[f] Anton Jesche,[c] Michael L. Baker[a b]

[a] *The University of Manchester at Harwell, Diamond Light Source, Harwell Campus, OX11 0DE, UK*

[b] *Department of Chemistry, The University of Manchester, Manchester, M13 9PL, UK*

[c] *EP VI, Center for Electronic Correlations and Magnetism, Institute of Physics, University of Augsburg, D-86159 Augsburg, Germany*

[d] *Diamond Light Source, Harwell Science and Innovation Campus, Chilton, Didcot, OX11 0DE, UK*

[e] *Department of Chemistry, Stanford University, Stanford, CA 94305, USA*

[f] *Institut de Minéralogie, de Physique des Matériaux et de Cosmochimie, CNRS, Sorbonne Université, IRD, MNHN, UMR7590, 75252 Paris Cedex 05, France.*

Contents

S.1 Kβ Comparison

To the authors knowledge there have been no published data of Kβ measurements performed on transition metal ions in linear complexes. Comprehensive studies are documented for Fe^{II} and Fe^{III} of standard symmetries (O_h and D_{4h}), Figure S1 which provides the only comparison for the measured spectrum. Intensity was normalised to the integrated trapezoidal area of each spectra. $Li_2(Li_{1-x}Fe_x)N$ displays closest resemblance to the $S = 2$ or 3/2 Fe model complexes which infer a d^6 or d^7 occupation respectively. However, there exists a strong deviation of K$\beta_{1,3}$ and Kβ' energy splitting and relative intensity limiting further comparative deductions to model complexes.

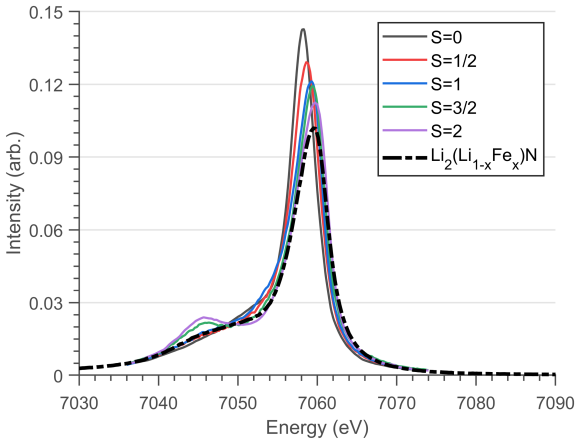

Figure S1: Kβ fluorescence mainline comparison of $Li_2(Li_{1-x}Fe_x)N$ with model Fe^{III} and Fe^{II} complexes with various spin moments of standard symmetries (O_h and D_{4h})[1].

S.2 Experimental XANES Results

XANES displays minimal spectral differences as a function of doping concentration, Figure S2. Slight discrepancies are likely correlated to fluctuating background subtraction or self-absorption effects. Rising edge feature (7113 eV) was isolated and fit with a two peak Pearson-VII fitting routine to extract transition angular dependence described by total area of the peak.

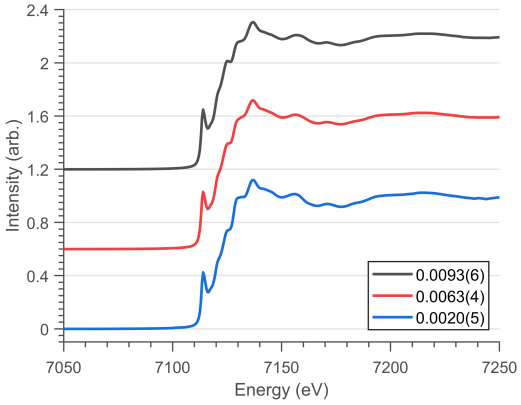

Figure S2: Fe K-edge XANES spectra for various concentrations, x (Values defined in legend) of $Li_2(Li_{1-x}Fe_x)N$.

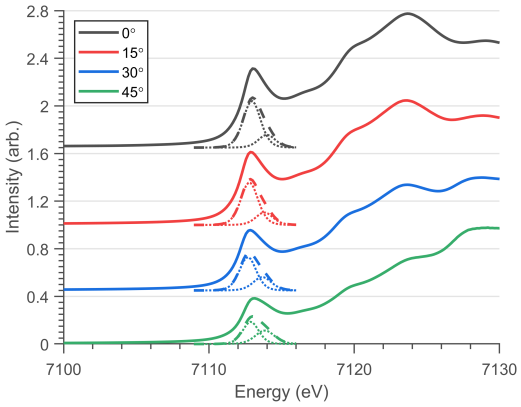

Figure S3: Angular dependent Fe K-edge XANES fitting, isolating the rising-edge peak of $Li_2(Li_{0.985}Fe_{0.015})N$. Dotted lines represent fitted Pearson-VII peaks and dashed lines the total fitted rising-edge area.

S.3 $L_{2,3}$-edge background subtraction

Figure S4 illustrates the background normalisation steps undertaken for the Fe-$L_{2,3}$ spectra. Pre- and Post-Edge normalisation is achieved through a linear fit, while Equation S1 models the background subtraction for the $2p_{3/2}$ and $2p_{1/2}$ continuum states through a double arc-tangent function[2].

$$f(2p_{ctm}) = \frac{h_{L_3}}{\pi}(\arctan(k \cdot (E - E_{L_3})) + \frac{h_{L_2}}{\pi}(\arctan(k \cdot (E - E_{L_2})) \tag{S1}$$

Heights of the arc-tangent (h_{L_3} and h_{L_2}) were set to the approximate minima of each edge while the energy shift is defined as the inflection point of the corresponding edges, E_{L_3} = 705.7 eV and E_{L_2} = 720.3 eV, k = 2.0.

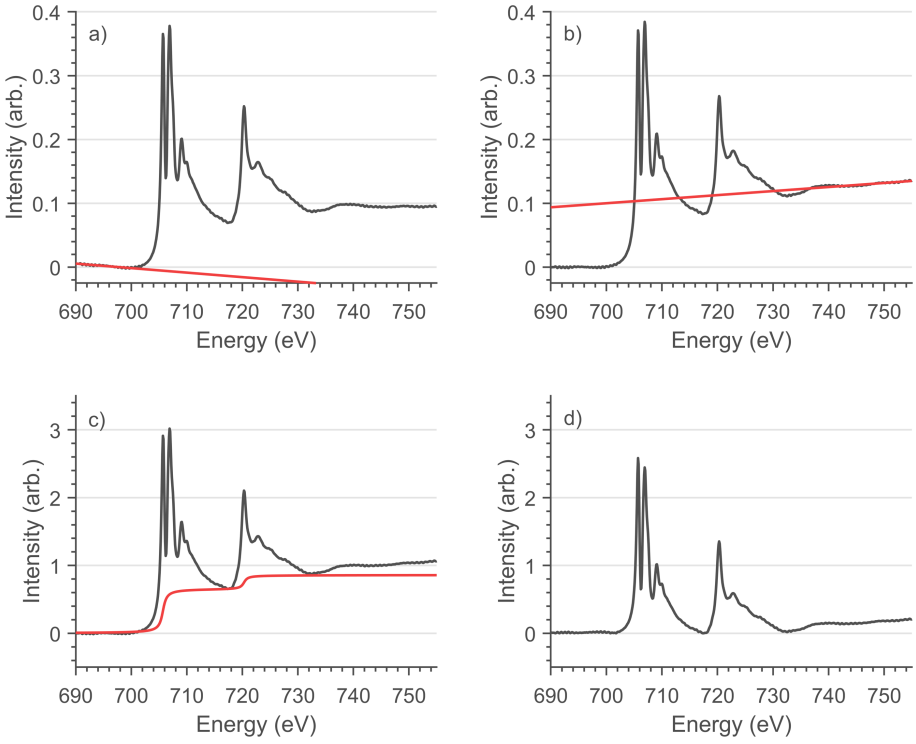

Figure S4: a) Background subtraction through linear fitting to pre-edge (690 - 700 eV), b) Normalisation of spectra through linear fitting to post-edge (735 - 750 eV), c) 2p continuum subtraction of equation S1, d) Normalised and background subtracted $L_{2,3}$-edge spectra of $Li_2(Li_{1-x}Fe_x)N$.

S.4 Density of States

As described in the main body of text DFT calculations were performed within Quantum-Espresso[3] and CASTEP[4] of a 3x3x3 supercell Li_3N matrix doped with a single Fe atom at the Wyckoff 1***b*** position. Interpretation of the converged system included mapping the partial density of states (pDOS), Figure S5. pDOS calculations are an extension of Mulliken population analysis capable of isolating the individual bands and orbitals of a selected atom. Unoccupied $4p_{x,y}$ states characterise the observed rising-edge feature, 7113 eV and $4p_z$ character is shifted to higher energy, as predicted for a linear coordination through a crystal field model.

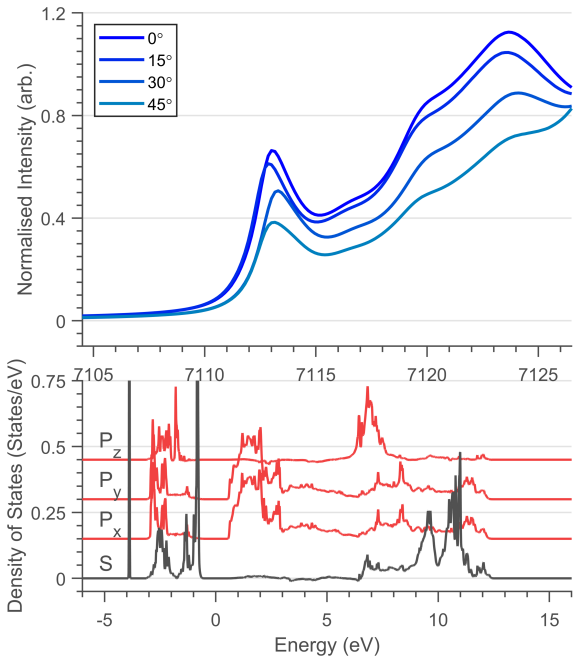

Figure S5: (*Top*) Experimental K-edge XANES of $Li_2(Li_{1-x}Fe_x)N$ with nominal concentration x = 0.0015. (*Bottom*) LDA+U Partial Density of States analysis of Fe s and p states

S.5 $L_{2,3}$-edge Experimental vs CASSCF

ab initio CASSCF calculations by Xu *et al.* predict the experimentally measured magnetic anisotropy of $Li_2(Li_{1-x}Fe_x)N$ to be ∼27 meV with either a linear Fe^{I} or quasilinear Fe^{II} coordination complexes[5]. Figure S6 shows Quanty[6] simulations of $L_{2,3}$-edge spectra of Fe^{I} and Fe^{II} valences. The Slater-Condon-Shortley parameters are reduced to 80% of the calculated Hartree-Fock values to account for over-estimation of the free ion values. Crystal field splittings were extracted from CASSCF calculations, Table S1. These simulations indicated Fe(I) provided the most suitable fit from which crystal field splitting was optimised to best reproduce the experimentally measured spectra.

Table S1: Quanty[6] fitting parameters of simulations presented in Figure 6. Dq, Dt and Ds represent the ligand field splitting parameters of a $D_{6\ h}$ symmetry and ξ_{3d} the spin-orbit coupling parameter deduced from Hartree-Fock calculations. Dq set to zero for all calculations. All values defined in eV.

		CASSCF[5]	
	Best Sim.	Fe(II)	Fe(I)
Dt	0.1806	0.1480	0.1829
Ds	-0.0257	-0.2300	-0.0786
ξ_{3d}	0.0522	0.039	0.045

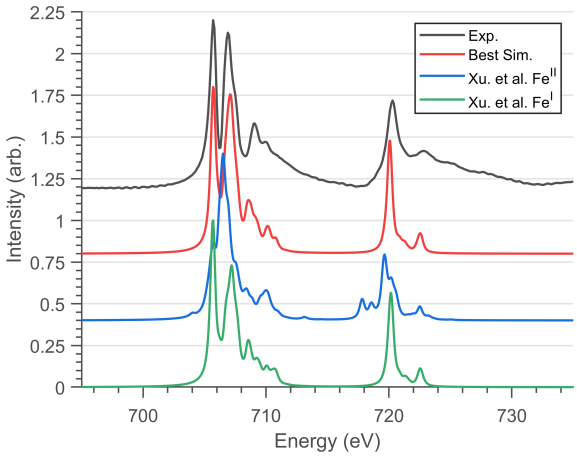

Figure S6: Comparisons of experimental (black), best simulated (red) and Xu *et al.*[5] Fe(II) (blue) and Fe(I) (green) models of Fe $L_{2,3}$-edge spectra. Calculation and experimental measurements undertaken at 4.5 K with L_3 peak maximum normalisation (704 - 708 eV). Ligand field parameters defined in Table S1.

S.6 Quanty Calculation of Anisotropy Barrier

Quanty calculations achieve a second quantisation approach of analytically simulating core-level spectroscopy[6]. Through this technique expectation values of quantum mechanical operators can be applied to the wavefunctions designated to the n electrons present within the basis set. As a result of this energy level separation each M_J doublet can be assigned and quantified.

To replicate the magnetic anisotropy determination undertaken experimentally, a temperature dependent L_3-edge simulation was performed, Figure S7. Fitting of Equation 1 determines an anisotropy energy of $E = 36.87 \pm 0.22$ meV between the ground $M_J = \pm 7/2$ and first excited state, $\pm 5/2$. As reported for the experimental determination of the anisotropy barrier, the calculation assumes equal splitting of the M_J ground-states.

This result is aligned with all previously experimentally and theoretically deduced values of magnetic anisotropy[7,8] and corroborates the technique of utilising $L_{2,3}$-edge temperature dependence to extract magnetic anisotropy of complex systems.

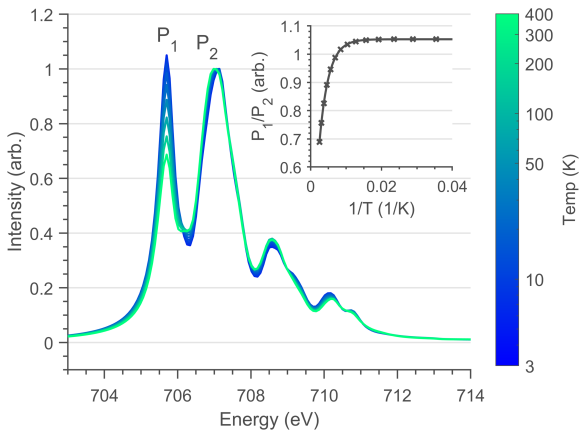

Figure S7: Quanty calculations of Fe L_3-edge as a function of temperature. Normalised through P_1 intensity. (*Inlay*) Least-squares fit of Equation 1 to Quanty simulation L_3 peak ratio with respect to the inverse absolute temperature.

Figure S8 isolates the spectral contribution of each populated M_J doublet to identify the spectral dependence relative to the predominant P_1 and P_2 features. This figure shows that the intensity of P_1 is uniquely related to the $\pm 7/2$ state, verifying the relationship between the temperature

dependence of the P_1 to P_2 ratio and the magnetic anisotropy energy.

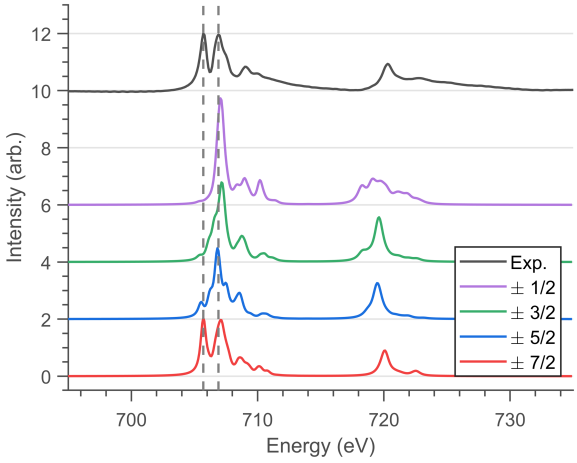

Figure S8: Fe $L_{2,3}$ Quanty calculations of the individual M_J ground-states compared to the experimental $Li_2(Li_{1-x}Fe_x)N$ spectra. Vertical dashed lines represent P_1 and P_2.

Table S2: Expectation values for the J=7/2 manifold based on parameters obtained from the best fit to the $L_{2,3}$-edge spectrum of Fe^{I}, corresponding to the d-orbital electron occupation, spin, S, orbital angular momentum, L and total angular momentum, J, oriented parallel to the principle axis, corresponding with the crystallographic c axis.

E (meV)	$\langle d_{xy} \rangle$	$\langle d_{xz} \rangle$	$\langle d_{z^2} \rangle$	$\langle d_{yz} \rangle$	$\langle d_{x^2-y^2} \rangle$	$\langle S_z \rangle$	$\langle L_z \rangle$	$\langle J_z \rangle$
0	0.9998	1.0002	1.9995	1.0005	2.0000	1.4992	2.0008	3.5000
0	2.0000	1.0005	1.9995	1.0002	0.9998	−1.4992	−2.0008	−3.5000
31.94	1.9885	1.0010	1.9991	1.0005	1.0109	−0.4893	−1.9555	−2.4448
31.94	1.0109	1.0005	1.9991	1.0010	1.9885	0.4893	1.9555	2.4448
66.17	1.9993	1.0010	1.9991	1.0003	1.0003	0.4987	1.9987	1.5000
66.17	1.0003	1.0003	1.9991	1.0010	1.9993	−0.4987	−1.9987	−1.5000
102.19	1.9994	1.0006	1.9994	0.9996	1.0010	−1.4978	−1.9978	−0.5000
102.19	1.0010	0.9996	1.9994	1.0006	1.9994	1.4978	1.9978	0.5000

References

[1] W. Zhang, R. Alonso-Mori, U. Bergmann, C. Bressler, M. Chollet, A. Galler, W. Gawelda, R. G. Hadt, R. W. Hartsock, T. Kroll, K. S. Kjær, K. Kubiek, H. T. Lemke, H. W. Liang, D. A. Meyer, M. M. Nielsen, C. Purser, J. S. Robinson, E. I. Solomon, Z. Sun, D. Sokaras, T. B. Van Driel, G. Vankó, T. C. Weng, D. Zhu and K. J. Gaffney, *Nature*, 2014, **509**, 345–348.

[2] E. C. Wasinger, F. M. De Groot, B. Hedman, K. O. Hodgson and E. I. Solomon, *Journal of the American Chemical Society*, 2003, **125**, 12894–12906.

[3] P. Giannozzi, S. Baroni, N. Bonini, M. Calandra, R. Car, C. Cavazzoni, D. Ceresoli, G. L. Chiarotti, M. Cococcioni, I. Dabo, A. Dal Corso, S. De Gironcoli, S. Fabris, G. Fratesi, R. Gebauer, U. Gerstmann, C. Gougoussis, A. Kokalj, M. Lazzeri, L. Martin-Samos, N. Marzari, F. Mauri, R. Mazzarello, S. Paolini, A. Pasquarello, L. Paulatto, C. Sbraccia, S. Scandolo, G. Sclauzero, A. P. Seitsonen, A. Smogunov, P. Umari and R. M. Wentzcovitch, *Journal of Physics Condensed Matter*, 2009, **21**, 395502.

[4] S. J. Clark, M. D. Segall, C. J. Pickard, P. J. Hasnip, M. I. Probert, K. Refson and M. C. Payne, *Zeitschrift fur Kristallographie*, 2005, **220**, 567–570.

[5] L. Xu, Z. Zangeneh, R. Yadav, S. Avdoshenko, J. Van Den Brink, A. Jesche and L. Hozoi, *Nanoscale*, 2017, **9**, 10596–10600.

[6] M. W. Haverkort, M. Zwierzycki and O. K. Andersen, *Physical Review B - Condensed Matter and Materials Physics*, 2012, **85**, 165113.

[7] A. Jesche, R. W. McCallum, S. Thimmaiah, J. L. Jacobs, V. Taufour, A. Kreyssig, R. S. Houk, S. L. Bud'Ko and P. C. Canfield, *Nature Communications*, 2014, **5**, 3333.

[8] M. Fix, J. H. Atkinson, P. C. Canfield, E. Del Barco and A. Jesche, *Physical Review Letters*, 2018, **120**, 147202.

Chapter 3

$L_{2,3}$-edge XAS and XMCD of linearly coordinated transition metal ions: a study of $3d$-$4s$ mixing and spin-orbit coupling

Fe doped Li_3N facilitates novel magnetic properties, however, insight into the origin of these properties had up to now been lacking, relying primarily on theoretical techniques. Motivated by a prospective Cu(I) d^{10} analogue, a systematic quantification of $Li_2(Li_{1-x}TM_x)N$ was pursued through core-level spectroscopic techniques to investigate how $3d$-$4s$ hybridisation, bonding and magnetism vary along the TM series. $L_{2,3}$-edge XAS and XMCD measurements resolved substantial orbital hybridisation through angular-dependent single-crystal measurements. These results were corroborated both through *ab initio* and multiplet calculations, unravelling the nature of $3d$-$4s$ hybridisation and metal-to-ligand charge-transfer properties throughout the series.

$L_{2,3}$-edge XAS and XMCD of linearly coordinated transition metal ions: a study of $3d$-$4s$ mixing and spin-orbit coupling

Myron S. Huzan,[†,‡] Timothy G. Burrow,[†,‡] Manuel Fix,[¶] Sut Kei Chong,[†] Peter Bencok,[§] Matteo Aramini,[§] Anton Jesche,[¶] and Michael L. Baker[*,†,‡]

†*Department of Chemistry, The University of Manchester, Manchester, M13 9PL, UK*

‡*The University of Manchester at Harwell, Diamond Light Source, Harwell Campus, OX11 0DE, UK*

¶*EP VI, Center for Electronic Correlations and Magnetism, Institute of Physics, University of Augsburg, D-86159 Augsburg, Germany*

§*Diamond Light Source, Harwell Science and Innovation Campus, Chilton, Didcot, OX11 0DE, UK*

E-mail: michael.baker@manchester.ac.uk

Abstract

The influence of *ds* hybridisation due to linear axial ligand fields are predicted for transition metals, lanthanides and actinides. Transition metal sites possessing a linear axial ligand field have been shown to behave as single ion magnets (SIMs) with extremely large energy barriers to spin reversal. This is due to the linear ligand field, that minimises the quenching of orbital angular momentum and is strongly influenced by metal 3*d*-4*s* orbital hybridisation. In this study, single crystal $L_{2,3}$-edge absorption measurements are combined with X-ray magnetic circular dichroism (XMCD) to

quantify how spin-orbit coupling, $3d$-$4s$ orbital hybridisation and bonding influences the electronic structure and magnetism of mono-valent linear TM sites in, $Li_2(Li_{1-x}TM_x)N$ where TM = Mn, Fe, Co, Ni and Cu. It is found that mixing of $3d_{z^2}$ character into the unoccupied $4s$ orbital opens up additional transitions at the $L_{2,3}$-edge, providing a route to evaluate $3d$-$4s$ hybridisation. These transitions are distinguished from metal-ligand, $d\delta$ and $d\pi$, charge-transfer satellites present, due to their distinctive angular dependence. The observed evidence of $3d$-$4s$ hybridisation and metal-ligand covalency are interpreted *via* charge-transfer ligand-field multiplet theory and *ab initio* calculations. The ligand field splitting of the series follow a trend in energy such that $d(\sigma) < d(\delta) < d(\pi)$. XMCD analysis is applied to decompose the spin and orbital contributions to magnetisation for the series. In addition to $3d$-$4s$ hybridisation, significant $3d_{x^2-y^2,xy}$-$L\delta$ and $3d_{xz,yz}$-$L\pi$ bonding is observed and proposed to stabilise TM sites from Renner–Teller vibronic coupling and pseudo Jahn–Teller distortions of which are integral to the high-performance SIM properties present in $Li_2(Li_{1-x}Fe_x)N$.

Introduction

The growing prevalence of low coordination complexes has attracted pronounced interest within molecular magnetism due to exceptional energy barriers to magnetisation reversal at the single-ion level, resulting in a bi-stability of magnetism devoid of long-range ordering. Potential applications for molecular magnets include high-density data storage,[1] quantum computation,[2] and magnetic field sensing.[3] Targeting highly symmetric linear transition metal complexes facilitates an unquenched orbital angular momentum (L) unperturbed by Jahn-Teller distortions. Prominent examples of linear single ion magnets (SIMs) include di-valent $[Co(C(SiMe_3)_3)_2]$[4] and mono-valent $[Fe(C(SiMe_3)_3)_2]^-$[5] which exhibit magnetic remanence and slow magnetic relaxation. The former achieves a non-Aufbau ground-state with maximal orbital angular momentum, $L = 3$ resulting from competing ligand-field stabilisation and interelectronic repulsions of low-lying near-degenerate states; while the latter

exhibits a monovalent $L = 2$ ground-state with $3d_{z^2}$ at lowest energy. Energy reduction of the nd_{z^2} orbital has been predicted by DFT and ligand-field theories[6–8] and *ab initio* calculations[9] due to $nd - (n+1)\,s$ orbital hybridisation extending from transition metals to lanthanides and actinides, where n is the principle quantum number (Figure 1). These studies highlight a preference of molecular moiety linearity that minimises the presence of pseudo-Jahn-Teller contributions correlated to reduced symmetry analogues, significantly reducing the resultant magnetic anisotropic properties. The presence of $nd - (n+1)\,s$ orbital mixing can significantly enhance hyperfine interactions.[10] Exploitation of this effect has led to enhanced quantum clock transitions that are proposed as a route to increase phase time memory in the application of quantum computing.[11] Despite both fundamental and applied implications of $nd - (n+1)\,s$ mixing on electronic structure and magnetism, there have been very few experimental experimental studies[12] and therefore to date most interpretation stems from theory. Thus, this study investigates *ds* hybridisation of an extended solid-state dopant series, $Li_2(Li_{1-x}TM_x)N$ where TM = Mn, Fe, Co, Ni and Cu, through angular dependent single-crystal X-ray absorption spectroscopy (XAS) and X-ray magnetic circular dichroism (XMCD) measurements in conjunction with charge-transfer ligand-field multiplet and *ab initio* calculations.

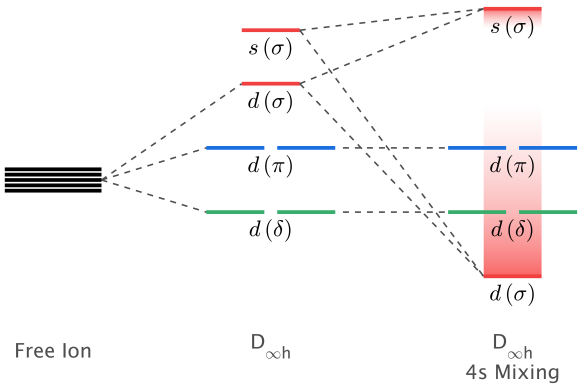

Figure 1: Illustration of energy reordering *d*-orbitals within linear TM system exhibiting nd_{z^2}-$(n+1)\,s$ orbital hybridisation.

Previous experimental quantification of $Li_2(Li_{1-x}Fe_x)N$ confirms a 1+ valence where the

$3d_{z^2}$ orbital is fully occupied due to energy stabilisation *via* $3d$-$4s$ hybridisation.[13] The extended solid-state system of Li_3N has proved an exemplary compound to accommodate high-spin transition metal dopant sites at the single-ion level from Mn through to Ni.[14] Variable-field magnetisation measurements confirm the presence of alternating magnetic anisotropy of easy-planar (Mn, Co) to easy-axis (Fe, Ni) with the Fe analogue exhibiting amongst the largest spin reversal barriers of a transition metal SIM, $U_{eff} = 33\,\text{meV}$,[13,15,16] and relaxation times approaching the highest performing Dy(III) complexes, τ being of the order of $\sim 10^4\,\text{s}$.[16] However, while magnetometry could probe the field dependence of total magnetisation, a generalised interpretation of the spin and orbital contributions to magnetic properties were precluded. In this study, X-ray magnetic circular dichroism (XMCD) is applied to obtain a holistic insight into the origin of the observed magnetic properties in terms of spin and orbital contributions for the $Li_2(Li_{1-x}TM_x)N$ series. Furthermore, angular dependent $L_{2,3}$-edge XAS is found to exhibit sensitivity to $3d$-$4s$ mixing and metal ligand covalency. Together, these detailed insights are found to be imperative to interpreting the electronic structure and magnetic properties of the linear transition metal series. The experimental results of this study are supported *via* both charge-transfer ligand-field multiplet and *ab initio* calculations providing important complimentary insight into electronic and magnetic properties across the $Li_2(Li_{1-x}TM_x)N$ series.

Methods

Preparation of $Li_2(Li_{1-x}TM_x)N$

Synthesis of $Li_2(Li_{1-x}TM_x)N$ single crystals (where TM = Mn, Fe, Co, Ni and Cu) was achieved through a Li-rich solution to the desired concentration, of $x = 0.01$. Detailed information on crystal synthesis is reported by Jesche and Canfield.[17] Metal-ion substitution within the α-Li_3N matrix replaces a Li-ion situated at the $1\boldsymbol{b}$ Wyckoff position. $Li_2(Li_{1-x}TM_x)N$ crystallises as a hexagonal lattice of Li_2N layers alternating with $Li_{1-x}TM_x$

planes perpendicular to the crystallographic c axis.

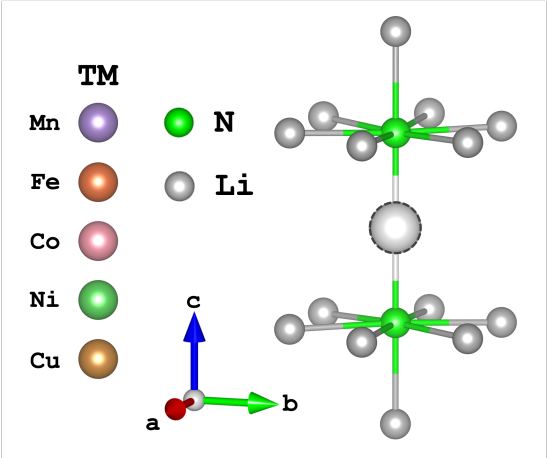

Figure 2: $[Li_{14}TMN_2]^{9+}$ fragment utilised for TD-DFT and CASSCF calculations where TM ions replace the Li-ion at the 1b-Wyckoff position.

.

Experimental

$L_{2,3}$-edge XAS and XMCD measurements were performed at the I10-BLADE high-field magnet end station at Diamond Light Source. Fast energy scans were acquired for each transition metal ion at the respective metal $L_{2,3}$-edges; Mn (620 - 690 eV), Fe (690 - 755 eV), Co (750 - 840 eV), Ni (835 - 920 eV) and Cu (920 - 1000 eV), each at 0.1 eV energy intervals. Measurements were performed at 21 K within an ultra-high vacuum (10^{-10} bar). Total fluorescence yield (TFY) was acquired in a back-scattering geometry using a 10x10 mm^2 silicon diode with a 150 nm Al cover to filter out emitted electrons. Single crystals were mounted with Torr Seal within an argon atmosphere, <0.5 ppm O_2 and H_2O glovebox, onto a copper sample holder and transferred into the XMCD loadlock through a nitrogen-purged glove bag. XMCD measurements were performed at 14 T and collected through the individual detection of right (σ_r) and left (σ_l) circular polarisation with total fluorescence yield (TFY) detection. XAS measurements were acquired through linear horizontal polarisation (σ_h) with TFY detection. Background subtraction of XAS spectra were performed with a linear fitting of the

pre-edge and normalised through a linear fitting of the post-edge. The $2p_{3/2}$ and $2p_{1/2}$ continuum transitions were subtracted through a double arctangent function (Further details of background subtraction see Supplementary Information of Huzan et al. [13]).

Computational

Multiplet calculations

The quantification of charge-transfer ligand field splitting is modelled through multiplet simulations undertaken using the many-body scripting language, Quanty. [18] Quanty input files for the simulation of $L_{2,3}$-edge fluorescence XAS and XMCD were adapted from templates generated in Crispy. [19] Atomic multiplets are given by the Slater-Condon-Shortley integrals, F^k_{dd}, F^k_{pd} (Coulomb) and G^k_{pd}, G^k_{ds}, G^k_{ps} (exchange). An 80% weighting is applied to Hartree-Fock deduced values accounting for the over-estimation of electron-electron repulsions of the free ion. The $2p^5$ spin-orbit coupling values, ξ_{2p} of all transition metal ions remain consistent with the atomic values. The $3d^n$ spin-orbit coupling parameters, ξ_{3d} of Mn and Ni, are left consistent with atomic values. The Fe and Co spin-orbit coupling parameters are scaled to experimentally deduced values provided by temperature-dependent $L_{2,3}$-edge XAS [13] and EPR [20] measurements, respectively. The local symmetry of each transition metal complex is represented in the $D_{\infty h}$ point group, which is equivalent to D_{6h} when $Dq = 0$. This results in a ligand field d-orbital energy splitting of an $A_{1g}(d_{z^2})$ singlet, and two E doublets, $E_{1g}(d_{xy}, d_{yz})$ and $E_{2g}(d_{x^2-y^2}, d_{xy})$ with energies that are adjusted through the crystal field parameters, Ds and Dt. Orbital covalency is considered via a metal-to-ligand charge-transfer configuration with an energy separation, Δ_L and valence bond configuration interaction mixing given by V_L. [21] Where required, differential symmetry adapted metal to ligand charge-transfer [22] is introduced to reproduce back-bonding contributions of the π and δ-bonds. Ligand back-donation is treated with parameters, V_π and V_δ and individual Δ values, Δ_π and Δ_δ. Contributions of $3d$-$4s$ hybridisation is symmetry restricted to the $d\,(\sigma)$-orbital ($3d_{z^2}$) and introduced with an energy separation, Δ_{4s} and orbital overlap parameter, V_{4s}.

Additionally, further exchange Slater-Condon-Shortley integrals are included in the ground, G^2_{ds} and excited states, G^1_{ps}, G^2_{ds}. The ground state is expressed as a linear combination of $\left|3d^N\right\rangle, \left|3d^{N-1}4s\right\rangle$ and $\left|3d^{N-1}L^-\right\rangle$ and was systematically explored by fitting calculated spectra to experiment, to comprehensively deduce the independent bonding contributions for the series of linear transition metal complexes studied. The charge-transfer ligand-field multiplet parameters were informed by the Cu TD-DFT calculations (discussed below) including the relative energy ordering of characteristic satellite features of $s\,(\sigma) < L\,(\delta) < L\,(\pi)$.

ab initio calculations

Time-dependent density functional theory (TD-DFT) and complete active space self-consistent field (CASSCF) calculations presented in this work were performed using the quantum chemistry software suite, ORCA, version 5.0.2.[23] Structural optimisation of N-TM-N bond lengths were calculated through energy minimisation of DFT-SCF calculations for TM = Mn, Ni and Cu of the $[Li_{14}TMN_2]^{9+}$ fragment, Figure 2; EXAFS deduced bond lengths were used for Fe[13] and Co.[24] Calculations used a combination of the def2-TZVPP, def2-TZVP and def2-SVP all-electron basis sets for the transition metal, nitrogen and lithium atoms, respectively. Scalar relativistic effects are included through the second-order Douglas-Kroll-Hess (DKH2) method. TD-DFT calculations applying the BP86 functional were performed with spin multiplicity of the metal centre defined as $2S+1 = 1$ and fragment charge of +9, Figure 2. Unit cell symmetry was constrained to replicate the D_{6h} symmetry of α-Li_3N; previous Fe K-edge $Li_2(Li_{1-x}Fe_x)N$ studies highlighted the strict linearity of the metal-nitrogen bond. There was no significant deviation in the simulated spectroscopic line shape upon varying the Cu-N bond lengths within a reasonable range. Saturation of the spectroscopic features required 150 roots per multiplet, and an empirical shift of 9.33 eV was applied to match the experimental data. State averaged CASSCF calculations in conjunction with N-electron-valence perturbation theory (NEVPT2) were performed with an active space of N electrons in five orbital (N,5), where N = 6 through to 9 for TM = Mn (25 quintets, 135 triplets and

50 singlets), Fe (40 quartets and 80 doublets), Co (30 triplets and 15 singlets) and Ni (5 doublets). The CASSCF-NEVPT2 results were projected using the *ab initio* ligand field theory (AILFT)[25,26] method available within ORCA upon the *d*-orbital basis set giving ligand field parameters (Ds, Dt), Slater integrals (B and C) and spin-orbit coupling (ξ_{3d^n}) for all the metal ions. These parameters were implemented within Quanty to calculate the fluorescence-XAS spectra with absorption final state Slater integrals calculated from Hartree-Fock theory scaled to 80%. Broadenings of all calculated transitions were convolved with a full-width half-maximum Gaussian of 0.25 eV representative of the experimental instrument resolution, and a varying Lorentzian broadening over the L_3 and L_2-edges to account for the core-hole lifetimes (Tabulated values provided in Supplementary Information).

Further DFT calculations on $Li_2(Li_{1-x}Cu_x)N$ presented in this work were performed using the plane-wave pseudopotential DFT method available within the code CASTEP.[27] Generalised-gradient approximation for the exchange-correlation energy was selected in the form of PBE functional revised for solids.[28] Self-consistently generated ultrasoft pseudopotentials were used for both PBE and PBE+U calculations. A kinetic energy cutoff of 750 eV for the wave function, together with a (6x6x6) Monkhorst-Pack k-point grid, were determined as parameters for convergence calculations. A (10x10x10) k-point grid was used instead for calculating the density of states (DOS). Self-consistent calculations were performed to a convergence value of 1×10^{-7} eV. Due to the isolated nature of Cu atoms in $Li_2(Li_{1-x}Cu_x)N$, we operated with a 3x3x3 supercell constructed from the hexagonal cell of Li_3N with a single dopant atom, having space group P6/mmm. The structure was generated using the sample method as previously reported for $Li_2(Li_{1-x}Fe_x)N$.[13] A smearing of 0.1 eV was applied to the computed eigenvalues to improve the k-point convergence. The angular dependence of Cu L_3-edge was calculated, including the effects of core-hole[29] and using the same k-point grid as previously used for the DOS. The ground state DFT was also expanded by expressing the exchange-correlation potential in terms of local-density band theory via the PBE+U method.[30] The electronic properties were calculated with the simplified, rotational-

invariant formulation developed within the linear response approach.[31] An effective U value of 3 eV was included in the calculations. Based on the ground-state energy evaluation and the spectroscopic results, angular-momentum dependent orbital occupation was determined with Löwdin charge analysis on top of ground-state, converged DFT wavefunctions. X-ray absorption spectra were computed by extracting the matrix elements for electronic interband transitions from the ground state DFT, including the local effects of the $2p$ core-hole as implemented in the code CASTEP. An energy shift of 933.38 eV was applied to match the experimental data and normalised through trapezoidal integration of the simulated spectrum. Transition broadening as a consequence of instrumental resolution (Gaussian) and core-lifetime effects (Lorentzian) was set as 0.2 and 0.7 eV FWHM, respectively.

Results and Analysis

Cu(I) $L_{2,3}$-edge XAS and DFT

Single-crystal $L_{2,3}$-edge XMCD measurements of $Li_2(Li_{1-x}Cu_x)N$ show no dichroism at 21 K and 14 T (Figure S1). The absence of XMCD is consistent with a monovalent oxidation state (closed shell Cu-$3d^{10}$). This confirms that previously reported evidence of $Li_2(Li_{1-x}Cu_x)N$ magnetism via magnetic susceptibility is due to the presence of paramagnetic impurities.[32,33] Linearly horizontal polarised $L_{2,3}$-edge XAS of $Li_2(Li_{1-x}Cu_x)N$ display a rich single-crystal angular dependence. Figure 3a shows single-crystal $Li_2(Li_{1-x}Cu_x)N$ measurements acquired over a range of angles from 0 to 70°, where 0° corresponds with the electric vector $\mathbf{E} \perp c$ and 90° with $\mathbf{E} \parallel c$. The $L_{2,3}$-edge XAS of d^{10} Cu(I) is known to exhibit weak dipole transitions into states with unoccupied Cu 4s orbital character,[34] and no angular dependence is expected. The $L_{2,3}$-edge XAS of $Li_2(Li_{1-x}Cu_x)N$ exhibits multiple transitions that carry a strong angular dependence. The L_3 and L_2 edges are very similar; however, the L_3-edge has a higher spectral resolution, and therefore, analysis of transitions are focused on this region of the spectra. The Cu L_3-edge features are dominated by three (I-III) distinct sets of

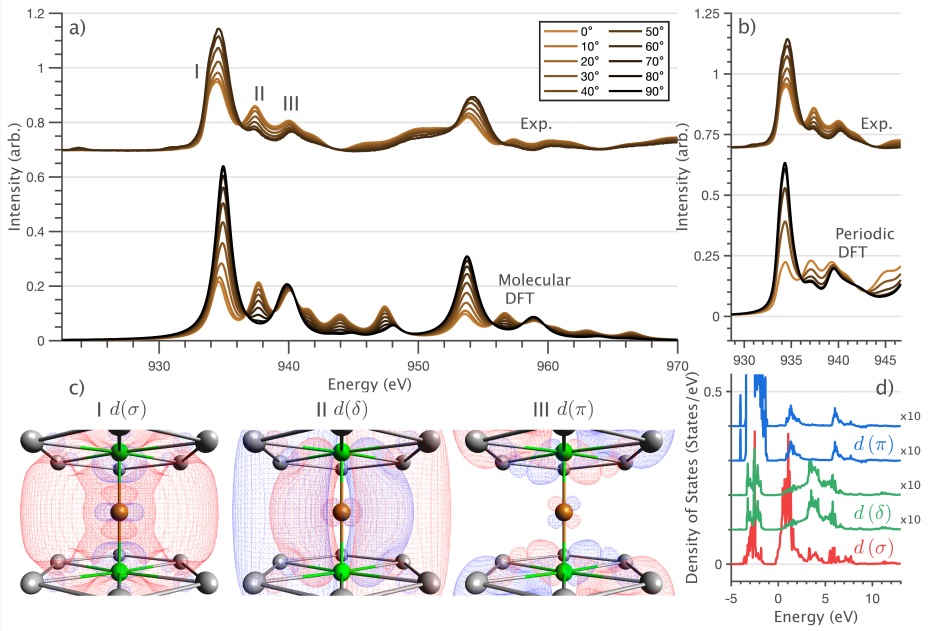

Figure 3: *a*,[*b*])) Single crystal angular dependent Cu $L_{2,3}$[L_3]-edge measurements. (*Top*) Experimental spectra with background subtraction. (*Bottom*) TD-DFT calculated spectra. (*[Bottom]*) Periodic-DFT calculated spectra. 0° corresponds with **E** $\perp$ *c* and 90° with **E** $\parallel$ *c* (*c*)) Löewdin deduced molecular orbital densities with corresponding molecular bonding characters. *d)* DFT calculated project Density of States (pDOS), visualising predominant contributions of Cu-*d* states above the Fermi energy level.

peaks centred at 934.4, 937.4 and 940.1 eV, respectively. Interestingly, peaks I and II exhibit opposing angular dependence. The angular dependence of peak III is composed of multiple overlapping features following a less pronounced angular dependence than I and II.

To assist the transition assignment and investigate the electronic structure further, density functional theory (DFT) calculations are applied to simulate the measured spectra. Since $Li_2(Li_{1-x}Cu_x)N$ is a dopant within an extended solid, it is necessary to identify if the Cu L_3-edge XAS final states are localised to the immediate Cu coordination environment, or if significant transition intensity relates to the band structure of the Li_3N crystal. To address this question, both molecular and periodic DFT calculations are applied to simulate the measured spectra. Both methods are found to accurately reproduce the Cu L_3-edge XAS spectral shape and angular dependence (Figure 3a and b). This confirms that the molecular TD-DFT model based on a $[Li_{14}CuN_2]^{9+}$ fragment suitably captures the essential electronic structure of $Li_2(Li_{1-x}Cu_x)N$ at the dopant sites. The observed peaks can be assigned as resulting from the admixture of Cu 3*d* character into the lowest energy unoccupied orbitals of the local dopant environment. Peak I has maximum intensity with the X-ray electric vector (**E**) parallel with the principle c-axis, and therefore, can be assigned as relating to states with strong Cu-σ mixing. Peak II, with opposing angular dependence to I, is assigned as relating to states with Cu-δ mixing. Peak III has a similar but less resolved angular dependencies than peak II and originates from Cu-π mixing. Löewdin population analysis supports this interpretation (See Supplementary Information). Unoccupied orbitals relating to peak I final states are found to be a competition of N donation and strong Cu 3*d*-4*s* mixing, with 4.9% unoccupied Cu-*s* and 25% unoccupied Cu-d_{z^2} character in addition to 20% N character. Unoccupied orbitals relating to peak II final states exhibit strong δ bonding, with 30.6% unoccupied Cu-$d_{x^2-y^2,xy}$ character. Unoccupied orbitals relating to peak III final states exhibit pronounced unoccupied Cu-$d_{xz,yz}$ character, 1.9% with mixing into both N and Li (see the SI for details).

The molecular TD-DFT natural transition orbitals for peaks I, II and III are shown in

Figure 3c from which characteristic Cu-d_{z^2}-s (σ), Cu-$d_{x^2-y^2,xy}$ (δ) and Cu-$d_{xz,yz}$ (π) orbital shapes can be observed. This assignment is independently confirmed in the projected density of states resulting from the periodic DFT calculation, Figure 3d.

Ni(I) to Mn(I) $L_{2,3}$-edge XAS and XMCD

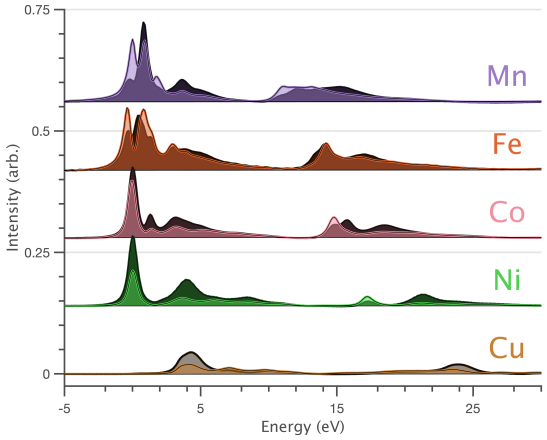

Figure 4: Normal (*light*), $k_i \parallel c$ and grazing (*dark*), $k_i 70° c$ incidence single crystal X-ray absorption spectra of $Li_2(Li_{1-x}TM_x)N$, where TM = Mn, Fe, Co, Ni and Cu performed at 21 K.

An overview of single-crystal $L_{2,3}$-edge XAS measurements for $Li_2(Li_{1-x}TM_x)N$ series are shown in Figure 4. The spectra gain complexity from Cu(I) (d^{10}) through to Mn(I) (d^6) due to the increasing number of d-holes that introduce additional dipole transitions into unoccupied ligand-field and multiplet final-states.

Two large L_3 and L_2 absorption peaks are observed in going from Cu(I) ($3d^{10}$) to Ni(I) ($3d^9$) due to the $3d$-hole. The Ni(I) L_3 and L_2 edge peaks have opposing angular dependence with the L_3-edge showing a maximum intensity with **E** parallel to the crystallographic c-axis and the L_2-edge showing a maximum intensity with **E** perpendicular to the crystallographic c-axis. This angular dependence is unique to the lowest unoccupied molecular orbital being of $3d_{xz,yz}$ character (see SI for further details). The satellite intensity features at energies greater than the main L_3 and L_2 absorption peaks closely resemble the Cu(I) spectra. Furthermore,

the satellites also share the same angular dependencies as the Cu(I) spectra.

The $Li_2(Li_{1-x}Co_x)N$ $L_{2,3}$-edge spectra exhibit the same angular dependencies of the L_3 and L_2 edge peaks as Ni(I). This indicates that the lowest unoccupied molecular orbital is also of $3d_{xz,yz}$ character. The main L_3 and L_2 edge peaks for Co(I) are more intense relative to Ni(I), which is consistent with an additional $3d_{xz,yz}$-hole made available in going from $3d^9$ to $3d^8$. The Co(I) spectra also exhibits an additional peak (1.3 eV) nested between the main edge peaks and the satellites due to $2p$-$3d$ multiplet effects present in the absorption final state.

Spectral assignment of the $L_{2,3}$-edge XAS of Fe(I) and Mn(I) requires ligand-field multiplet theory analysis. However, it is clear that the Ni to Mn series all show strong satellite intensities at energies extending above the L_3 and L_2 edges resembling the Cu(I) spectrum. However, the satellite intensities increasingly overlap with the $2p \rightarrow 3d$, $L_{2,3}$ absorption edges in going from Ni(I) to Mn(I).

CASSCF interpretation

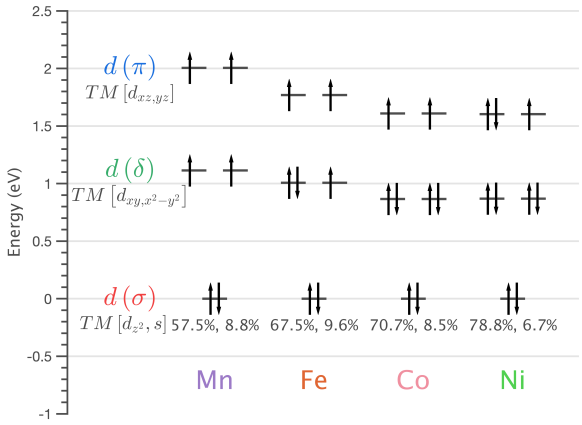

Figure 5: Energies and Löewdin orbital compositions as percentages of $3d$, $4s$ and ligand character of $Li_2(Li_{1-x}TM_x)N$ (where TM = Mn, Fe, Co and Ni). d-orbital energies calculated as one electron eigenfunctions within an AILFT and NEVPT2 calculation.

Ab initio ligand field theory (AILFT) was employed to obtain insights into the ligand-field multiplet structure of the transition metal $L_{2,3}$-edge XAS spectra series. The calculations

predict the d-orbital splitting of the $Li_2(Li_{1-x}TM_x)N$ series, Figure 5. Each transition metal ion exhibits strong $3d$-$4s$ hybridisation with a fully occupied $3d_{z^2}$ orbital at lowest energy. From Mn(I) to Ni(I), the d-orbital splitting narrows in energy due to the varying extent of $4s$ admixture and N-σ donation into the $3d_{z^2}$ orbital.

AILFT calculations provide ligand-field splitting, Slater integrals and spin-orbit coupling parameters, from which the $L_{2,3}$-edge XAS can be calculated, Figure S3. The general ligand-field multiplet structure and angular dependences are reasonably reproduced in the simulations, confirming the +1 oxidation state for the series and a fully occupied $3d_{z^2}$ orbital. The charge transfer satellites present at the high energy side of the L_3 and L_2 edges in the measured spectra are missing from the simulations, as expected for the *ab initio* calculation that is limited to a CASSCF active space including only five $3d$ valence orbitals. The simulated Mn and Fe $L_{2,3}$-edge intensities are distributed over a wide range of energies, indicating how multiplet features also provide significant intensity contributions to the high energy side of the L_3 and L_2 edges. The simulated Co(I) and Ni(I) spectra are much simpler in comparison to Mn(I) and Fe(I) due to the reduced number of multiplet and ligand-field final states. The simulated Co(I) spectrum reproduces the multiplet structure on the high energy side of the edges, and both the Ni(I) and Co(I) spectrum simulations exhibit angular dependence as observed experimentally.

Charge transfer multiplet interpretation

Linearly polarised Ni $L_{2,3}$-edge XAS measurements are shown in Figure 6 with XMCD results Figure 7l and S2. The Ni L_2 and L_3-edge satellite intensities are very similar and show the same angular dependence. However, the L_3-edge satellites are better resolved; hence analysis of the satellite intensities is focused on the former part of the spectrum. The satellites include three distinct features, labelled I, II and III, with different angular dependencies that exhibit equivalent σ, δ and π features as the Cu $L_{2,3}$-edge XAS. Charge transfer ligand field multiplet theory simulations accurately reproduce the satellites in the Ni $L_{2,3}$-edge XAS spectra. This

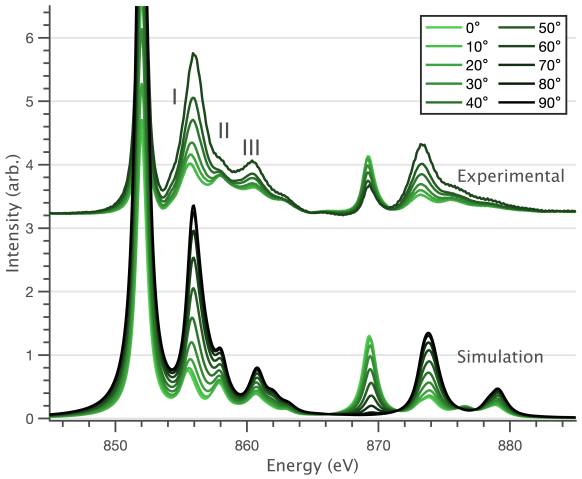

Figure 6: Single crystal angular dependent Ni $L_{2,3}$-edge measurements. (*Top*) Experimental spectra with background subtraction. (*Bottom*) Charge transfer multiplet calculation. 0° corresponds with $\mathbf{E} \perp c$ and 90° with $\mathbf{E} \parallel c$ performed at 21 K and 14 T.

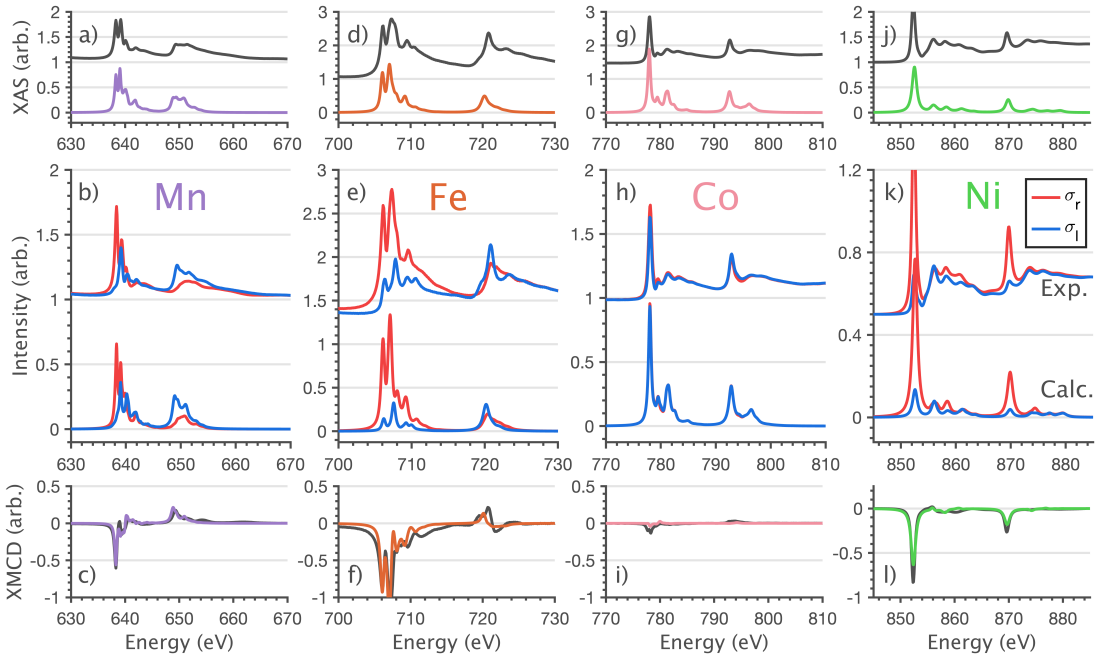

Figure 7: Normal incidence, $k_i \parallel c$, single crystal $Li_2(Li_{1-x}TM_x)N$ (where TM = Mn, Fe and Co) XAS (*a, d, g*) (σ_h), circular polarisation absorption (*b, e, h*) (σ_r and σ_l), and XMCD (*c, f, i*) (σ_r - σ_l) spectra of experimental (*black*) and optimised charge transfer multiplet calculations (*colour*) performed at 21 K and 14 T.

.

calculation confirms the presence of 3*d*-4*s* mixing and metal to ligand donation via both *d*-δ and *d*-σ symmetries. Each satellite feature is distinct and is consistent with the spectral assignments made for $Li_2(Li_{1-x}Cu_x)N$, $s\,(\sigma) < L\,(\delta) < L\,(\pi)$. The XMCD of $Li_2(Li_{1-x}Ni_x)N$ is negative at both the L_3 and L_2 edges, indicating a strongly spin-orbit coupled ground state, Figure 7l and S2. The resultant XMCD is reproduced by the charge-transfer ligand-field multiplet model (Further discussion provided in Supplementary Information).

Single-crystal $L_{2,3}$-edge XAS and XMCD for Co(I), Fe(I) and Mn(I) measured with k_i and H parallel to the crystallographic *c*-axis are shown in Figure 7 and with k_i and H applied within the *a*-*b* plane are shown in Figure S4. The experimental results are shown with the related charge-transfer ligand-field multiplet calculations. Ligand-field multiplet effects distribute intensity over the full $L_{2,3}$-edge region, prohibiting clear isolation of charge transfer satellites. To limit over parameterisation, the multiplet models, shown in Figure 7, for Co(I), Fe(I) and Mn(I) include only 3*d*-4*s* hybridisation and *d*-π metal-ligand charge transfer.

Discussion

The application of sum-rule analysis through XMCD measurements is frequently utilised to unravel spin and orbital contributions to the total magnetic moment. The validity of this technique has been discussed in several reviews, with errors approaching $\pm 30\%$.[35,36] Since single-crystals of $Li_2(Li_{1-x}TM_x)N$ are electrically insulating, total-electron yield detection is inhibited therefore limiting experimental measurements to fluorescence yield detection, which exhibits state and angular-dependent fluorescence decay channels that deviate significantly from the absorption cross-section. The detection method, therefore limits the utility of sum rule analysis even further, with errors proposed in excess of $\pm 50\%$.[37] Therefore, analysis of charge-transfer ligand-field multiplet fits are used to extract the lowest energy expectation values for m_s, m_l and m_j for each TM compound. Table 1 shows the energy and related m_s,

m_l and m_j expectation values for Mn(I) through to Ni(I). The easy-plane magnetisation for both $Li_2(Li_{1-x}Mn_x)N$ and $Li_2(Li_{1-x}Co_x)N$[14] can be understood due to their orbital quenched, ground states resultant from $a_{1g}^2 e_{2g}^2 e_{1g}^2$ and $a_{1g}^2 e_{2g}^4 e_{1g}^2$ configurations respectively. Zero-field splitting of the $S = 2$ and $S = 1$ ground-state multiplets for Mn(I) and Co(I) are responsible for the easy-plane type magnetisation observed by single crystal magnetisation measurement (Representative Zeeman calculations are provided within the Supplementary Information). The analysis finds Ni(I) to exhibit a spin-orbit coupled $^2P_{3/2}$ ground state, of total angular momentum of $J = 3/2$ ($S = 1/2$ and $L = 1$) and Fe(I) has a $^4D_{7/2}$ ground state as previously reported.[13] This analysis of the lowest energy eigenstates are cross-examined against CASSCF results, Figure 8. Consistent agreement between the semi-empirical and *ab initio* results are found for the complete series.

Angular dependent single-crystal $L_{2,3}$-edge XAS for the $Li_2(Li_{1-x}TM_x)N$ series enables identification of multiple satellite intensities that relate to both $3dz^2$ enhanced $4s$ transitions and metal-ligand δ and π back-bonding. This is most clearly observed in the case of $Li_2(Li_{1-x}Cu_x)N$ since the closed $3d^{10}$ shell precludes the presence of 2p $\rightarrow$ 3d transitions. The resultant $Li_2(Li_{1-x}Cu_x)N$ $L_{2,3}$-edge XAS spectra can be accurately simulated within either a molecular or periodic DFT framework. Mulliken population analysis of the σ anti-bonding orbital is calculated to exhibit 20.9% Cu-$3dz^2$, 30.2% Cu-$4s$ with the majority of the remaining character as being N-$2p_z$ and Li -$2s$ character

Charge-transfer ligand-field multiplet simulations to accurately reproduce the single-crystal $L_{2,3}$-edge XAS and XMCD of $Li_2(Li_{1-x}Ni_x)N$ require 32.5% $3dz^2$ character in the $4s(\sigma)$ anti-bonding orbital. Similarly, 29% $3dz^2$ into the $4s(\sigma)$ anti-bonding orbital is required to simulate the $Li_2(Li_{1-x}Co_x)N$ spectra. For Fe(I) and Mn(I) the 2p $\rightarrow$ 3d transitions conceal the satellite intensities relating to $3dz^2$ enhanced $4s$ transitions. However, a more reproducible fit to the $L_{2,3}$-edge XAS and XMCD is obtained by including significant $3d$-$4s$ hybridisation.

Table 1: Expectation values of the lowest-lying wavefunctions corresponding to the anisotropic energy barriers, Fig.8 of $Li_2(Li_{1-x}TM_x)N$. E, m_s, m_l, and m_j correspond to eigenvalue calculations of energy, spin, orbital angular momentum and total angular momentum. Energy values in meV.

TM	$\langle E \rangle$	$\langle m_s \rangle$	$\langle m_l \rangle$	$\langle m_j \rangle$
Mn	0.00	0.000	0.000	
	0.25	$\pm$1.022	$\pm$0.002	
	0.98	$\pm$2.045	$\pm$0.002	
Fe	0.00	$\pm$1.505	$\pm$2.002	$\pm$3.506
	31.88	$\pm$0.504	$\pm$2.001	$\pm$2.505
	65.92	$\pm$0.498	$\mp$1.999	$\mp$1.501
	101.67	$\pm$1.503	$\mp$2.000	$\mp$0.497
Co	0.00	0.000	0.000	
	4.14	$\pm$0.910	$\pm$0.010	
Ni	0.00	$\pm$0.486	$\pm$0.948	$\pm$1.471
	75.66	$\pm$0.501	$\mp$0.933	$\pm$0.432

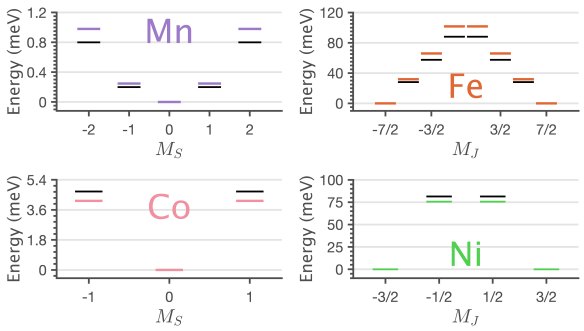

Figure 8: Charge-transfer ligand-field multiplet (*colour*) and AILFT (*black*) determined energy level diagrams of $Li_2(Li_{1-x}TM_x)N$ exhibiting easy-planar, Mn and Co and easy-axis, Fe and Ni anisotropic barriers.

Conclusions and Outlook

A comprehensive study of electronic structure and magnetism is presented for mono-valent linear coordinated transition metal ions TM = Mn, Fe, Co, Ni and Cu doped in $Li_2(Li_{1-x}TM_x)N$ at low concentration (nominal x=0.01). $L_{2,3}$-edge XAS spectra of the series are found to exhibit strong satellite intensities on the high-energy sides of the edges. The satellites have distinctive angular dependencies that enables a precise assignment of transitions in accordance with orbital symmetry. This includes transitions into states with hybridised TM $3d$-$4s$ character, and therefore we identify $L_{2,3}$-edge XAS as a probe for the experimental quantification of ds mixing. The interpretation of the observed spectral satellites are backed up by theory, including molecular based and periodic DFT. A charge-transfer ligand-field multiplet model is developed that introduces $3d_{z^2}$-$4s$ mixing to simulate $L_{2,3}$-edge XAS spectra including satellites and their angular dependencies. Further satellites are identified to originate from metal to ligand charge-transfer of $L\,(\delta)$ and $L\,(\pi)$ symmetries, an assignment that is also backed up by charge-transfer ligand-field multiplet theory and DFT. The ligand field splitting of $3d$ orbitals, as obtained from $L_{2,3}$-edge XAS analysis and AILFT-CASSCF calculations, all follow the same energetic ordering, $s\,(\sigma) < L\,(\delta) < L\,(\pi)$.

Single crystal $L_{2,3}$-edge XMCD measurements provide insight into the origin of observed alternating magnetic anisotropy within the series from Mn(I) to Ni(I). Decomposition of spin and orbital contributions to the total magnetic moment are extracted from charge-transfer ligand-field multiplet calculations. This analysis provides definitive explanation for orbital angular momentum quenched, easy-plane magnetism for Mn and Co, and first-order spin-orbit coupled, easy-axis magnetism for Fe and Ni. The energy barriers to magnetic relaxation with their dominant M_S or M_J composition are calculated via multiplet and CASSCF theory show good agreement. $Li_2(Li_{1-x}Ni_x)N$ calculations predict the largest $U_{eff} \approx 75\,\text{meV}$ of any currently published TM-SIM. Despite this variable-field magnetisation measurements show no indication of magnetic hysteresis.[14] The spin relaxation mechanism suppressing any existence of a bi-stability of magnetism requires further investigation.

Linear transition metal SIMs provide prospective applications as rare-earth-free high-performance magnets, with low coordinate symmetries amongst the most desirable in approaching the single ion magnetic anisotropy limit. Vibronic modes introduced via Renner-Teller contributions are known to significantly reduce magnetic anisotropy barriers.[38] It is proposed that strong covalent $3d_{xz,yz}$-Nπ and $3d_{x^2-y^2,xy}$-Liδ bonding shield the D_{6h} symmetry dopant pocket from vibronic effects.

This study highlights the profound orbital hybridisation within linear transition metal complexes with direct implications on quantum technological developments.[2] The admixture of *s*-orbital hybridisation has been correlated to an increase in the electron-nuclear Fermi contact interaction, which subsequently maximises the hyperfine structure interactions.[11] Harnessing the admixture of *s*-character through extended solid-state systems offers an alternative approach in the tuning of magnetic and nuclear properties of the metal ions, facilitating as of yet unexplored synthetic domains.

Acknowledgement

We acknowledge Diamond Light Source for experimental time for the following proposals; SI21117-1 and MM23982-1 at I10-BLADE. This work was supported by the Deutsche Forschungsgemeinschaft (DFG, German Research Foundation) - Grant No. JE748/1. MLB acknowledges the support of the Royal Society of Chemistry. Eric Mciness is gratefully acknowledged for stimulating discussions and comments.

References

(1) Mannini, M.; Pineider, F.; Danieli, C.; Totti, F.; Sorace, L.; Sainctavit, P.; Arrio, M. A.; Otero, E.; Joly, L.; Cezar, J. C.; Cornia, A.; Sessoli, R. Quantum tunnelling of the magnetization in a monolayer of oriented single-molecule magnets. *Nature* **2010**, *468*, 417–421.

(2) Gaita-Ariño, A.; Luis, F.; Hill, S.; Coronado, E. Molecular spins for quantum computation. 2019.

(3) Leuenberger, M. N.; Mucciolo, E. R. Berry-phase oscillations of the Kondo effect in single-molecule magnets. *Physical Review Letters* **2006**, *97*, 126601.

(4) Bunting, P. C.; Atanasov, M.; Damgaard-Møller, E.; Perfetti, M.; Crassee, I.; Orlita, M.; Overgaard, J.; Van Slageren, J.; Neese, F.; Long, J. R. A linear cobalt(II) complex with maximal orbital angular momentum from a non-Aufbau ground state. *Science* **2018**, *362*, 7319.

(5) Zadrozny, J. M.; Xiao, D. J.; Atanasov, M.; Long, G. J.; Grandjean, F.; Neese, F.; Long, J. R. Magnetic blocking in a linear iron(I) complex. *Nature Chemistry* **2013**, *5*, 577–581.

(6) Wang, S. G.; Schwarz, W. H. Density functional study of first row transition metal dihalides. *Journal of Chemical Physics* **1998**, *109*, 7252–7262.

(7) Vogel, M.; Weber, W.; Wenzel, W. A new ligand field approach to linear transition metal dihalides. *Journal of Chemical Physics* **2006**, *125*, 7252.

(8) Deeth, R. J. Ligand Field Theory for Linear ML2 Complexes. *European Journal of Inorganic Chemistry* **2022**, *2022*.

(9) Guo, F. S.; Tsoureas, N.; Huang, G. Z.; Tong, M. L.; Mansikkamäki, A.; Layfield, R. A. Isolation of a Perfectly Linear Uranium(II) Metallocene. *Angewandte Chemie - International Edition* **2020**, *59*, 2299–2303.

(10) Moehring, S. A.; Miehlich, M.; Hoerger, C. J.; Meyer, K.; Ziller, J. W.; Evans, W. J. A Room-Temperature Stable Y(II) Aryloxide: Using Steric Saturation to Kinetically Stabilize Y(II) Complexes. *Inorganic Chemistry* **2020**, *59*, 3207–3214.

(11) Kundu, K.; White, J. R.; Moehring, S. A.; Yu, J. M.; Ziller, J. W.; Furche, F.; Evans, W. J.; Hill, S. A 9.2-GHz clock transition in a Lu(II) molecular spin qubit arising from a 3,467-MHz hyperfine interaction. *Nature Chemistry* **2022**, *14*, 392–397.

(12) Thomsen, M. K.; Nyvang, A.; Walsh, J. P.; Bunting, P. C.; Long, J. R.; Neese, F.; Atanasov, M.; Genoni, A.; Overgaard, J. Insights into Single-Molecule-Magnet Behavior from the Experimental Electron Density of Linear Two-Coordinate Iron Complexes. *Inorganic Chemistry* **2019**, *58*, 3211–3218.

(13) Huzan, M. S.; Fix, M.; Aramini, M.; Bencok, P.; Mosselmans, J. F. W.; Hayama, S.; Breitner, F. A.; Gee, L. B.; Titus, C. J.; Arrio, M. A.; Jesche, A.; Baker, M. L. Single-ion magnetism in the extended solid-state: Insights from X-ray absorption and emission spectroscopy. *Chemical Science* **2020**, *11*, 11801–11810.

(14) Jesche, A.; Ke, L.; Jacobs, J. L.; Harmon, B.; Houk, R. S.; Canfield, P. C. Alternating magnetic anisotropy of Li2(Li1-xTx) N (T=Mn, Fe, Co, and Ni). *Physical Review B - Condensed Matter and Materials Physics* **2015**, *91*, 180403.

(15) Jesche, A.; McCallum, R. W.; Thimmaiah, S.; Jacobs, J. L.; Taufour, V.; Kreyssig, A.; Houk, R. S.; Bud'Ko, S. L.; Canfield, P. C. Giant magnetic anisotropy and tunnelling of the magnetization in Li 2(Li1-xFex)N. *Nature Communications* **2014**, *5*, 3333.

(16) Fix, M.; Atkinson, J. H.; Canfield, P. C.; Del Barco, E.; Jesche, A. Extreme Field Sensitivity of Magnetic Tunneling in Fe-Doped Li3 N. *Physical Review Letters* **2018**, *120*, 147202.

(17) Jesche, A.; Canfield, P. C. Single crystal growth from light, volatile and reactive materials using lithium and calcium flux. *Philosophical Magazine* **2014**, *94*, 2372–2402.

(18) Haverkort, M. W.; Zwierzycki, M.; Andersen, O. K. Multiplet ligand-field theory using Wannier orbitals. *Physical Review B - Condensed Matter and Materials Physics* **2012**, *85*, 165113.

(19) Retegan, M. Crispy: v0.7.3. 2019.

(20) Albert, C.; Ballé, T. J.; Breitner, F. A.; Krupskaya, Y.; Alfonsov, A.; Zangeneh, Z.; Avdoshenko, S.; Eldeeb, M. S.; Hozoi, L.; Vilangottunjalil, A.; Haubold, E.; Charnukha, A.; Büchner, B.; Jesche, A.; Kataev, V. Terahertz Magneto-Optical Excitations of the sd-Hybrid States of Lithium Nitridocobaltate Li2(Li1- xCox)N. *Inorganic Chemistry* **2021**, *60*, 4497–4507.

(21) Hocking, R. K.; Wasinger, E. C.; De Groot, F. M.; Hodgson, K. O.; Hedman, B.; Solomon, E. I. Fe L-edge XAS studies of K4[Fe(CN)6] and K 3[Fe(CN)6]: A direct probe of back-bonding. *Journal of the American Chemical Society* **2006**, *128*, 10442–10451.

(22) Wasinger, E. C.; De Groot, F. M.; Hedman, B.; Hodgson, K. O.; Solomon, E. I. L-edge X-ray Absorption Spectroscopy of Non-Heme Iron Sites: Experimental Determination of Differential Orbital Covalency. *Journal of the American Chemical Society* **2003**, *125*, 12894–12906.

(23) Neese, F.; Wennmohs, F.; Becker, U.; Riplinger, C. The ORCA quantum chemistry program package. *The Journal of chemical physics* **2020**, *152*, 224108.

(24) Muller-Bouvet, D.; Pereira-Ramos, J. P.; Bach, S.; Willmann, P.; Michalowicz, A. Effect of Cobalt Substitution on Li3-2 xCoxN Local Structure: A XAS Investigation. *Inorganic Chemistry* **2014**, *53*, 6127–6131.

(25) Singh, S. K.; Eng, J.; Atanasov, M.; Neese, F. Covalency and chemical bonding in transition metal complexes: An ab initio based ligand field perspective. *Coordination Chemistry Reviews* **2017**, *344*, 2–25.

(26) Lang, L.; Atanasov, M.; Neese, F. Improvement of Ab Initio Ligand Field Theory by Means of Multistate Perturbation Theory. *Journal of Physical Chemistry A* **2020**, *124*, 1025–1037.

(27) Clark, S. J.; Segall, M. D.; Pickard, C. J.; Hasnip, P. J.; Probert, M. I.; Refson, K.; Payne, M. C. First principles methods using CASTEP. *Zeitschrift fur Kristallographie* **2005**, *220*, 567–570.

(28) Perdew, J. P.; Ruzsinszky, A.; Csonka, G. I.; Vydrov, O. A.; Scuseria, G. E.; Constantin, L. A.; Zhou, X.; Burke, K. Restoring the density-gradient expansion for exchange in solids and surfaces. *Physical Review Letters* **2008**, *100*.

(29) Gao, S. P.; Pickard, C. J.; Payne, M. C.; Zhu, J.; Yuan, J. Theory of core-hole effects in 1s core-level spectroscopy of the first-row elements. *Physical Review B - Condensed Matter and Materials Physics* **2008**, *77*, 115122.

(30) Anisimov, V. I.; Zaanen, J.; Andersen, O. K. Band theory and Mott insulators: Hubbard U instead of Stoner I. *Physical Review B* **1991**, *44*, 943–954.

(31) Cococcioni, M.; De Gironcoli, S. Linear response approach to the calculation of the effective interaction parameters in the LDA+U method. *Physical Review B - Condensed Matter and Materials Physics* **2005**, *71*, 035105.

(32) Schnelle, W.; Niewa, R.; Wagner, F. R. Magnetic and electronic properties of lithium nitridometalates Li 2[(Li1-xTx)N] (T = Co, Ni, Cu). *Journal of Magnetism and Magnetic Materials* **2004**, *272-276*, 828–829.

(33) Novák, P.; Wagner, F. R. Electronic structure and magnetism of 3d metal substituted Li3N. Journal of Magnetism and Magnetic Materials. 2004.

(34) George, S. J.; Cramer, S. P.; Lowery, M. D.; Solomon, E. I. Copper L-Edge Spectral Studies: A Direct Experimental Probe of the Ground-State Covalency in the Blue Copper Site in Plastocyanin. 1993.

(35) Piamonteze, C.; Miedema, P.; De Groot, F. M. Accuracy of the spin sum rule in XMCD

for the transition-metal L edges from manganese to copper. *Physical Review B - Condensed Matter and Materials Physics* **2009**, *80*.

(36) Wang, H.; Friedrich, S.; Li, L.; Mao, Z.; Ge, P.; Balasubramanian, M.; Patil, D. S. L-edge sum rule analysis on 3d transition metal sites: From d10 to d0 and towards application to extremely dilute metallo-enzymes. *Physical Chemistry Chemical Physics* **2018**, *20*, 8166–8176.

(37) Liu, B.; Piamonteze, C.; Delgado-Jaime, M. U.; Wang, R. P.; Heidler, J.; Dreiser, J.; Chopdekar, R.; Nolting, F.; De Groot, F. M. Sum rule distortions in fluorescence-yield x-ray magnetic circular dichroism. *Physical Review B* **2017**, *96*.

(38) Atanasov, M.; Zadrozny, J. M.; Long, J. R.; Neese, F. A theoretical analysis of chemical bonding, vibronic coupling, and magnetic anisotropy in linear iron(ii) complexes with single-molecule magnet behavior. *Chemical Science* **2013**, *4*, 139–156.

Graphical TOC Entry

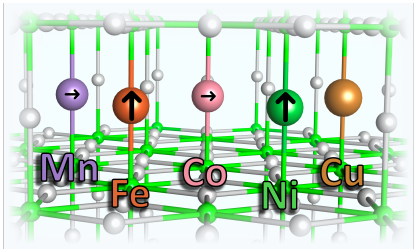

Extended solid-state illustration of the alternating magnetic anisotropy experimentally quantified for linear $Li_2(Li_{1-x}TM_x)N$, where TM = Mn, Fe, Co and Ni and diamagnetic Cu.

Electronic Supplementary Information:

$L_{2,3}$-edge XAS and XMCD of linearly coordinated transition metal ions: a study of 3*d*-4*s* mixing and spin-orbit coupling

Myron S. Huzan,[a] [b] Timothy G. Burrow,[a] [b] Manuel Fix,[c] Sut Kei Chong,[a] Matteo Aramini,[d] Peter Bencok,[d] Anton Jesche,[c] Michael L. Baker[a] [b]

[a] *Department of Chemistry, The University of Manchester, Manchester, M13 9PL, UK*

[b] *The University of Manchester at Harwell, Diamond Light Source, Harwell Campus, OX11 0DE, UK*

[c] *EP VI, Center for Electronic Correlations and Magnetism, Institute of Physics, University of Augsburg, D-86159 Augsburg, Germany*

[d] *Diamond Light Source, Harwell Science and Innovation Campus, Chilton, Didcot, OX11 0DE, UK*

Contents

S.1 Cu $L_{2,3}$-edge XMCD

Figure S1 presents experimental $Li_2(Li_{1-x}Cu_x)N$ $L_{2,3}$-edge XMCD measurement. The absence of any dichroism is indicative of a system exhibiting no magnetic phenomena upon application of a 14 T field. This strongly suggests a near-closed shell Cu(I), d^{10} valence with spectral features corresponding to orbital and ligand hybridisation; full discussion within the main body of text.

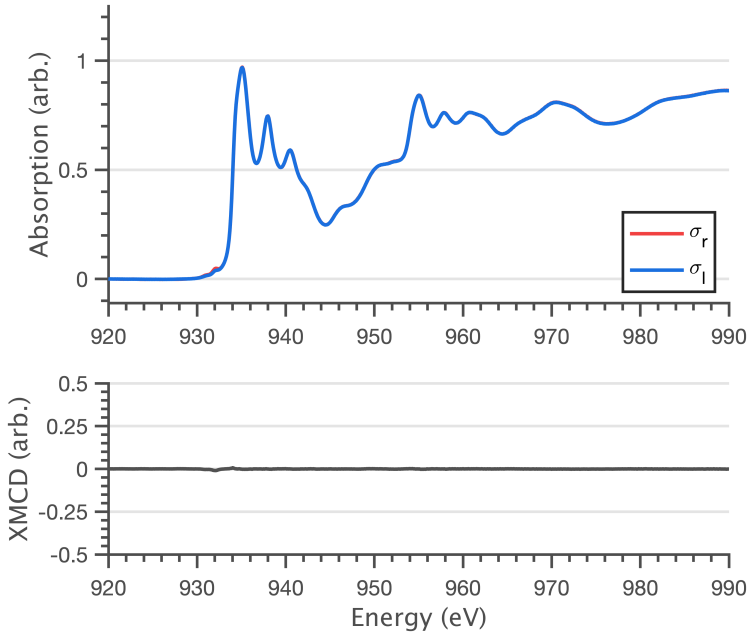

Figure S1: Single crystal $Li_2(Li_{1-x}Cu_x)N$ $L_{2,3}$-edge spectra. (*Top*) Normal incidence, $k_i \parallel c$, circularly polarised absorption, (σ_l and σ_r) and (*bottom*) XMCD (σ_l - σ_r) $L_{2,3}$-edge spectra performed at 21 K and 14 T.

S.2 Ni(I) absorption cross-section selection rules

Figure S2 presents ligand-field calculations of Ni(I), d^9 $L_{2,3}$-edge XAS and XMCD angular dependencies. Ni(I) presents the simplest illustration of an $L_{2,3}$-edge calculations dependent solely on the orbital location of the lone hole. The presence of an Ni L_2-edge, 869.7 eV, within the experimental spectra (Figure 6) forbids an atomic-like description of the Ni ion exhibiting maximal Hund's rule occupancy, ($L = 2$) (Figure S2e); by virtue of a completely filled $3d_{1/2}$ state. While this is not unforeseen through rudimentary ligand-field arguments, the observed opposing angular dependencies within the experimental measurements of the L_3 and L_2 edges (Figure S2b) compels an electronic ordering of $d(\sigma) < d(\delta) < d(\pi)$ or $d(\delta) < d(\sigma) < d(\pi)$; as an unoccupied $d(\sigma)$ orbital ($L = 0$) would exhibit an incorrect negative-positive XMCD signal Figure S2h. This technique facilitates an understanding of the general electronic occupation of the Ni(I); but it is limited to primitive labelling of the lone hole. To further quantify the electronic ordering of the complete d-orbital manifolds *ab initio* and charge-transfer ligand-field multiplet calculations are utilised within the main-body of the text.

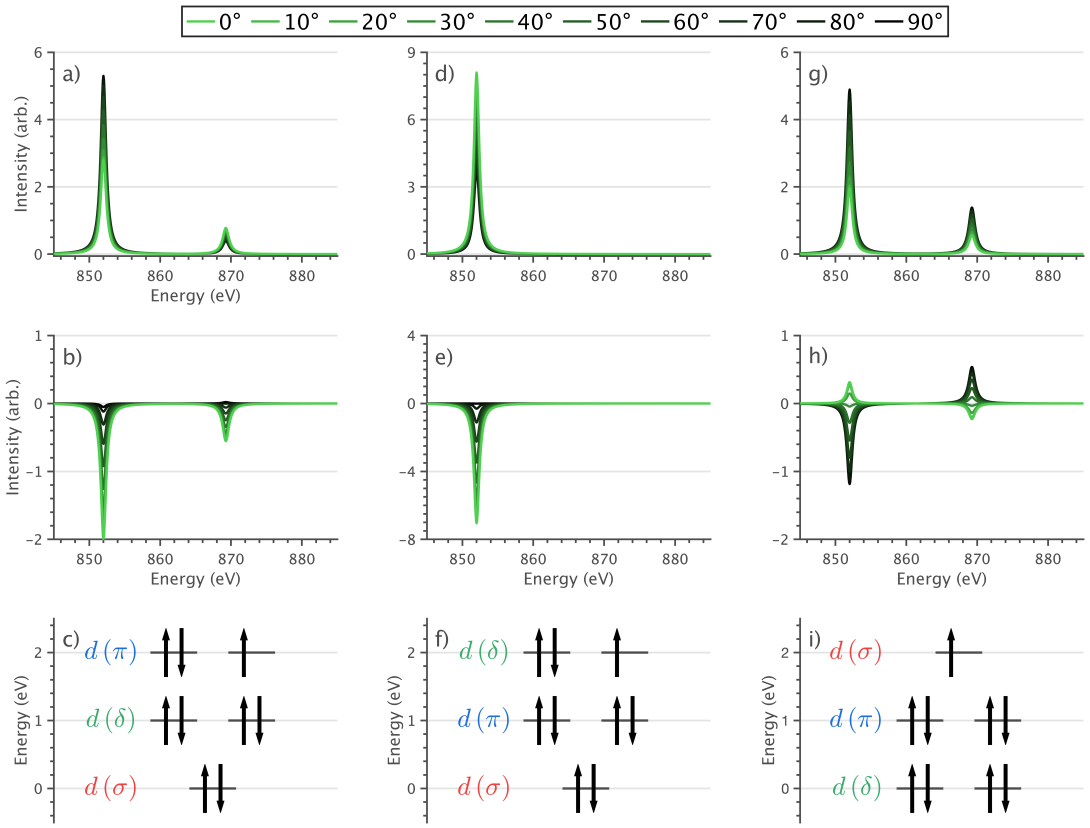

Figure S2: Ni $L_{2,3}$-edge charge-transfer ligand-field multiplet calculations of (*a, d, g*) X-ray absorption, (*b, e, h*) and X-ray magnetic circular dichroism calculations with representative electronic (d^9) occupations. Itterative angular dependent calculations performed with incident, $k_i \parallel c$ (0°) through to $k_i \perp c$ (90°) at 21 K and 14 T.

S.3 Mulliken and Löewdin population analysis of Cu DFT

Table S1 presents metal and ligand anti-bonding molecular orbital character as calculated through Mulliken and Löewdin population analysis. Orbital multiplicities are denoted in square parentheses of symmetrically equivalent ligand orbital sites. For conciseness, orbital character is limited to percentage character above 1%.

Table S1: Metal and ligand anti-bonding Mulliken (*top*) and Löewdin (*bottom*) deduced molecular orbital characters (%) of TD-DFT Cu $L_{2,3}$-edge transitions, Figure 3a.

Mulliken

Peak I		Peak II				Peak III			
Cu s	30.2	Cu $d_{x^2-y^2}$	46.9	Cu d_{xy}	46.9	Cu d_{xz}	-5.2	Cu d_{yz}	-5.2
Cu d_{z^2}	20.9	Li p_y [x4]	6.4	Li s [x4]	2.7	N p_x [x2]	2.8	N p_y [x2]	2.8
N s [x2]	1.1	Li s [x8]	2.0	Li p_x [x8]	4.0	Li s [x4]	15.9	Li s [x8]	11.9
N p_z [x2]	8.3					Li p_z [x4]	1.3	Li p_z [x8]	1.0
Li s [x12]	2.6					Li p_x [x8]	-2.3	Li p_y [x12]	-1.7
Li s [x2]	2.2					Li p_x [x2]	3.3	Li p_y [x2]	3.3
						Li s [x8]	4.4		

Löewdin

Peak I		Peak II				Peak III			
Cu s	4.8	Cu $d_{x^2-y^2}$	35.8	Cu d_{xy}	35.8	Cu d_{xz}	3.9	Cu d_{yz}	3.9
Cu d_{z^2}	28.2	Li p_y [x4]	8.2	Li s [x4]	1.1	N p_x [x2]	3.6	N p_y [x2]	3.6
N s [x2]	4.7	Li p_x [x8]	1.7	Li p_x [x8]	4.5	Li s [x4]	2.2	Li s [x8]	2.5
N p_z [x2]	7.2			Li p_y [x8]	1.7	Li p_z [x4]	6.7	Li p_z [x8]	5.0
Li s [x12]	2.6					Li p_z [x8]	1.7	Li p_y [x4]	1.6
						Li p_x [x2]	11.5	Li p_y [x2]	11.5

S.4 Multiplet Parameters

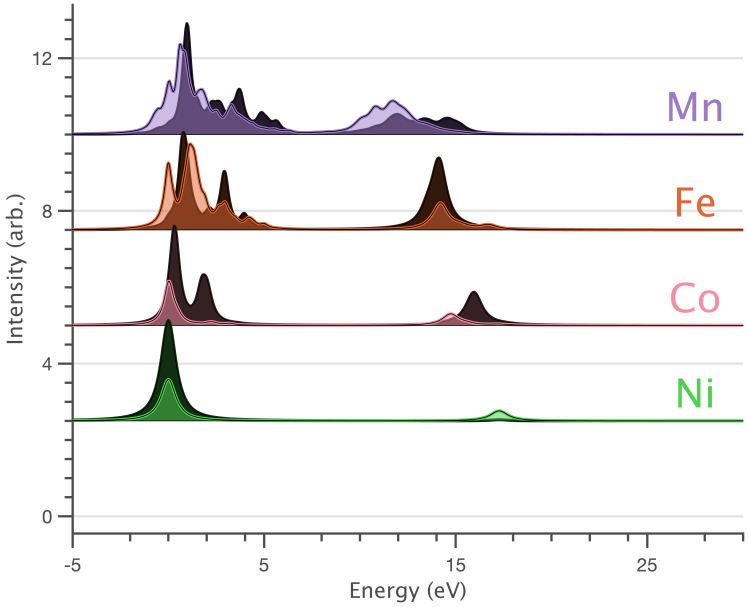

Figure S3: Normal (*light*), $k_i \parallel c$ and grazing (*dark*), $k_i 70° c$ incidence single crystal X-ray absorption spectra of $Li_2(Li_{1-x}TM_x)N$, where TM = Mn, Fe, Co and Ni calculated through AILFT deduced multiplet calculations (Table S3) at 21 K.

Table S2: Ground (GS, $3d^n$) and excited-state (ES, $2p^5 3d^{n-1}$) charge-transfer ligand-field multiplet parameters of optimised $Li_2(Li_{1-x}TM_x)N$ $L_{2,3}$-edge calculations; all values in eV.

	$Li_2(Li_{1-x}Ni_x)N$		$Li_2(Li_{1-x}Co_x)N$		$Li_2(Li_{1-x}Fe_x)N$		$Li_2(Li_{1-x}Mn_x)N$	
	GS	ES	GS	ES	GS	ES	GS	ES
F^2_{dd}	8.8672	9.5120	8.3440	9.0088	7.8088	8.4976	7.2576	7.9768
F^4_{dd}	5.4680	5.8744	5.1448	5.5632	4.8136	5.2472	4.4720	4.9248
F^2_{pd}		5.6784		5.2992		4.9136		4.5216
G^1_{pd}		4.2096		3.8920		3.5704		3.2448
G^3_{pd}		2.3944		2.2128		2.0296		1.8432
G^2_{ds}	0.9656	0.8584	0.9704	0.8560	0.9768	0.8569	0.9888	0.8576
G^1_{ps}		0.1472		0.1456		0.1440		0.1424
ξ_{2p}		11.509		9.750		8.530		7.121
ξ_{3d}	0.074	0.093	0.054[1]	0.069[1]	0.052[2]	0.068[2]	0.035	0.046
Ds	-0.0429	-0.0429	-0.0729	-0.0729	0.186	0.186	-0.0286	-0.0286
Dt	0.2324	0.2324	0.2683	0.2683	0.2011	0.2011	0.1789	0.1789
Δ_{4s}	1.25	2.25	0.458	1.458	1.67	2.67	1.38	2.38
V_{4s}	7.49	7.49	5.37	5.37	2.68	2.68	2.12	2.12
$\Delta_{[\delta]\pi}$	[4.40] 6.80	[5.40] 7.80	2.40	3.40	2.25	3.25	3.74	4.74
$V_{[\delta]\pi}$	[0.80] 1.80	[0.80] 1.80	1.40	1.40	0.50	0.50	0.83	0.83

[a]Scaling of 92% to atomic value as determined from EPR measurements[1].

[b]Scaling of 116% to atomic value as determined from temperature dependent X-ray absorption measurements[2].

Table S3: CASSCF AILFT deduced $Li_2(Li_{1-x}TM_x)N$ ground-state ($3d^n$) multiplet parameters, excited-state ($3d^{n+1}$) values scaled to 80% Hartree-Fock deduced values (See Table S2) with associated TM-N deduced bond lengths; all values in eV unless stated otherwise.

	Ni	Co	Fe	Mn
F^2_{dd}	0.000	6.788	6.065	5.425
F^4_{dd}	0.000	3.644	4.101	3.627
ξ_{3d}	0.071	0.054	0.041	0.030
Ds	0.0193	0.0171	0.0353	0.0319
Dt	0.1584	0.1671	0.1732	0.1973
TM-N (Å)	1.8479[2]	1.8100[1]	1.8737[1]	1.8791[2]

[a]Experimentally deduced from EXAFS measurements, Co[3] and Fe[2].

[b]SCF energy minimised within the BP86 functional.

Table S4: Ground-state expectation values of the electronic occupation of $3d$, $4s$ and ligand orbitals for $Li_2(Li_{1-x}TM_x)N$ of the optimised charge-transfer ligand-field multiplet parameters (Table S2).

	Ni	Co	Fe	Mn
$\langle d_{z^2} \rangle$	1.6151	1.6280	1.7742	1.6803
$\langle d_{x^2-y^2}, d_{xy} \rangle$	3.9631	3.8425	2.9912	1.9988
$\langle d_{xz}, d_{yz} \rangle$	2.9042	1.9528	1.9676	1.9622
$\langle 3d \rangle$	8.4823	7.4232	6.7330	5.6413
$\langle 4s \rangle$	0.3931	0.3699	0.2244	0.3170
$\langle L \rangle$	0.1246	0.2068	0.0426	0.0417

Table S5: Full-width half maximum, FWHM Lorentzian core-hole life time broadenings applied to calculated $L_{2,3}$-edge spectra. Gaussian FWHM consistent throughout all calculations of 0.25 eV. All values in eV.

	Cu	Ni	Co	Fe	Mn
Γ L_3, L_2	1.40, 1.85	0.55, 1.10	0.45, 1.00	0.35, 0.90	0.25, 0.80

S.5 Grazing incidence XAS and XMCD

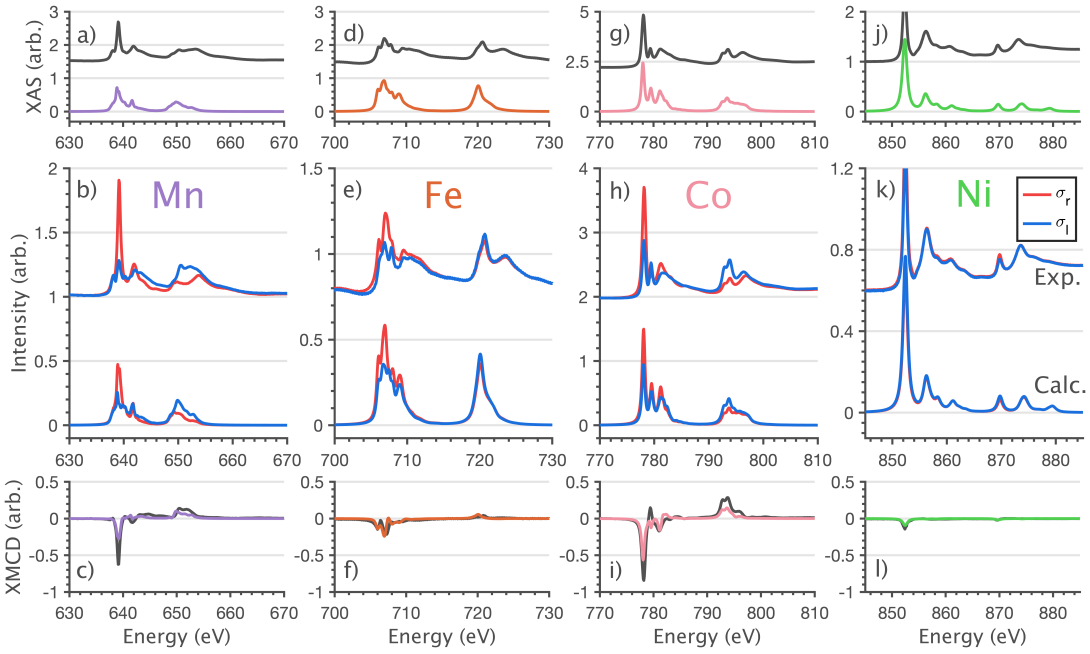

Figure S4: Grazing incidence, k_i 70° c, single crystal $Li_2(Li_{1-x}TM_x)N$ (where TM = Mn, Fe, Co and Ni) XAS (*a, d, g, j*) (σ_h), circular polarisation absorption (*b, e, h, k*) (σ_r and σ_l), and XMCD (*c, f, i, l*) (σ_r - σ_l) spectra of experimental (*black*) and optimised charge-transfer ligand-field multiplet calculations (*colour*) performed at 21 K and 14 T.

S.6 Magnetisation and Zeeman Diagrams

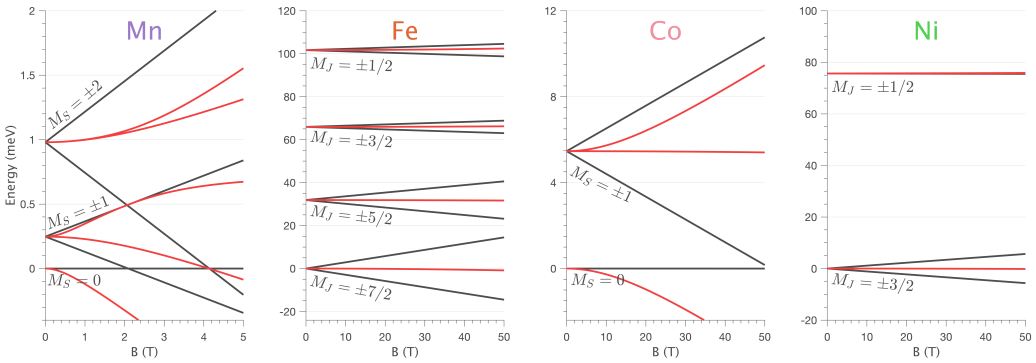

Figure S5: Calculation of Zeeman diagrams for the $Li_2(Li_{1-x}TM_x)N$ series portraying the degeneracy of the ground-state manifolds upon application of a magnetic field. (—) $H \parallel c$ and (—) $H \perp c$. Labelling of ground- and excited-states as defined in Table 1.

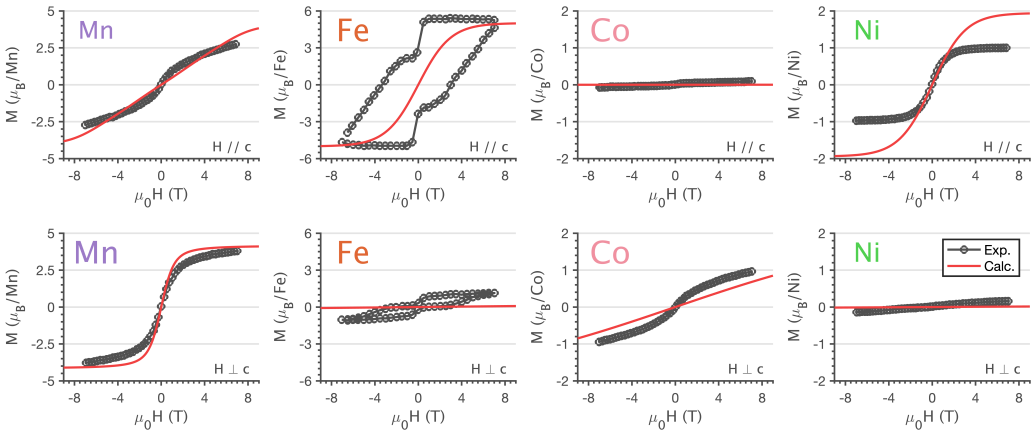

Figure S6: Calculation of representative magnetisation dependencies of $Li_2(Li_{1-x}TM_x)N$ and compared to experimental measurements[4]. (*Top row*) $H \parallel c$ (*Bottom row*) $H \perp c$. Calculated magnetic moments of optimised charge-transfer multiplet calculations scaled through the Landé g-factor.

S.7 Charge-transfer energy differences dependence

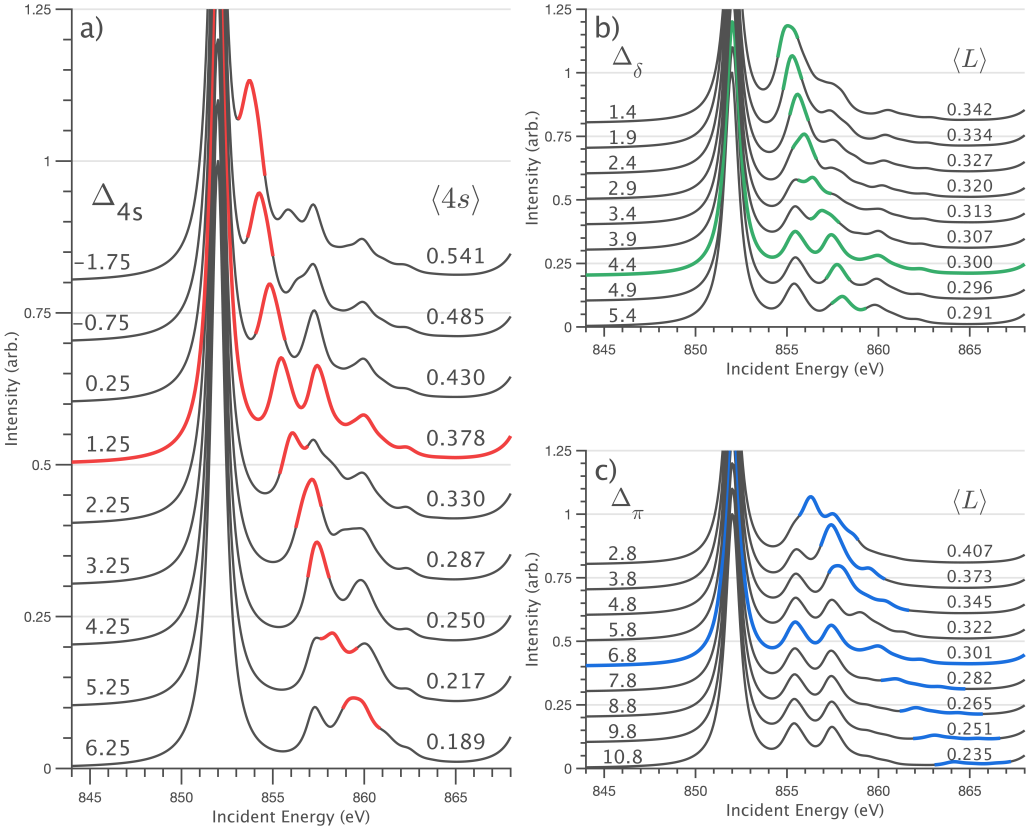

Figure S7: Systematic exploration of the multi-configurational interaction energy difference, Δ dependencies upon normal incidence ($k_i \parallel c$) Ni $L_{2,3}$-edge calculations. Optimised calculations in bold linewidths (Figure 7j). Fixed optimised overlap, V of all calculations (as stated in Table S2) with exploration of (a) $\left|3d^8 4s\right\rangle$, (b) $\left|3d^8 L_{\delta}^{-}\right\rangle$ and (c) $\left|3d^8 L_{\pi}^{-}\right\rangle$ configuration interactions investigated with calculated expectation values of the metal $4s$ or ligand orbitals.

Chapter 4

Direct access to $3d$-$4s$ orbital excitations and single-ion magnetisation dynamics with high-energy resolution RIXS

Direct measurement of single-ion magnetic anisotropy has yet to be achieved by RIXS, and with $Li_2(Li_{1-x}Fe_x)N$ exhibiting an energy barrier approaching the spectral resolution limit of the I21 emission spectrometer, pursuit of single-ion magnetisation dynamics was proposed to be undertaken. While magnetic dynamics could not be experimentally resolved, low energy $3d$-$4s$ excitations were discovered. These $2p3d$ Fe L_3-edge results provide the first evidence of bands of $2p \rightarrow 3d_{z^2}4s$ hybridised excitations observed through this technique with magnetisation dynamics approaching the limit of being resolved. These results were verified through multiplet and *ab initio* calculations. Upon the formation of an accurate multiplet description of $Li_2(Li_{1-x}Fe_x)N$ the study also identifies a characteristic q-dependence in zero-field splitting excitations. The q-dependence differ for $\Delta M_J \pm 7/2 \rightarrow \pm 5/2$ versus $\pm 7/2 \rightarrow \pm 3/2$ and are further proposed as a means to accurately probe the structure of eigenstates that define SIM magnetisation dynamics.

Direct access to $3d$-$4s$ orbital excitations and single-ion magnetisation dynamics with high-energy resolution RIXS

Myron S. Huzan[1,2], Manuel Fix[3], Abhishek Nag[4], Mirian Garcia-Fernandez[4], Andrew C. Walters[4], Ke-Jin Zhou[4], Anton Jesche[3], Michael L. Baker[1,2*]

[1] *The School of Chemistry, The University of Manchester, M13 9PL, Manchester, UK*

[2] *The University of Manchester at Harwell, Diamond Light Source, Harwell Campus, OX11 0DE, UK*

[3] *EP VI, Center for Electronic Correlations and Magnetism, Institute of Physics, University of Augsburg, D-86159 Augsburg, Germany*

[4] *Diamond Light Source, Harwell Science and Innovation Campus, Chilton, Didcot, OX11 0DE, UK*

(Dated: October 12, 2022)

Single-ion magnets (SIMs) exhibit bi-stability of magnetisation due to an effective anisotropic barrier to the reversal of their magnetic moment, giving rise to a magnetic coercivity below a blocking temperature. Linearly coordinated transition metal complexes have gained significant interest in displaying giant magnetic anisotropy barriers due to first order spin-orbit coupled ground states resulting from pronounced $3d_{z^2}$-$4s$ orbital hybridisation. This study reports the quantification of the first single crystal, monovalent Fe L_3-edge RIXS measurements on an exceptional SIM, $Li_2(Li_{1-x}Fe_x)N$. The measurements enable direct measurement of $3d_{z^2}$-$4s$ spin excitations, present due to the admixture of Fe $3d_{z^2}$ character into unoccupied Fe $4s$ orbitals. The observed excitations are analysed using multiplet theory with inclusion of $3d_{z^2}$-$4s$ orbital hybridisation via a single impurity Anderson model. Additionally, it is revealed how $2p3d$ RIXS can be applied to directly probe single-ion magnetisation dynamics. It is shown that momentum transfer dependence of these excitations are sensitive to the structure of eigenstates that define SIM magnetisation dynamics.

I. INTRODUCTION

As advancements in the chemical synthesis of molecular systems drive towards ever increasingly sophisticated electronic and magnetic properties, there exists a necessity for experimental quantification to keep step; the application of $2p3d$ L_3-edge RIXS exists at this forefront as a compelling technique to comprehensively quantify the electronic structure and magnetism of nanoscale structures.

Fe dopants within $Li_2(Li_{1-x}Fe_x)N$ are linearly coordinated, monovalent ($3d^7$) sites which exist as one of a growing number of low coordinate transition metal (TM) complexes which exhibit exceptional bi-stability of magnetism and magnetic remanence with a prospective application as a rare-earth alternative —. Furthermore, at low Fe doping concentrations $Li_2(Li_{1-x}Fe_x)N$ has been shown to act as a single ion magnet (SIM) with potential applications in domains including nanoscale information storage [1], quantum computation [2] and magnetic field sensing [3]. Fe doped lithium nitride exhibits amongst the largest barrier to magnetisation reversal largest of any TM-SIM, U_{eff} = 34.8±3.31 meV [4–6] and magnetic relaxation times approaching those of the highest performing Ln-SIMs, with τ being of the order of $\sim 10^4$ s [5]. The extended solid-state system of Li_3N as a dopant matrix achieves remarkable alternating magnetic anisotropic properties for a series of monovalent TM ions, Mn through to Ni [7, 8]. It provides an alternative approach to maximising SIM properties [9] currently steered by coordination chemistry approaches.

Symmetry permitted mixing of the ds-orbitals facilitates the reordering of the $3d$ ligand field, resulting in first-order spin-orbit coupling that approaches the atomic limit of various TM ions [10–12]. The influence of ds mixing on electronic structure has relied predominantly on theoretical approaches. There currently exists limited experimental methods shown to exhibit a direct sensitivity to ds mixing. Previous X-ray spectroscopic investigations of the dopant $Li_2(Li_{1-x}TM_x)N$ system, where TM = Mn through to Cu, provided substantial evidence of significant orbital and ligand hybridisation [8]. However, it was shown that the presence of multiplet excitations for Fe(I), $3d^7$ mask spectral features relating to ds mixing. Thus, this study turns to the high-resolution $2p3d$ RIXS to identify the methods sensitivity to ds mixing and quantify these effect in $Li_2(Li_{1-x}Fe_x)N$.

This letter presents a comprehensive quantification of single crystal L_3-edge $2p3d$ RIXS of $Li_2(Li_{1-x}Fe_x)N$, providing the first experimental evidence of low-lying $3d_{z^2}$-$4s$ excitations through this technique. An Anderson impurity model is applied to interpret and reproduce the experimental measurements. This study further highlights the capacity $2p3d$ RIXS and multiplet calculations in unravelling sophisticated orbital hybridisations. RIXS is shown to provide unprecedented insight into sd hybridisation, which can undoubtedly be further employed for a myriad of current and future molecular systems.

II. EXPERIMENTAL SECTION
L_3-EDGE RIXS MEASUREMENTS

High energy resolution Fe L_3-edge $2p3d$ resonant inelastic X-ray scattering (RIXS) measurements were per-

* michael.baker@manchester.ac.uk

formed on the I21-RIXS spectrometer at Diamond Light Source, UK [13]. Single crystals of $Li_2(Li_{1-x}Fe_x)N$ were prepared as previously reported [14] to a nominal concentration of $x = 0.01$. $Li_2(Li_{1-x}Fe_x)N$ crystallises as a hexagonal lattice of Li_2N layers alternating with $Li_{1-x}Fe_x$ planes perpendicular to the crystallographic c axis. Dopant Fe site substitution replaces a Li-1b Wyckoff position ion, Figure 1c. Single crystals were mounted stipulating crystallographic c axis (magnetic easy-axis) to be oriented parallel k_i within an Argon atmosphere with Torr Seal onto a copper sample holder. Cleaving posts were mounted and removed within an ultra-high vacuum ($< 10^{-8}$ mbar), revealing a fresh surface. Oxygen K-edge X-ray absorption measurements confirmed no surface oxidation. Measurements were performed with linear horizontal (σ) polarisation. Linear vertical (π) polarisation confirmed as rotational invariant with respect to k_i incidences. RIXS measurements were conducted for incident energies ranging from 709 - 715 eV in steps of 200 meV with energy transfer ranging from -0.5 to 6 eV in 6.5 meV step sizes. Measurements were performed at 11 K and 300 K with a fixed 2θ scattering angle of 150°. Normal ($k_i \parallel c$) and grazing (k_i 70°c) incidences relative to the surface normal of the crystals were performed, Figure 1e. Energy calibration was conducted with respect to elastic scattering from a carbon tape reference. Fine energy adjustments through Gaussian fitting were performed within DAWN [15]. RIXS simulations performed include charge-transfer ligand-field multiplet and CASSCF calculations. Complete descriptions of the computational details are provided within the Supplementary Information.

III. RESULTS AND DISCUSSION

Figure 1a compares the Fe L_3-edge total-fluorescence yield detected X-ray absorption spectroscopy (XAS) spectra with the integrated energy transfer Fe L_3-edge RIXS. $2p3d$ RIXS provides access to dd and charge-transfer excitations through dipole allowed transitions [16] ($2p^63d^n \rightarrow 2p^53d^{n+1}$ excitation, $2p^53d^{n+1} \rightarrow 2p^63d^n$ relaxation) and Figure 1b shows the measured L_3-edge RIXS surface plot of $Li_2(Li_{1-x}Fe_x)N$ at 11 K and normal incidence, $k_i \parallel c$. The RIXS maps clearly shows how spectral contributions can be observed that are inaccessible with L_3-edge XAS.

$Li_2(Li_{1-x}Fe_x)N$ exhibits extremely rich spectral features over the L_3-edge extending up to 3.5 eV energy transfer. Previous studies of $3d^7$ ions (Co(II)) L_3-edge RIXS indicate that ligand field multiplet excitations exist at an energy transfer of approximately 0-2 eV [17], and charge-transfer excitations to energies in excess of 2.5 eV [18, 19]. As demonstrated by Hunault *et al.* [20], ligand field diagrams provide a useful insight for the interpretation of RIXS, enabling the quantification of ligand-field multiplet excitations. Figure 2 presents a series of ligand-field diagrams where the effects of ligand-field strength and electron-electron repulsion are systematically varied within a reasonable range. Ligand field diagrams are shown with comparison to the integrated incident energy Fe L_3-edge RIXS, Figure 2e. The magnitude and sign of ligand field parameters Dt and Ds dictate the orbital degeneracy and energy splittings of the $3d$-orbitals within a $D_{\infty h}$ point-group symmetry. The sign of Dt is required to be positive for the system to exhibit the previously established Fe(I) ^{4}E ground-state for $Li_2(Li_{1-x}Fe_x)N$ [6]. The sensitivity of Ds and Racah B and C facilitates tuning of multiplet effects. Ligand-field multiplet theory was previously applied to simulate the fluorescence detected $L_{2,3}$-edge X-ray absorption spectra of $Li_2(Li_{1-x}Fe_x)N$ [6]. The ligand-field splitting and Racah parameters obtained, (vertical dashed lines of Figure 2) identified the ground-state (^{4}E) is energetically well-isolated from excited states, Figure 2. Spin-orbit coupling is excluded from the ligand-field diagrams for clarity. The effect of which is shown in the integrated simulation of the RIXS, where a subtle but significant difference is observed, Figure 2e. The sensitivity to spin-orbit coupling originates from thermal de-population of the four Kramers doublets ($^4D_{7/2}$), with increased spin-orbit coupling. Thus, an accurate Boltzmann thermal population of a first-order spin-orbit coupled ground-state and fine structure features at 11 K is required. The ligand-field diagrams show that the experimentally observed 0.25 eV excitation cannot be accounted for with ligand field theory since it is too high in energy to originate from spin-orbit coupling and too low in energy to manifest from excitations of ligand-field multiplets.

Previous studies of $Li_2(Li_{1-x}TM_x)N$, through X-ray absorption spectroscopy and X-ray magnetic circular dichroism, developed knowledge and trends of orbital hybridisation within this series [8]. Results indicated that $L_{2,3}$-edge X-ray absorption spectroscopy has a sensitivity to $3d$-$4s$ orbital hybridisation. However, for $Li_2(Li_{1-x}Fe_x)N$ $3d$-$4s$ satellites count not be identified due to overlapping multiplet excitations Huzan *et al.*. It is therefore proposed that the uncharacterised low energy excitation at 0.25 eV is a $3d$ intensity enhanced $4s$ excitation. To test this theory we construct and investigate a three configuration interaction $|\psi_i\rangle = \alpha\left|3d^7\right\rangle + \beta\left|3d^64s\right\rangle + \gamma\left|3d^6L^-\right\rangle$ with prefactor coefficients, ($\alpha^2 + \beta^2 + \gamma^2 = 1$) as described through charge transfer ligand field multiplet principles [21] to comprehensively evaluate if the 0.25 eV excitation is consistent with being assigned as a $3d_{z^2}$ enhanced $4s$ excitation (full description provided within the Supplementary Information). Figure 3a and b show energy level dependencies of pure $3d$ and hybridised $3d_{z^2}4s$ excitations respectively. Through tuning of $3d$-$4s$ orbital overlap, V_{4s} and corresponding energy separation, Δ_{4s}a low-lying band of hybridised $3d_{z^2}4s$ sextet excitations is found consistent with the experimentally measured 0.25 eV excitation. This excitation is composed of two sets of dominant excited-states that are not fully resolved experimentally; an orbitally quenched $S = 5/2$ and orbitally unquenched ($S = 5/2$,

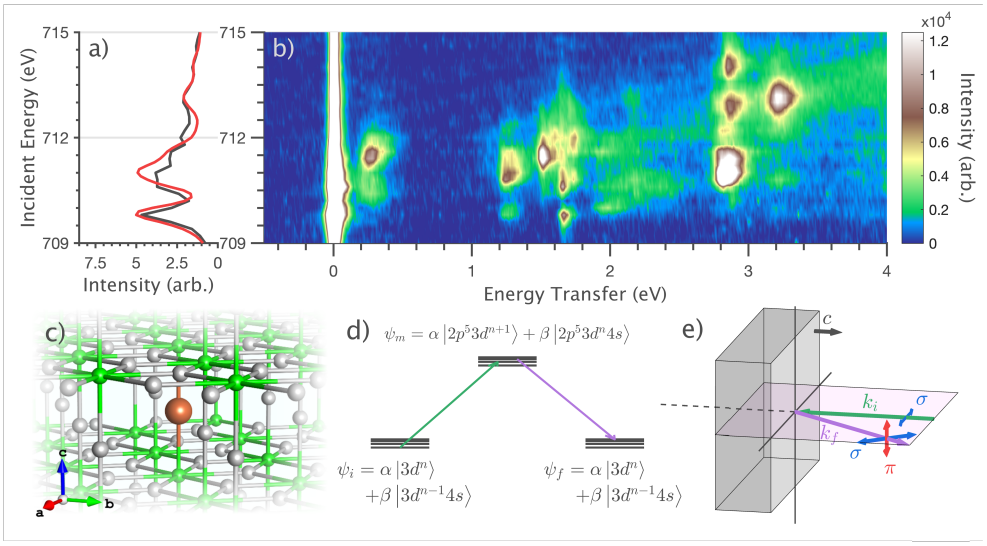

FIG. 1. *a*) Comparison of L_3-edge integrated energy transfer RIXS (black) and previously measured $Li_2(Li_{1-x}Fe_x)N$ FY-XAS (red) [Ref]. *b*) Fe L_3-edge RIXS map of $Li_2(Li_{1-x}Fe_x)N$ with incident X-ray vector, $k_i \parallel c$ performed at 11 K with a nominal concentration of 1%. *c*) Extended solid-state view of $Li_2(Li_{1-x}Fe_x)N$ illustrating Fe dopant substitution with an α-Li3N matrix at the 1**b** Wyckoff position. *d*) Schematic of the 2-step scattering processes of 2p3d RIXS, illustrating the incident ($\rightarrow$), and emission ($\rightarrow$) energies with corresponding ground (ψ_i), intermediate (ψ_m), and final (ψ_f) state wavefunctions of a hybridised 3*d*-4*s* system. $\alpha^2 + \beta^2 = 1$ and defined through a charge transfer ligand field multiplet description within the Supplementary Information. *e*) Sketch of the normal incidence ($k_i \parallel c$) experimental geometry with incident (k_i) and emission (k_f) vectors and corresponding linear horizontal (σ) and vertical (π) polarisations.

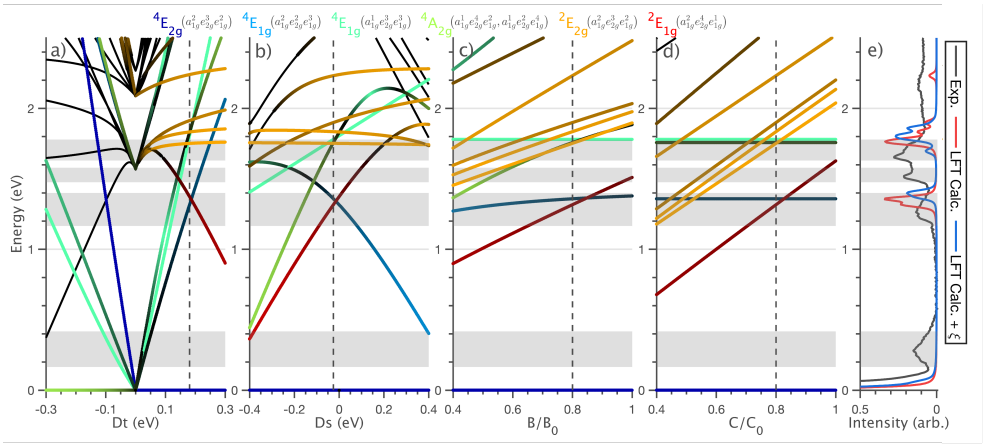

FIG. 2. Energy level dependencies of ligand field theory deduced Fe(I) as a function of crystal field parameters Dt (*a*), Ds (*b*) and Racah parameters B (*c*) and C (*d*) of $D_{\infty h}$ symmetry. Colour labelling to spectroscopic term symbols with representative colour gradient indicative of relative expected *d*-orbital occupation (Darker gradients representative of electron occupations fractionally disparate from assumed spectroscopic term symbol). *e*) Comparison of experimental to calculated Fe L_3-edge integrated incident energy RIXS isolating excitation features to energy level diagrams, performed at 11 K and $k_i \parallel c$. Dashed vertical lines represent previously deduced ligand field parameters of $Li_2(Li_{1-x}Fe_x)N$ from X-ray absorption measurements [Ref Huzan].

$L = 2$) $J = 9/2$ states. Further, 3*d*-4*s* excitations at higher energy consist of quartet and doublet spin states which nestle within the *dd* excitations. Figure 3c compares integrated incident energy Fe L_3-edge RIXS of the optimised Anderson impurity model to experiment.

Figure 4 compares optimised charge-transfer ligand field multiplet calculations with experimentally measured Fe L_3-edge RIXS. This model replicates the rich spectral features observed. Further comparisons of theory to ex-

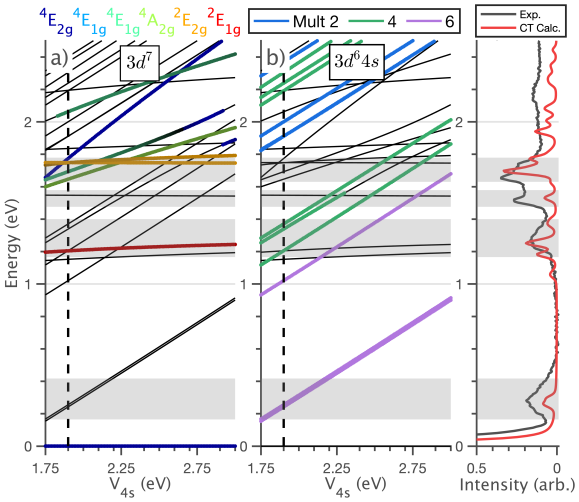

FIG. 3. Energy level dependencies of charge transfer ligand field multiplet modelled $Li_2(Li_{1-x}Fe_x)N$ as a function of $3d$-$4s$ orbital overlap, V_{4s}. Spectroscopic term symbol labelling of $3d^7$ states consistent with Figure 2 and *b*) isolation of excited-state $3d^6 4s$ character with corresponding atomic multiplicity. *c*) Comparison of experimental to optimised charge-transfer multiplet deduced Fe(I) of integrated incident energy Fe-L_3 RIXS.

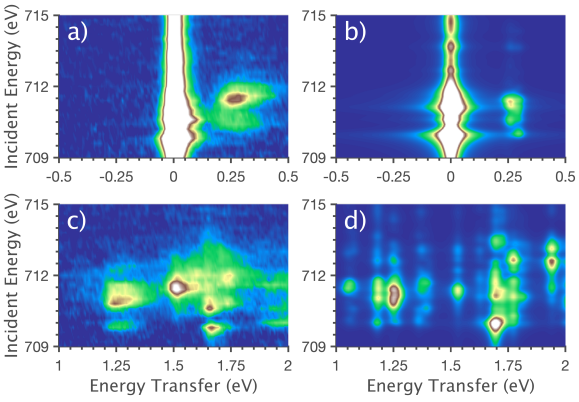

FIG. 4. Fe L_3-edge RIXS contour plots of $Li_2(Li_{1-x}Fe_x)N$ with incident X-ray vector, $k_i \parallel c$, performed at 11 K, with a nominal concentration of 1%. Comparison of experimental (a, c) to simulated (b, d) highlighting the low energy (a, b) and respective *dd* multiplet excitations (c, d).

perimental measurements are supplied within the supplementary information, demonstrating the model's success in also reproducing grazing incidence and 300 K measurements.

A. Experimentally approaching measurement of magnetic anisotropy

Direct measurement of TM single ion magnetisation dynamics *via* RIXS are yet to be reported. However, as complexes with increasingly large magnetic anisotropy barriers are synthesised, coupled with the increasing experimental resolution at fourth-generation synchrotrons [13], this breakthrough is within reach. For $Li_2(Li_{1-x}Fe_x)N$ the $^4D_{7/2}$ ground-state splits into four doublets, $M_J = \pm 7/2, \pm 5/2, \pm 3/2$ and $\pm 1/2$ manifesting from an unquenched first-order spin-orbit coupled ground-state, Figure 5a. Previous [22], (and current) *ab initio* and charge-transfer multiplet calculations, in combination with experimentally determined magnetic relaxation [4, 5] and temperature-dependent X-ray absorption measurements [6] predict the first spin-orbit coupling excited state ($M_J = \pm 5/2$) at 34.8±3.31 meV; a value approaching the experimental resolution of I21 [13]. While direct experimental quantification of these excitations were not conclusively observed (Figure 5c), Figures 5d and e present charge-transfer ligand-field multiplet and CASSCF results of RIXS contour plots with significantly reduced line width. The simulated RIXS maps show two spin-orbit coupled excitations within the ground-state manifold, Peak I ($M_J = \pm 7/2 \rightarrow \pm 5/2$) and Peak II ($M_J = \pm 7/2 \rightarrow \pm 3/2$). These calculations predict the evidence of RIXS transition selection rules extending to $\Delta M_J = \pm 2$ for a TM ion within a single-ion magnet with signs of experimentally measuring these excitations being within reach. Furthermore, exploring momentum transfer dependencies (q) of these excited state features, Peak I and II, Figure 5b show that they have opposing q dependence.

IV. CONCLUSIONS

High-resolution Fe L_3 RIXS identifies the presence of a low-lying band of $3d_{z^2}$-$4s$ excitations present due to significant *ds*-orbital hybridisation within $Li_2(Li_{1-x}Fe_x)N$. The orbital hybridisation is correlated to facilitating first-order spin-orbit coupling of the monovalent Fe ion, driving its high-performance magnetic properties. Quantification through charge-transfer ligand field multiplet calculations provides experimental verification of these excitations, which were previously limited to theoretical techniques.

Energy barriers to magnetisation reversal within high-performance SIMs are within reach and are approaching the experimental resolution of the new generation of RIXS spectrometers; previously only accessible with inelastic neutron scattering measurements [23]. Further experimental advantages of RIXS to that of INS extends to the accessibility of spin selection rules extending to $\Delta M_J = \pm 1, \pm 2$ for a first-order spin-orbit coupled ground-state [24–26]. Predicted for $Li_2(Li_{1-x}Fe_x)N$ is a q-dependence of these excitations opens additional exper-

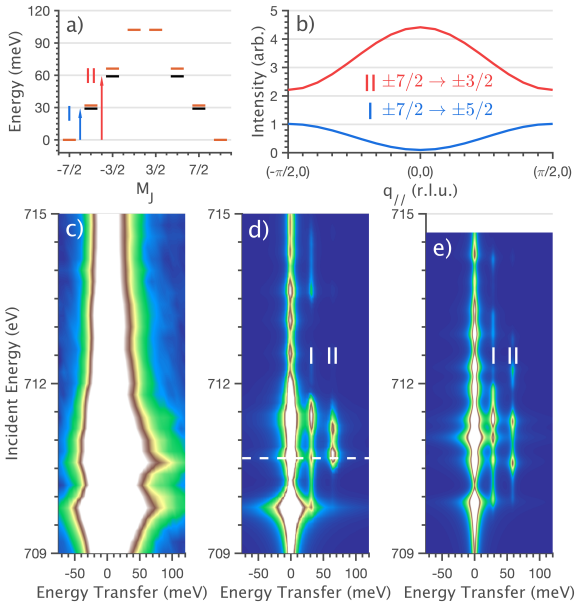

FIG. 5. *a*) Calculated M_J splitting of the ground-state $J = 7/2$ manifold from charge transfer ligand field multiplet (—) and CASSCF (—) calculations. *b*) Momentum transfer dependence of anisotropic excitations with $q \parallel c$ rotating through to the crystallographic *a*-*b* plane. A dashed horizontal line within *d* represents the selected incident energy of the explored excited M_J state momentum transfer dependencies. Comparison of anisotropic limit of experimental (*c*), charge transfer ligand field multiplet (*d*) and CASSCF (*e*) calculations. Labelling of Peak I and II corresponding to excitation of ground-state $M_J = \pm7/2$ to $\pm5/2$ and $\pm3/2$ respectively.

imental avenues to pursue the identification of ground- and excited-state eigenfunctions, which define magnetisation dynamics.

ACKNOWLEDGMENTS

We acknowledge Diamond Light Source for experimental time for the following proposals; SP18489-1 and MM21595-1 at I21. This work was supported by the Deutsche Forschungsgemeinschaft (DFG, German Research Foundation) - Grant No. JE748/1. MLB acknowledges the support of the Royal Society of Chemistry. Nikolay A. Bogdanov is thanked for providing preliminary CASSCF calculations. David Collison is gratefully acknowledged for stimulating discussions and comments.

[1] M. Mannini, F. Pineider, C. Danieli, F. Totti, L. Sorace, P. Sainctavit, M. A. Arrio, E. Otero, L. Joly, J. C. Cezar, A. Cornia, and R. Sessoli, Nature **468**, 417 (2010).
[2] A. Gaita-Ariño, F. Luis, S. Hill, and E. Coronado, Molecular spins for quantum computation (2019).
[3] M. N. Leuenberger and E. R. Mucciolo, Physical Review Letters **97**, 126601 (2006).
[4] A. Jesche, R. W. McCallum, S. Thimmaiah, J. L. Jacobs, V. Taufour, A. Kreyssig, R. S. Houk, S. L. Bud'Ko, and P. C. Canfield, Nature Communications **5**, 3333 (2014), arXiv:arXiv:1402.6626v1.
[5] M. Fix, J. H. Atkinson, P. C. Canfield, E. Del Barco, and A. Jesche, Physical Review Letters **120**, 147202 (2018), arXiv:1803.04867.
[6] M. S. Huzan, M. Fix, M. Aramini, P. Bencok, J. F. W. Mosselmans, S. Hayama, F. A. Breitner, L. B. Gee, C. J. Titus, M. A. Arrio, A. Jesche, and M. L. Baker, Chemical Science **11**, 11801 (2020).
[7] A. Jesche, L. Ke, J. L. Jacobs, B. Harmon, R. S. Houk, and P. C. Canfield, Physical Review B - Condensed Matter and Materials Physics **91**, 180403 (2015).
[8] M. S. Huzan, T. G. Burrow, M. Fix, P. Bencok, M. Aramini, A. Jesche, and M. L. Baker, Unpublished.
[9] M. A. Zykin, P. E. Kazin, and M. Jansen, Chemistry - A European Journal **26**, 8834 (2020).
[10] J. M. Zadrozny, D. J. Xiao, M. Atanasov, G. J. Long, F. Grandjean, F. Neese, and J. R. Long, Nature Chemistry **5**, 577 (2013).
[11] I. G. Rau, S. Baumann, S. Rusponi, F. Donati, S. Stepanow, L. Gragnaniello, J. Dreiser, C. Piamonteze, F. Nolting, S. Gangopadhyay, O. R. Albertini, R. M. Macfarlane, C. P. Lutz, B. A. Jones, P. Gambardella, A. J. Heinrich, and H. Brune, Science **344**, 988 (2014).
[12] P. C. Bunting, M. Atanasov, E. Damgaard-Møller, M. Perfetti, I. Crassee, M. Orlita, J. Overgaard, J. Van Slageren, F. Neese, and J. R. Long, Science **362**, 7319 (2018).
[13] K.-J. Zhou, A. Walters, M. Garcia-Fernandez, T. Rice, M. Hand, A. Nag, J. Li, S. Agrestini, P. Garland, H. Wang, S. Alcock, I. Nistea, B. Nutter, N. Rubies, G. Knap, M. Gaughran, F. Yuan, P. Chang, J. Emmins, and G. Howell, J. Synchrotron Rad **29**, 563 (2022).
[14] A. Jesche and P. C. Canfield, Philosophical Magazine **94**, 2372 (2014), arXiv:1402.6004.

[15] M. Basham, J. Filik, M. T. Wharmby, P. C. Chang, B. El Kassaby, M. Gerring, J. Aishima, K. Levik, B. C. Pulford, I. Sikharulidze, D. Sneddon, M. Webber, S. S. Dhesi, F. Maccherozzi, O. Svensson, S. Brockhauser, G. Náray, and A. W. Ashton, Journal of Synchrotron Radiation **22**, 853 (2015).

[16] L. J. Ament, M. Van Veenendaal, T. P. Devereaux, J. P. Hill, and J. Van Den Brink, Reviews of Modern Physics **83**, 705 (2011), arXiv:1009.3630.

[17] R.-P. Wang, M.-J. Huang, A. Hariki, J. Okamoto, H.-Y. Huang, A. Singh, D.-J. Huang, P. Nagel, S. Schuppler, T. Haarman, B. Liu, and F. M. F. de Groot, The Journal of Physical Chemistry C 10.1021/ACS.JPCC.2C01521 (2022).

[18] B. Liu, M. M. Van Schooneveld, Y.-T. Cui, J. Miyawaki, Y. Harada, T. O. Eschemann, K. P. De Jong, M. U. Delgado-Jaime, and F. M. F. De Groot, J. Phys. Chem. C , 17450 (2017).

[19] B. Liu, E. N. Glass, R.-P. Wang, Y.-T. Cui, Y. Harada, D.-J. Huang, S. Schuppler, C. L. Hill, and F. M. F. De Groot, Physical Chemistry Chemical Physics 10.1039/c7cp06786k (2018).

[20] M. O. Hunault, Y. Harada, J. Miyawaki, J. Wang, A. Meijerink, F. M. De Groot, and M. M. Van Schooneveld, Journal of Physical Chemistry A **122**, 4399 (2018).

[21] M. W. Haverkort, M. Zwierzycki, and O. K. Andersen, Physical Review B - Condensed Matter and Materials Physics **85**, 165113 (2012), arXiv:1111.4940.

[22] L. Xu, Z. Zangeneh, R. Yadav, S. Avdoshenko, J. Van Den Brink, A. Jesche, and L. Hozoi, Nanoscale **9**, 10596 (2017).

[23] M. L. Baker, S. J. Blundell, N. Domingo, and S. Hill, Spectroscopy Methods for Molecular Nanomagnets (2015).

[24] M. W. Haverkort, Physical Review Letters **105**, 10.1103/PhysRevLett.105.167404 (2010), arXiv:0911.0706.

[25] G. Ghiringhelli, A. Piazzalunga, C. Dallera, T. Schmitt, V. N. Strocov, J. Schlappa, L. Patthey, X. Wang, H. Berger, and M. Grioni, Physical Review Letters **102**, 10.1103/PHYSREVLETT.102.027401 (2009).

[26] A. Nag, H. C. Robarts, F. Wenzel, J. Li, H. Elnaggar, R. P. Wang, A. C. Walters, M. García-Fernández, F. M. De Groot, M. W. Haverkort, and K. J. Zhou, Physical Review Letters **124**, 10.1103/PhysRevLett.124.067202 (2020).

Electronic Supplementary Information:

Direct access to 3*d*-4*s* orbital excitations and single-ion magnetisation dynamics with high-energy resolution RIXS

Myron S. Huzan,[a] [b] Manuel Fix,[c] Abhishek Nag,[d] Mirian Garcia-Fernandez,[d] Andrew C. Walters,[d] Ke-Jin Zhou,[d] Anton Jesche,[c] Michael L. Baker[a] [b]

[a] *Department of Chemistry, The University of Manchester, Manchester, M13 9PL, UK*

[b] *The University of Manchester at Harwell, Diamond Light Source, Harwell Campus, OX11 0DE, UK*

[c] *EP VI, Center for Electronic Correlations and Magnetism, Institute of Physics, University of Augsburg, D-86159 Augsburg, Germany*

[d] *Diamond Light Source, Harwell Science and Innovation Campus, Chilton, Didcot, OX11 0DE, UK*

Contents

S.1 Computational Details

Charge-transfer (Anderson impurity) ligand-field multiplet calculations of the Fe L_3-edge RIXS results were performed using the quantum many-body scripting language, Quanty[1]. Input files for the simulation of RIXS were adapted from templates generated in Crispy[2]. Atomic multiplet effects are described through Slater-Condon-Shortley integrals, F^k_{pp}, F^k_{pd} (Coulomb) and G^k_{pd} (exchange); an 80% reduction is applied to the Hartree-Fock calculations resulting from the overestimation of electron-electron repulsion found for the free ion. Relativistic effects resulting from $3d$ spin-orbit coupling were previously determined through temperature-dependent X-ray absorption spectroscopy measurements[3], resulting in $\xi_{3d} = 0.052$ and $0.068\,\text{eV}$ for the initial and intermediate states respectively. Li_3N exhibits a D_{6h} point group symmetry resulting in a ligand field model characterising the orbital degeneracy through Dq, Ds and Dt parameters. The local linear symmetry of the Fe atom is characterised by a $D_{\infty h}$ point group and has an equivalence with D_{6h} when $Dq = 0$. This stipulates a d-orbital degeneracy and energy splittings of an $A_{1g}(d_{z^2})$ singlet, and two E doublets, $E_{1g}(d_{xy}, d_{yz})$ and $E_{2g}(d_{x^2-y^2}, d_{xy})$. Orbital covalency as previously deduced for this series of linear transition metal dopants of $Li_2(Li_{1-x}TM_x)N$ (where TM = Mn through to Cu) characterises an appreciable π-bonding donation mixing the degenerate $E_{1g}(d_{xy}$,$d_{yz})$ orbitals into unoccupied N $2p$. The magnitude of hybridisation is quantified through an energy separation, $\Delta_{E_{1g}}$ and covalency overlap, $V_{E_{1g}}$ of the $3d$ and ligand states. $4s$ hybridisation within linear TM complexes is known to destabilise σ-donation $3d\sigma$ orbital character and reduce the $3d_{z^2}$ orbital energy. The strength of ds orbital hybridisation is introduced through an energy separation Δ_{4s}, orbital overlap parameter V_{4s}. Additionally, further exchange Slater-Condon-Shortley integrals are included in the ground, G^2_{ds} and excited states, G^1_{ps}, G^2_{ds}. Multiplet calculations of ground and excited state configurations are considered as a linear combination of $\left|3d^7\right\rangle, \left|3d^6 4s\right\rangle$ and $\left|3d^6 L^-\right\rangle$, where L^- represents an additional ligand electron of metal character (metal-ligand charge transfer, MLCT). Gaussian broadening due to instrumental resolution was fixed at 25 meV full-width half-maximum (FWHM), calculated from the fitting of the elastic line of scattering off carbon tape. Core-hole lifetime broadenings of intermediate and final states was applied through a Lorentzian convolution of $\Gamma_i = 350\,\text{meV}$ and $\Gamma_t = 20\,\text{meV}$ FWHM over the incident and transfer energy domains respectively. Transfer energy resolution is applied to match spectral features of the experimental data. RIXS spectra were collected without polarisation analysis, stipulating the

calculated scattered photon transitions to include contributions of both σ and π.

Table S1: Ground (GS, $3d^n$) and excited-state (ES, $2p^5 3d^{n-1}$) charge transfer multiplet parameters of optimised $Li_2(Li_{1-x}Fe_x)N$ L_3-edge RIXS calculations; all values in eV.

	GS	ES
F^2_{dd}	7.8088	8.4976
F^4_{dd}	4.8136	5.2472
F^2_{pd}		4.9136
G^1_{pd}		3.5704
G^3_{pd}		2.0296
G^2_{ds}	0.9768	0.8569
G^1_{ps}		0.1440
ξ_{2p}		8.530
ξ_{3d}	0.052	0.068
Ds	-0.230	-0.230
Dt	0.174	0.174
Δ_{4s}	0.65	0.65
V_{4s}	1.90	1.90
Δ_L	3.10	4.10
V_L	1.00	1.00

S.2 Fe L_3-edge Temperature and Angular dependence RIXS

$Li_2(Li_{1-x}Fe_x)N$ is known to exhibit significant angular and temperature dependencies of spectral features through previous $L_{2,3}$-edge X-ray absorption and X-ray magnetic circular dichroism studies[3]. Figure S1a and S2a present grazing and room-temperature (nominal concentration of $x = 0.1$) L_3-RIXS contour plots with further comparison of the optimised charge-transfer multiplet calculations within these experimental conditions. As within the main body of this publication, the calculation replicates the spectral features of these experimental conditions. Comparison plots are further presented to the 11 K normal incidence as difference contour plot, Figure S1d, f (normal, $k_i \parallel c$ - grazing, k_i 70°c incidence) and S2b, d (300 K - 11 K), this highlights the spectral variation RIXS exhibits upon various experimental conditions.

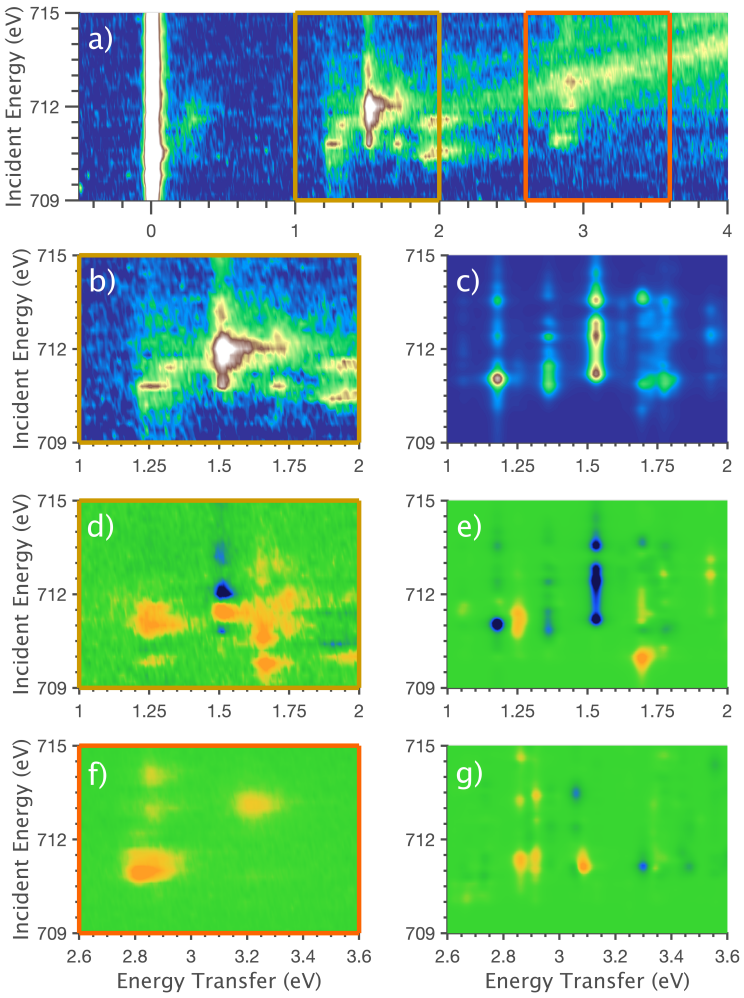

Figure S1: a) Grazing Fe L_3-edge RIXS plane of $Li_2(Li_{1-x}Fe_x)N$ with incident X-ray vector, k_i 70°c performed at 11K with a nominal concentration of 1%. Comparison of experimental (b, d, f) to simulated (c, e, g) RIXS contour plots. Difference contour plots (normal, $k_i \parallel c$ - grazing, k_i 70°c incidence) *dd* multiplet (d, e) and charge transfer (f, g) excitation regions.

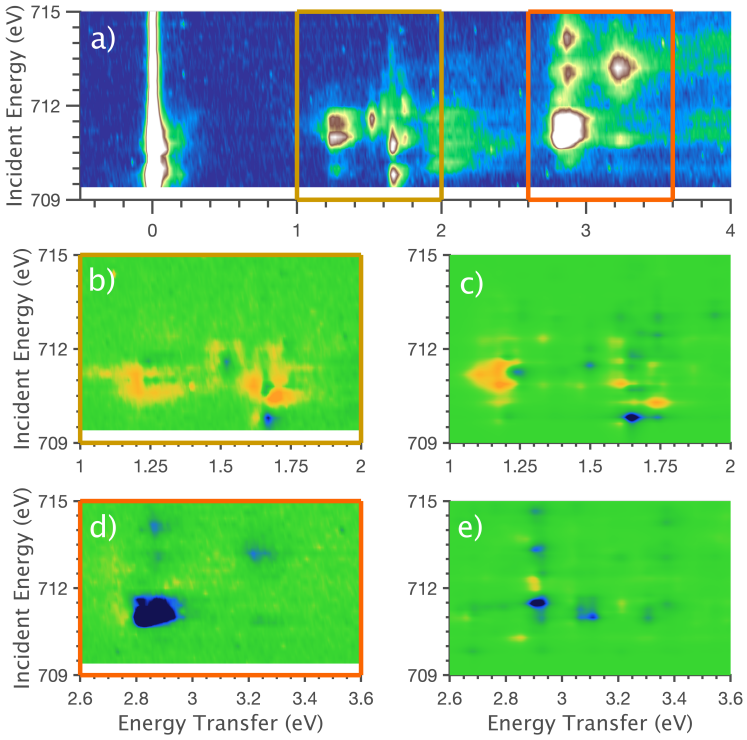

Figure S2: a) Room temperature Fe L_3-edge RIXS plane of $Li_2(Li_{1-x}Fe_x)N$ with incident X-ray vector, $k_i \parallel c$ performed at 300K with a nominal concentration of 10%. Comparison of experimental (b, d) to simulated (c, e) RIXS contour plots. Difference contour plots (300 K - 11 K) *dd* multiplet (b, c) and charge transfer (d, e) excitation regions.

References

[1] M. W. Haverkort, M. Zwierzycki and O. K. Andersen, *Physical Review B - Condensed Matter and Materials Physics*, 2012, **85**, 165113.

[2] M. Retegan, *Crispy: v0.7.3*, 2019.

[3] M. S. Huzan, M. Fix, M. Aramini, P. Bencok, J. F. W. Mosselmans, S. Hayama, F. A. Breitner, L. B. Gee, C. J. Titus, M. A. Arrio, A. Jesche and M. L. Baker, *Chemical Science*, 2020, **11**, 11801–11810.

Chapter 5

Conclusions and Outlook

Since the discovery of Mn_{12} [2], *molecular magnetism* has branched many scientific disciplines exploring all corners of the periodic table. Propelled by the direction of the ever-growing developments within computational quantum chemistry techniques and momentous advancements in chemical synthesis with the field, these collective efforts continue to drive higher the operational temperatures and longer relaxation times of single-ion and molecular magnets.

For several decades, harnessing open-shell single ion systems displaying a bi-stability of magnetism has driven considerable interdisciplinary efforts in the continued pursuit in the miniaturisation of magnetic information storage. $Li_2(Li_{1-x}Fe_x)N$ exists as a novel, solid-state dopant system which facilitates remarkable single-ion properties alternative to the vast majority of efforts steered by coordination chemistry approaches. $Li_2(Li_{1-x}Fe_x)N$ compares favourably to the highest performing transition metal and lanthanide single-ion magnets. The outset of this thesis aimed to quantify the underlying electronic structure contributions to the giant single-ion magnetic anisotropy in $Li_2(Li_{1-x}Fe_x)N$ via a broad range of core-level spectroscopic techniques. Uniquely, this system has demonstrated no signatures of radiolysis through X-ray measurements, facilitating numerous intensive single-crystal spectroscopic studies, ranging from the soft to hard X-ray regimes. As a dopant material, experimental measurements utilising laboratory equipment prohibits accurate quantification. Thus, element sensitivity of synchrotron X-ray radiation techniques are applied to unravel the electronic and magnetic properties. The vast majority of the experimental techniques used within the thesis are seminal to the study of monovalent linear transition metal complexes. The spectra obtained are rich, demonstrating the substantial amount of information that can be deduced. Dopant sites within Li_3N are found to be linearly coordinated with considerable δ and π bonding contributions. This provides a pocket of $D_{\infty h}$ linearity that is proposed to suppress vibronic effects with respect to other linear SIMs. Applications of single-ions exhibiting large magnetic anisotropic has been discussed in great depth through many comprehensive studies [86–88]. However, the

fundamental quantification of these materials and the unravelling of orbital hybridisation is what drove the imminent understanding of $Li_2(Li_{1-x}TM_x)N$; complementary to this is an aspiration to provide insights that inform the synthesis of new SIMs with superior magnetic properties.

This thesis has made extensive use of angular-dependent single-crystal X-ray absorption spectroscopy measurements that enable assignment of orbital transitions, as an extra dimension of quantification where powder measurements would fall short. The versatility that semi-empirical multiplet calculations provide in conjunction with *ab initio* calculations has provided insurmountable evidence of strong orbital hybridisation in $Li_2(Li_{1-x}TM_x)N$, which previously has not been conclusively investigated. Through comprehensive exploration of parameter spaces, a multiplet description of $3d$-$4s$ orbital hybridisation and metal-to-ligand charge-transfer for the $Li_2(Li_{1-x}TM_x)N$ series where TM = Mn, Fe, Co and Ni is provided. Linear transition metal complexes are quickly becoming synonymous with facilitating large magnetic anisotropies resulting from strong $3d$-$4s$ hybridisation. The substantial s-admixture exhibited for the series of TM doped complexes, $Li_2(Li_{1-x}TM_x)N$, is further corroborated through TD-DFT and CASSCF calculations. Periodic trends are explored, and avenues for further scientific directions are opened for the identification and pursuit of alternative solid-state lattice systems.

There exists a symbiotic relationship between theoretical and experimental techniques. As theory advances, there exists a desire for experimental proof. While at the same time, experimental observations of the unknown turn to theory for answers. Like the causality dilemma of the chicken and the egg, the concern is not where it began; instead, the pursuit of answers is what drives the self-perpetuating cycle of science, and this story of TM doped Li_3N does not conclude with the submission of this thesis; instead, it simply opens more doors for further studies.

Comprehension of spin-phonon coupling has widespread implications within *molecular magnetism* and beyond, and the understanding of these modes within a solid-state regime is of great scientific interest [170, 171]. Nuclear resonant vibrational spectroscopy (NRVS) [172, 173] is yet another synchrotron-based spectroscopic technique to be undertaken on $Li_2(Li_{1-x}Fe_x)N$. ^{57}Fe exists as a particularly favourable isotope upon which this vibrational technique can be performed upon. Analogous to Raman spectroscopy, NRVS provides a complete description of the vibrational modes of Mössbauer-active nuclei [174], with the added benefit of revealing both IR and Raman-active modes containing ^{57}Fe-motion [175]. Measurements have already been performed at the ID18 beamline at ESRF, France [176], of several doping con-

centrations, x, in addition to a doubly TM doped system, $Li_2(Li_{1-x-y}Fe_xCu_y)N$. The former aims to investigate the concentration dependencies of vibrational modes, while the latter proposes to investigate the influence of a diamagnetic dopant ion, Cu(I) d^{10} in an attempt to probe the solid-state lattice density dependencies and the prospect of tuning spin-phonon coupling modes through modulation of host lattice density. Interpreting these results will demand sophisticated theoretical methods to understand the spin-phonon coupling modes comprehensively.

To complement the interpretation of spin-phonon coupling within $Li_2(Li_{1-x}Fe_x)N$ the pursuit of electronic structure manifesting from bond-length contraction is proposed to be explored. K-edge X-ray absorption near-edge structure (XANES) measurements performed in Chapter 2 present clear sensitivity to the ligand-field degeneracy of the $4p_{x,y}$ orbitals. Consequently, pressure dependent K-edge XANES measurements were proposed and have been performed at the I20-EDE beamline, Diamond Light Source, UK [177]. Spectroscopic elucidation of N-Fe-N bond length shortening through single crystal and powder diamond anvil cell pressure dependencies and the tracking of energy lowering/raising of the respective $4p$ orbitals was investigated. In light of these prospective results, K-edge X-ray magnetic circular dichroism (XMCD) measurements will hopefully be proposed to correlate to a magnetic interpretation directly.

References

(1) Waldrop, M. M. *Nature* **2016**, *530*, 144–147.

(2) Sessoli, R.; Gatteschi, D.; Caneschi, A.; Novak, M. A. *Nature* **1993**, *365*, 141–143.

(3) Caneschi, A.; Gatteschi, D.; Sessoli, R.; Barra, A. L.; Brunei, L. C.; Guillot, M. *Journal of the American Chemical Society* **1991**, *113*, 5873–5874.

(4) Regnault, N.; Jolicœur, T.; Sessoli, R.; Gatteschi, D.; Verdaguer, M. *Physical Review B - Condensed Matter and Materials Physics* **2002**, *66*, 544091–544095.

(5) Gatteschi, D.; Barra, A. L.; Caneschi, A.; Cornia, A.; Sessoli, R.; Sorace, L. *Coordination Chemistry Reviews* **2006**, *250*, 1514–1529.

(6) Gatteschi, D.; Sessoli, R. Quantum tunneling of magnetization and related phenomena in molecular materials, 2003.

(7) Aromí, G.; Brechin, E. K. *Structure and Bonding* **2006**, *122*, 1–67.

(8) Ako, A. M.; Hewitt, I. J.; Mereacre, V.; Clérac, R.; Wernsdorfer, W.; Anson, C. E.; Powell, A. K. *Angewandte Chemie - International Edition* **2006**, *45*, 4926–4929.

(9) Tanabe, Y.; Kamimura, H. *Journal of the Physical Society of Japan* **1958**, *13*, 539.

(10) Atanasov, M.; Aravena, D.; Suturina, E.; Bill, E.; Maganas, D.; Neese, F. *Coordination Chemistry Reviews* **2015**, *289-290*, 177–214.

(11) Gomez-Coca, S.; Cremades, E.; Aliaga-Alcalde, N.; Ruiz, E. *Journal of the American Chemical Society* **2013**, *135*, 7010–7018.

(12) Shrivastava, K. N. *physica status solidi (b)* **1983**, *117*, 437–458.

(13) Aravena, D.; Ruiz, E. *Dalton Transactions* **2020**, *49*, 9916–9928.

(14) Goodwin, C. A. *Dalton Transactions* **2020**, *49*, 14320–14337.

(15) Reta, D.; Kragskow, J. G.; Chilton, N. F. *Journal of the American Chemical Society* **2021**, *143*, 5943–5950.

(16) Pedersen, K. S.; Dreiser, J.; Weihe, H.; Sibille, R.; Johannesen, H. V.; Sørensen, M. A.; Nielsen, B. E.; Sigrist, M.; Mutka, H.; Rols, S.; Bendix, J.; Piligkos, S. *Inorganic Chemistry* **2015**, *54*, 7600–7606.

(17) Ding, Y. S.; Yu, K. X.; Reta, D.; Ortu, F.; Winpenny, R. E.; Zheng, Y. Z.; Chilton, N. F. *Nature Communications* **2018**, *9*, 3134.

(18) Briganti, M.; Santanni, F.; Tesi, L.; Totti, F.; Sessoli, R.; Lunghi, A. *Journal of the American Chemical Society* **2021**, *143*, 13633–13645.

(19) Gómez-Coca, S.; Urtizberea, A.; Cremades, E.; Alonso, P. J.; Camón, A.; Ruiz, E.; Luis, F. *Nature Communications* **2014**, *5*.

(20) Liu, J. L.; Chen, Y. C.; Tong, M. L. *Chemical Society Reviews* **2018**, *47*, 2431–2453.

(21) Lunghi, A.; Sanvito, S. *Science Advances* **2019**, *5*.

(22) Ceglarska, M.; Stefańczyk, O.; Ohkoshi, S. I.; Majcher-Fitas, A. M. *Dalton Transactions* **2020**, *49*, 6807–6815.

(23) Moseley, I. P.; Ard, C. P.; DiVerdi, J. A.; Ozarowski, A.; Chen, H.; Zadrozny, J. M. *Cell Reports Physical Science* **2022**, *3*, 100802.

(24) Kishi, Y.; Pointillart, F.; Lefeuvre, B.; Riobé, F.; Le Guennic, B.; Golhen, S.; Cador, O.; Maury, O.; Fujiwara, H.; Ouahab, L. *Chemical Communications* **2017**, *53*, 3575–3578.

(25) Tesi, L.; Salman, Z.; Cimatti, I.; Pointillart, F.; Bernot, K.; Mannini, M.; Sessoli, R. *Chemical Communications* **2018**, *54*, 7826–7829.

(26) Frost, J. M.; Harriman, K. L.; Murugesu, M. *Chemical Science* **2016**, *7*, 2470–2491.

(27) Feng, M.; Tong, M. L. *Chemistry - A European Journal* **2018**, *24*, 7574–7594.

(28) Perlepe, P. S.; Maniaki, D.; Pilichos, E.; Katsoulakou, E.; Perlepes, S. P. *Inorganics* **2020**, *8*, 39.

(29) Yu, K. X.; Kragskow, J. G.; Ding, Y. S.; Zhai, Y. Q.; Reta, D.; Chilton, N. F.; Zheng, Y. Z. *Chem* **2020**, *6*, 1777–1793.

(30) Sessoli, R.; Powell, A. K. *Coordination Chemistry Reviews* **2009**, *253*, 2328–2341.

(31) Rinehart, J. D.; Fang, M.; Evans, W. J.; Long, J. R. *Journal of the American Chemical Society* **2011**, *133*, 14236–14239.

(32) Woodruff, D. N.; Winpenny, R. E.; Layfield, R. A. *Chemical Reviews* **2013**, *113*, 5110–5148.

(33) Liddle, S. T.; Van Slageren, J. *Chemical Society Reviews* **2015**, *44*, 6655–6669.

(34) McAdams, S. G.; Ariciu, A. M.; Kostopoulos, A. K.; Walsh, J. P.; Tuna, F. *Coordination Chemistry Reviews* **2017**, *346*, 216–239.

(35) Thomas, L.; Caneschi, A.; Barbara, B. *Physical Review Letters* **1999**, *83*, 2398–2401.

(36) Jahn H. A.; Teller E. *Proceedings of the Royal Society of London. Series A - Mathematical and Physical Sciences* **1937**, *161*, 220–235.

(37) Bersuker, I. B. *Chemical Reviews* **2001**, *101*, 1067–1114.

(38) Ishikawa, N.; Sugita, M.; Ishikawa, T.; Koshihara, S. Y.; Kaizu, Y. *Journal of the American Chemical Society* **2003**, *125*, 8694–8695.

(39) Goodwin, C. A.; Ortu, F.; Reta, D.; Chilton, N. F.; Mills, D. P. *Nature* **2017**, *548*, 439–442.

(40) Guo, F. S.; Day, B. M.; Chen, Y. C.; Tong, M. L.; Mansikkamäki, A.; Layfield, R. A. *Science* **2018**, *362*, 1400–1403.

(41) Bethe, H. *Annalen der Physik* **1929**, *395*, 133–208.

(42) Van Vleck, J. H. *Physical Review* **1932**, *41*, 208–215.

(43) Figgis, B. N.; Hitchman, M. A. *Journal of Chemical Education* **2002**, *79*, ed. by Hitchman, M. A., 1072.

(44) De Groot, F.; Kotani, A., *Core level spectroscopy of solids*; CRC Press: 2008, pp 1–491.

(45) Wang, S. G.; Schwarz, W. H. *Journal of Chemical Physics* **1998**, *109*, 7252–7262.

(46) Power, P. P. *Comments on Inorganic Chemistry* **2011**, *8*, 177–202.

(47) Vogel, M.; Weber, W.; Wenzel, W. *Journal of Chemical Physics* **2006**, *125*, 7252.

(48) Gunnar Werncke, C.; Bunting, P. C.; Duhayon, C.; Long, J. R.; Bontemps, S.; Sabo-Etienne, S. *Angewandte Chemie - International Edition* **2015**, *54*, 245–248.

(49) Gerloch, M.; Harding, J. H.; Woolley, R. G. In Springer, Berlin, Heidelberg: 1981, pp 1–46.

(50) Gerloch, M. In *Understanding Molecular Properties*; Springer, Dordrecht: 1987, pp 111–142.

(51) Schäffer, C. E. *Pure and Applied Chemistry* **1970**, *24*, 361–392.

(52) Deeth, R. J. *Journal of the Chemical Society, Dalton Transactions* **1993**, 1061–1064.

(53) Bridgeman, A. J. *Journal of the Chemical Society - Dalton Transactions* **1996**, 2601–2607.

(54) Zadrozny, J. M.; Atanasov, M.; Bryan, A. M.; Lin, C. Y.; Rekken, B. D.; Power, P. P.; Neese, F.; Long, J. R. *Chemical Science* **2013**, *4*, 125–138.

(55) Kramers, H. A. *Proc. R. Acad. Sci. Amsterdam* **1930**, *33*.

(56) Zadrozny, J. M.; Xiao, D. J.; Atanasov, M.; Long, G. J.; Grandjean, F.; Neese, F.; Long, J. R. *Nature Chemistry* **2013**, *5*, 577–581.

(57) Perić, M. *Molecular Physics* **2007**, *105*, 59–69.

(58) Yoshihara, D.; Karasawa, S.; Koga, N. *Journal of the American Chemical Society* **2008**, *130*, 10460–10461.

(59) Cowan, R. D., *The Theory of Atomic Structure and Spectra*; University of California Press: 1981, p 731.

(60) Bunting, P. C.; Atanasov, M.; Damgaard-Møller, E.; Perfetti, M.; Crassee, I.; Orlita, M.; Overgaard, J.; Van Slageren, J.; Neese, F.; Long, J. R. *Science* **2018**, *362*, 7319.

(61) Zintl, E.; Brauer, G. *Z. Elektrochem.* **1935**, *41*, 102–107.

(62) Rabenau, A.; Schulz, H. *Journal of The Less-Common Metals* **1976**, *50*, 155–159.

(63) Boukamp, B. A.; Huggins, R. A. *Physics Letters A* **1976**, *58*, 231–233.

(64) Kress, W.; Grimm, H.; Press, W.; Lefebvre, J. *Physical Review B* **1980**, *22*, 4620–4625.

(65) Rowsell, J. L.; Pralong, V.; Nazar, L. F. *Journal of the American Chemical Society* **2001**, *123*, 8598–8599.

(66) Stoeva, Z.; Jäger, B.; Gomez, R.; Messaoudi, S.; Yahia, M. B.; Rocquefelte, X.; Hix, G. B.; Wolf, W.; Titman, J. J.; Gautier, R.; Herzig, P.; Gregory, D. H. *Journal of the American Chemical Society* **2007**, *129*, 1912–1920.

(67) Hu, Y. H.; Huo, Y. *Journal of Physical Chemistry A* **2011**, *115*, 11678–11681.

(68) Baldwin, F. P.; Blanchard, E. J.; Koenig, P. E. *Journal of Organic Chemistry* **1965**, *30*, 671–673.

(69) Chen, P.; Xiong, Z.; Luo, J.; Lin, J.; Lee Tan, K. *Nature* **2002**, *420*, 302–304.

(70) Sachsze, W.; Juza, R. *Zeitschrift für anorganische Chemie* **1949**, *259*, 278–290.

(71) Schnelle, W.; Niewa, R.; Wagner, F. R. *Journal of Magnetism and Magnetic Materials* **2004**, *272-276*, 828–829.

(72) Niewa, R.; Hu, Z.; Kniep, R. *European Journal of Inorganic Chemistry* **2003**, *2003*, 1632–1634.

(73) Niewa, R.; Huang, Z. L.; Schnelle, W.; Hu, Z.; Kniep, R. *Zeitschrift fur Anorganische und Allgemeine Chemie* **2003**, *629*, 1778–1786.

(74) Klatyk, J.; Schnelle, W.; Wagner, F. R.; Niewa, R.; Novák, P.; Kniep, R.; Waldeck, M.; Ksenofontov, V.; Gütlich, P. *Physical Review Letters* **2002**, *88*, 2072021–2072024.

(75) Novák, P.; Wagner, F. R. *Physical Review B - Condensed Matter and Materials Physics* **2002**, *66*, 1–6.

(76) Novák, P.; Wagner, F. R. In *Journal of Magnetism and Magnetic Materials*, 2004; Vol. 272-276.

(77) Klatyk, J.; Kniep, R. *Zeitschrift fur Kristallographie - New Crystal Structures* **1999**, *214*, 449–450.

(78) Jesche, A.; Canfield, P. C. *Philosophical Magazine* **2014**, *94*, 2372–2402.

(79) Muller-Bouvet, D.; Pereira-Ramos, J. P.; Bach, S.; Willmann, P.; Michalowicz, A. *Inorganic Chemistry* **2014**, *53*, 6127–6131.

(80) Gregory, D. H.; O'Meara, P. M.; Gordon, A. G.; Hodges, J. P.; Short, S.; Jorgensen, J. D. *Chemistry of Materials* **2002**, *14*, 2063–2070.

(81) Fix, M.; Jesche, A.; Jantz, S. G.; Bräuninger, S. A.; Klauss, H. H.; Manna, R. S.; Pietsch, I. M.; Höppe, H. A.; Canfield, P. C. *Physical Review B* **2018**, *97*, 064419.

(82) Jesche, A.; McCallum, R. W.; Thimmaiah, S.; Jacobs, J. L.; Taufour, V.; Kreyssig, A.; Houk, R. S.; Bud'Ko, S. L.; Canfield, P. C. *Nature Communications* **2014**, *5*, 3333.

(83) Fix, M.; Atkinson, J. H.; Canfield, P. C.; Del Barco, E.; Jesche, A. *Physical Review Letters* **2018**, *120*, 147202.

(84) Castro-Alvarez, A.; Gil, Y.; Llanos, L.; Aravena, D. *Inorganic Chemistry Frontiers* **2020**, *7*, 2478–2486.

(85) Errulat, D.; Harriman, K. L. M.; Gálico, D. A.; Ovens, J. S.; Mansikkamäki, A.; Murugesu, M. *Inorganic Chemistry Frontiers* **2021**.

(86) Mannini, M.; Pineider, F.; Danieli, C.; Totti, F.; Sorace, L.; Sainctavit, P.; Arrio, M. A.; Otero, E.; Joly, L.; Cezar, J. C.; Cornia, A.; Sessoli, R. *Nature* **2010**, *468*, 417–421.

(87) Gaita-Ariño, A.; Luis, F.; Hill, S.; Coronado, E. *Nature Chemistry* **2019**, *11*, 301–309.

(88) Leuenberger, M. N.; Mucciolo, E. R. *Physical Review Letters* **2006**, *97*, 126601.

(89) Thomsen, M. K.; Nyvang, A.; Walsh, J. P.; Bunting, P. C.; Long, J. R.; Neese, F.; Atanasov, M.; Genoni, A.; Overgaard, J. *Inorganic Chemistry* **2019**, *58*, 3211–3218.

(90) Huzan, M. S.; Fix, M.; Aramini, M.; Bencok, P.; Mosselmans, J. F. W.; Hayama, S.; Breitner, F. A.; Gee, L. B.; Titus, C. J.; Arrio, M. A.; Jesche, A.; Baker, M. L. *Chemical Science* **2020**, *11*, 11801–11810.

(91) Cornia, A.; Mannini, M.; Sainctavit, P.; Sessoli, R. *Chemical Society Reviews* **2011**, *40*, 3076–3091.

(92) Campbell, V. E.; Tonelli, M.; Cimatti, I.; Moussy, J. B.; Tortech, L.; Dappe, Y. J.; Rivière, E.; Guillot, R.; Delprat, S.; Mattana, R.; Seneor, P.; Ohresser, P.; Choueikani, F.; Otero, E.; Koprowiak, F.; Chilkuri, V. G.; Suaud, N.; Guihéry, N.; Galtayries, A.; Miserque, F.; Arrio, M. A.; Sainctavit, P.; Mallah, T. *Nature Communications* **2016**, *7*, 13646.

(93) Zykin, M. A.; Kazin, P. E.; Jansen, M. *Chemistry - A European Journal* **2020**, *26*, 8834–8844.

(94) Bach, S.; Pereira-Ramos, J. P.; Ducros, J. B.; Willmann, P. *Solid State Ionics* **2009**, *180*, 231–235.

(95) Xu, L.; Zangeneh, Z.; Yadav, R.; Avdoshenko, S.; Van Den Brink, J.; Jesche, A.; Hozoi, L. *Nanoscale* **2017**, *9*, 10596–10600.

(96) Bräuninger, S. A.; Jesche, A.; Kamusella, S.; Seewald, F.; Fix, M.; Sarkar, R.; Zvyagin, A. A.; Klauss, H. H. *Physical Review B* **2020**, *102*.

(97) Albert, C.; Ballé, T. J.; Breitner, F. A.; Krupskaya, Y.; Alfonsov, A.; Zangeneh, Z.; Avdoshenko, S.; Eldeeb, M. S.; Hozoi, L.; Vilangottunjalil, A.; Haubold, E.; Charnukha, A.; Büchner, B.; Jesche, A.; Kataev, V. *Inorganic Chemistry* **2021**, *60*, 4497–4507.

(98) Wu, S.; Dong, Z.; Boey, F.; Wu, P. *Applied Physics Letters* **2009**, *94*, 172104.

(99) Wu, G.; Wu, S.; Wu, P. *Physical Review Letters* **2011**, *107*.

(100) Wu, S.; Dong, Z.; Wu, P.; Boey, F. *Journal of Materials Chemistry* **2011**, *21*, 165–170.

(101) Shin, S. *AAPPS Bulletin* **2021**, *31*.

(102) *Magnetism: A synchrotron radiation approach*; Beaurepaire, E., Bulou, H., Scheurer, F., Kappler, J.-P., Eds.; Lecture Notes in Physics, Vol. 697; Springer: 2006.

(103) Cramer, S. P., *X-ray Spectroscopy with Synchrotron Radiation*; Springer: Berlin, 2020.

(104) *Magnetism and Accelerator-Based Light Sources*; Bulou, H., Joly, L., Mariot, J.-M., Scheurer, F., Eds.; Springer Proceedings in Physics, Vol. 262; Springer: Cham, 2021.

(105) Glatzel, P.; Bergmann, U. *Coordination Chemistry Reviews* **2005**, *249*, 65–95.

(106) Kowalska, J.; DeBeer, S. *Biochimica et Biophysica Acta - Molecular Cell Research* **2015**, *1853*, 1406–1415.

(107) Baker, M. L.; Mara, M. W.; Yan, J. J.; Hodgson, K. O.; Hedman, B.; Solomon, E. I. *Coordination Chemistry Reviews* **2017**, *345*, 182–208.

(108) De Groot, F.; Vankó, G.; Glatzel, P. *Journal of Physics Condensed Matter* **2009**, *21*.

(109) Ravel, B.; Newville, M. In *Journal of Synchrotron Radiation*, 2005; Vol. 12, pp 537–541.

(110) Bunker, G., *Introduction to XAFS : a practical guide to X-ray absorption fine structure spectroscopy*; Cambridge University Press: Cambridge, UK ; 2010.

(111) Calvin, S., *XAFS for Everyone*; CRC Press: Boca Raton, FL, 2013.

(112) Hämäläinen, K.; Siddons, D. P.; Hastings, J. B.; Berman, L. E. *Physical Review Letters* **1991**, *67*, 2850.

(113) Roemelt, M.; Maganas, D.; Debeer, S.; Neese, F. *Journal of Chemical Physics* **2013**, *138*.

(114) Maganas, D.; Roemelt, M.; Hävecker, M.; Trunschke, A.; Knop-Gericke, A.; Schlögl, R.; Neese, F. *Physical Chemistry Chemical Physics* **2013**, *15*, 7260–7276.

(115) Van der Laan, G.; Figueroa, A. I. *Coordination Chemistry Reviews* **2014**, *277*, 95–129.

(116) Piamonteze, C.; Miedema, P.; De Groot, F. M. *Physical Review B - Condensed Matter and Materials Physics* **2009**, *80*.

(117) Liu, B.; Van Schooneveld, M. M.; Cui, Y.-T.; Miyawaki, J.; Harada, Y.; Eschemann, T. O.; De Jong, K. P.; Delgado-Jaime, M. U.; De Groot, F. M. F. *J. Phys. Chem. C* **2017**, 17450–17456.

(118) Wang, R. P.; Hariki, A.; Sotnikov, A.; Frati, F.; Okamoto, J.; Huang, H. Y.; Singh, A.; Huang, D. J.; Tomiyasu, K.; Du, C. H.; Kuneš, J.; De Groot, F. M. *Physical Review B* **2018**, *98*, 35149.

(119) Thole, B. T.; Carra, P.; Sette, F.; Van Der Laan, G. *Physical Review Letters* **1992**, *68*, 1943–1946.

(120) Carra, P.; Thole, B. T.; Altarelli, M.; Wang, X. *Physical Review Letters* **1993**, *70*, 694–697.

(121) Baker, M. L.; Blundell, S. J.; Domingo, N.; Hill, S. In *Structure and Bonding*; Springer, Berlin, Heidelberg: 2015; Vol. 164, pp 231–291.

(122) Gel'mukhanov, F.; Ågren, H. *Physics Report* **1999**, *312*, 87–330.

(123) Zhou, K.-J.; Walters, A.; Garcia-Fernandez, M.; Rice, T.; Hand, M.; Nag, A.; Li, J.; Agrestini, S.; Garland, P.; Wang, H.; Alcock, S.; Nistea, I.; Nutter, B.; Rubies, N.; Knap, G.; Gaughran, M.; Yuan, F.; Chang, P.; Emmins, J.; Howell, G. *J. Synchrotron Rad* **2022**, *29*, 563–580.

(124) Rubensson, J. E. *Journal of Electron Spectroscopy and Related Phenomena* **2000**, *110*, 135–151.

(125) Kotani, A.; Shin, S. *Resonant inelastic x-ray scattering spectra for electrons in solids*; tech. rep. 1; 2001, pp 203–246.

(126) Ament, L. J.; Van Veenendaal, M.; Devereaux, T. P.; Hill, J. P.; Van Den Brink, J. *Reviews of Modern Physics* **2011**, *83*, 705–767.

(127) Zimmermann, P.; Hunault, M. O.; De Groot, F. M. *Journal of Spectroscopy* **2018**, *2018*, 1–50.

(128) Fatale, S.; Moser, S.; Grioni, M. *Journal of Electron Spectroscopy and Related Phenomena* **2015**, *200*, 274–281.

(129) Fumagalli, R.; Braicovich, L.; Minola, M.; Peng, Y. Y.; Kummer, K.; Betto, D.; Rossi, M.; Lefrançois, E.; Morawe, C.; Salluzzo, M.; Suzuki, H.; Yakhou, F.; Le Tacon, M.; Keimer, B.; Brookes, N. B.; Sala, M. M.; Ghiringhelli, G. *Physical Review B* **2019**, *99*.

(130) Hayama, S.; Duller, G.; Sutter, J. P.; Amboage, M.; Boada, R.; Freeman, A.; Keenan, L.; Nutter, B.; Cahill, L.; Leicester, P.; Kemp, B.; Rubies, N.; Diaz-Moreno, S. *Journal of Synchrotron Radiation* **2018**, *25*, 1556–1564.

(131) De Groot, F. M.; Arrio, M. A.; Sainctavit, P.; Cartier, C.; Chen, C. T. *Solid State Communications* **1994**, *92*, 991–995.

(132) Kurian, R.; Kunnus, K.; Wernet, P.; Butorin, S. M.; Glatzel, P.; De Groot, F. M. *Journal of Physics Condensed Matter* **2012**, *24*, 452201.

(133) Carboni, R.; Giovannini, S.; Antonioli, G.; Boscherini, F. *Physica Scripta T* **2005**, *T115*, 986–988.

(134) Wang, H.; Peng, G.; Miller, L. M.; Scheuring, E. M.; George, S. J.; Chance, M. R.; Cramer, S. P. *Journal of the American Chemical Society* **1997**, *119*, 4921–4928.

(135) Vercamer, V.; Hunault, M. O.; Lelong, G.; Haverkort, M. W.; Calas, G.; Arai, Y.; Hijiya, H.; Paulatto, L.; Brouder, C.; Arrio, M. A.; Juhin, A. *Physical Review B* **2016**, *94*, 245115.

(136) Hunault, M. O.; Harada, Y.; Miyawaki, J.; Wang, J.; Meijerink, A.; De Groot, F. M.; Van Schooneveld, M. M. *Journal of Physical Chemistry A* **2018**, *122*, 4399–4413.

(137) Nag, A.; Robarts, H. C.; Wenzel, F.; Li, J.; Elnaggar, H.; Wang, R. P.; Walters, A. C.; García-Fernández, M.; De Groot, F. M.; Haverkort, M. W.; Zhou, K. J. *Physical Review Letters* **2020**, *124*.

(138) Wang, R.-P.; Huang, M.-J.; Hariki, A.; Okamoto, J.; Huang, H.-Y.; Singh, A.; Huang, D.-J.; Nagel, P.; Schuppler, S.; Haarman, T.; Liu, B.; de Groot, F. M. F. *The Journal of Physical Chemistry C* **2022**.

(139) Dirac, P. A. M. *Proceedings of the Royal Society of London* **1928**, *117*, 610–624.

(140) Haverkort, M. W.; Zwierzycki, M.; Andersen, O. K. *Physical Review B - Condensed Matter and Materials Physics* **2012**, *85*, 165113.

(141) Thole, B. T.; Van Der Laan, G.; Fuggle, J. C.; Sawatzky, G. A.; Karnatak, R. C.; Esteva, J. M. *Physical Review B* **1985**, *32*, 5107–5118.

(142) Butler, P. H., *Point Group Symmetry Applications*; Plenum: New York ; 1981.

(143) Juhin, A.; Brouder, C.; de Groot, F. *Central European Journal of Physics* **2014**, *12*, 323–340.

(144) Haverkort, M. W. In *Journal of Physics: Conference Series*, 2016; Vol. 712, p 12001.

(145) Lu, Y.; Cao, X.; Hansmann, P.; Haverkort, M. W. *Physical Review B* **2019**, *100*, 213984.

(146) Born, M.; Oppenheimer, R. *Annalen der Physik* **1927**, *389*, 457–484.

(147) Cowan, R. D., *The Theory of Atomic Structure and Spectra*; Los Alamos series in basic and applied sciences; University of California Press: Berkeley ; 1981.

(148) Condon, E. U. *Physical Review* **1930**, *36*, 1121–1133.

(149) Condon, E. U.; Shortley, G. H. In *Selected Scientific Papers of E.U. Condon*; Springer New York: New York, NY, 1931, pp 128–148.

(150) Slater, J. C., *Quantum theory of atomic structure, Vol I*; International series in pure and applied physics; McGraw-Hill: New York, 1960.

(151) Slater, J. C., *Quantum theory of atomic structure, Vol II*; McGraw-Hill: New York, 1960.

(152) Lever, A. B. P., *Inorganic electronic spectroscopy*, 2nd ed.; Studies in physical and theoretical chemistry ; 33; Elsevier: Amsterdam ; 1984, p 103.

(153) Griffith, J. S., *The theory of transition-metal ions*; Cambridge University Press: Cambridge, 1961.

(154) Sugano, S.; Tanabe, Y.; Kamimura, H., *Multiplets of Transition-Metal Ions in Crystals*; Tanabe, Y., Kamimura, H., Eds.; Pure and applied physics, v. 33; Academic Press: New York, 1970.

(155) Jørgensen, C. K. In *Structure And Bonding*; Springer, Berlin, Heidelberg: 1966, pp 3–31.

(156) Anthon, C.; Schäffer, C. E. *Coordination Chemistry Reviews* **2002**, *226*, 17–38.

(157) Konig, E.; Kremer, S., *Ligand Field Energy Diagrams*, 1977.

(158) Görller-Walrand, C.; Binnemans, K. In *Handbook on the Physics and Chemistry of Rare Earths*; Elsevier: 1996; Vol. 23; Chapter 155, pp 121–283.

(159) Wu, W.; Song, L.; Cao, Z.; Zhang, Q.; Shaik, S. *Journal of Physical Chemistry A* **2002**, *106*, 2721–2726.

(160) Westre, T. E.; Kennepohl, P.; DeWitt, J. G.; Hedman, B.; Hodgson, K. O.; Solomon, E. I. *Journal of the American Chemical Society* **1997**, *119*, 6297–6314.

(161) Arrio, M. A.; Rossano, S.; Brouder, C.; Galoisy, L.; Calas, G. *Europhysics Letters* **2000**, *51*, 454–460.

(162) Lundberg, M.; Kroll, T.; Debeer, S.; Bergmann, U.; Wilson, S. A.; Glatzel, P.; Nordlund, D.; Hedman, B.; Hodgson, K. O.; Solomon, E. I. *Journal of the American Chemical Society* **2013**, *135*, 17121–17134.

(163) Bonhommeau, S.; Pontius, N.; Cobo, S.; Salmon, L.; De Groot, F. M.; Molnár, G.; Bousseksou, A.; Dürr, H. A.; Eberhardt, W. *Physical Chemistry Chemical Physics* **2008**, *10*, 5882–5889.

(164) Wasinger, E. C.; De Groot, F. M.; Hedman, B.; Hodgson, K. O.; Solomon, E. I. *Journal of the American Chemical Society* **2003**, *125*, 12894–12906.

(165) Hocking, R. K.; Wasinger, E. C.; De Groot, F. M.; Hodgson, K. O.; Hedman, B.; Solomon, E. I. *Journal of the American Chemical Society* **2006**, *128*, 10442–10451.

(166) Yan, J. J.; Gonzales, M. A.; Mascharak, P. K.; Hedman, B.; Hodgson, K. O.; Solomon, E. I. *Journal of the American Chemical Society* **2017**, *139*, 1215–1225.

(167) Kramers, H. A.; Heisenberg, W. *Zeitschrift für Physik* **1925**, *31*, 681–708.

(168) Glatzel, P.; Bergmann, U. *Coordination Chemistry Reviews* **2005**, *249*, 65–95.

(169) Haverkort, M. W. *Physical Review Letters* **2010**, *105*, 167404.

(170) Lunghi, A.; Sanvito, S. *Journal of Chemical Physics* **2020**, *153*, 174113.

(171) Lunghi, A. *Science Advances* **2022**, *8*, DOI: 10.1126/SCIADV.ABN7880.

(172) Scheidt, W. R.; Durbin, S. M.; Sage, J. T. *Journal of Inorganic Biochemistry* **2005**, *99*, 60–71.

(173) Scheidt, W. R.; Li, J.; Sage, J. T. What Can Be Learned from Nuclear Resonance Vibrational Spectroscopy: Vibrational Dynamics and Hemes, 2017.

(174) Scherthan, L.; Pfleger, R. F.; Auerbach, H.; Hochdörffer, T.; Wolny, J. A.; Bi, W.; Zhao, J.; Hu, M. Y.; Alp, E. E.; Anson, C. E.; Diller, R.; Powell, A. K.; Schünemann, V. *Angewandte Chemie - International Edition* **2020**, *59*, 8818–8822.

(175) Gee, L. B.; Wang, H.; Cramer, S. P. In *Methods in Enzymology*; Academic Press Inc.: 2018; Vol. 599, pp 409–425.

(176) Rüffer, R.; Chumakov, A. I. *Hyperfine Interactions 1996 97:1* **1996**, *97*, 589–604.

(177) Diaz-Moreno, S.; Amboage, M.; Basham, M.; Boada, R.; Bricknell, N. E.; Cibin, G.; Cobb, T. M.; Filik, J.; Freeman, A.; Geraki, K.; Gianolio, D.; Hayama, S.; Ignatyev, K.; Keenan, L.; Mikulska, I.; Mosselmans, J. F. W.; Mudd, J. J.; Parry, S. A. *Journal of Synchrotron Radiation* **2018**, *25*, 998–1009.